



# Free-Piston Stirling Power Conversion Unit for Fission Surface Power, Phase I Final Report

*J. Gary Wood, Andrew Buffalino, and Ezekiel Holliday  
Sunpower, Inc., Athens, Ohio*

*Barry Penswick  
Consultant, Stevenson, Washington*

*David Gedeon  
Gedeon Associates, Athens, Ohio*

## NASA STI Program . . . in Profile

Since its founding, NASA has been dedicated to the advancement of aeronautics and space science. The NASA Scientific and Technical Information (STI) program plays a key part in helping NASA maintain this important role.

The NASA STI Program operates under the auspices of the Agency Chief Information Officer. It collects, organizes, provides for archiving, and disseminates NASA's STI. The NASA STI program provides access to the NASA Aeronautics and Space Database and its public interface, the NASA Technical Reports Server, thus providing one of the largest collections of aeronautical and space science STI in the world. Results are published in both non-NASA channels and by NASA in the NASA STI Report Series, which includes the following report types:

- **TECHNICAL PUBLICATION.** Reports of completed research or a major significant phase of research that present the results of NASA programs and include extensive data or theoretical analysis. Includes compilations of significant scientific and technical data and information deemed to be of continuing reference value. NASA counterpart of peer-reviewed formal professional papers but has less stringent limitations on manuscript length and extent of graphic presentations.
- **TECHNICAL MEMORANDUM.** Scientific and technical findings that are preliminary or of specialized interest, e.g., quick release reports, working papers, and bibliographies that contain minimal annotation. Does not contain extensive analysis.
- **CONTRACTOR REPORT.** Scientific and technical findings by NASA-sponsored contractors and grantees.

- **CONFERENCE PUBLICATION.** Collected papers from scientific and technical conferences, symposia, seminars, or other meetings sponsored or cosponsored by NASA.
- **SPECIAL PUBLICATION.** Scientific, technical, or historical information from NASA programs, projects, and missions, often concerned with subjects having substantial public interest.
- **TECHNICAL TRANSLATION.** English-language translations of foreign scientific and technical material pertinent to NASA's mission.

Specialized services also include creating custom thesauri, building customized databases, organizing and publishing research results.

For more information about the NASA STI program, see the following:

- Access the NASA STI program home page at <http://www.sti.nasa.gov>
- E-mail your question via the Internet to [help@sti.nasa.gov](mailto:help@sti.nasa.gov)
- Fax your question to the NASA STI Help Desk at 443-757-5803
- Telephone the NASA STI Help Desk at 443-757-5802
- Write to:  
NASA Center for AeroSpace Information (CASI)  
7115 Standard Drive  
Hanover, MD 21076-1320

NASA/CR—2010-216750



# Free-Piston Stirling Power Conversion Unit for Fission Surface Power, Phase I Final Report

*J. Gary Wood, Andrew Buffalino, and Ezekiel Holliday  
Sunpower, Inc., Athens, Ohio*

*Barry Penswick  
Consultant, Stevenson, Washington*

*David Gedeon  
Gedeon Associates, Athens, Ohio*

Prepared under Contract NNC08CA65C

National Aeronautics and  
Space Administration

Glenn Research Center  
Cleveland, Ohio 44135

---

July 2010

This report contains preliminary findings,  
subject to revision as analysis proceeds.

Trade names and trademarks are used in this report for identification  
only. Their usage does not constitute an official endorsement,  
either expressed or implied, by the National Aeronautics and  
Space Administration.

*Level of Review:* This material has been technically reviewed by NASA technical management.

Available from

NASA Center for Aerospace Information  
7115 Standard Drive  
Hanover, MD 21076-1320

National Technical Information Service  
5301 Shawnee Road  
Alexandria, VA 22312

Available electronically at <http://gltrs.grc.nasa.gov>

# Free-Piston Stirling Power Conversion Unit for Fission Surface Power, Phase I Final Report

J. Gary Wood, Andrew Buffalino, and Ezekiel Holliday  
Sunpower, Inc.  
Athens, Ohio 45701

Barry Penswick  
Consultant  
Stevenson, Washington 98648

David Gedeon  
Gedeon Associates  
Athens, Ohio 45701

## Summary

In Phase I, we completed the design of a 12 kW dual-opposed free-piston Stirling convertor and controller. The convertor is shown in Figure 1. The convertor mass is calculated as 188 kg not including the piping shown, and the controller is projected at 68 kg for a total of 256 kg. The machine operates at 60 Hz at an operating pressure of 6.2 MPa (absolute). The convertor is approximately 0.3 m (11.9 in.) in diameter and 1.1 m (43 in.) long.

Convertor efficiency is predicted at 27 percent (AC electrical out/heat in) and the efficiency of the controller is predicted at 91 percent. Heating is provided by a pumped NaK (sodium potassium) fluid which flows axially on the outside of the heater heads supplied from a central tangentially fed manifold. In addition to the primary engine rejectors, parallel water paths are provided to cool the alternator enclosure of both convertors. The small diameter protrusions on the ends of the unit are piston position sensors.

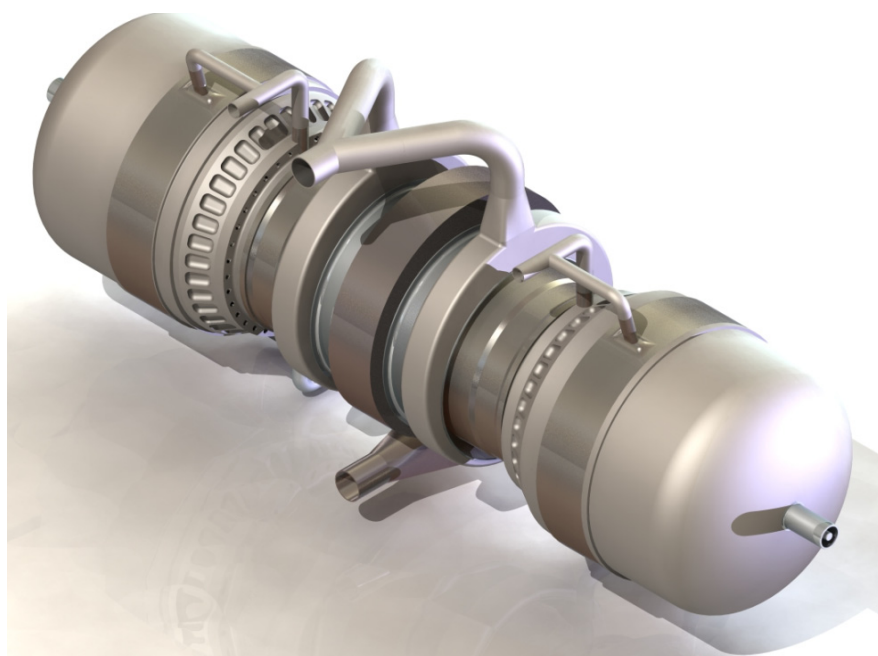


Figure 1.—Outer view of hermetically sealed Fission Surface Power (FSP) convertor.

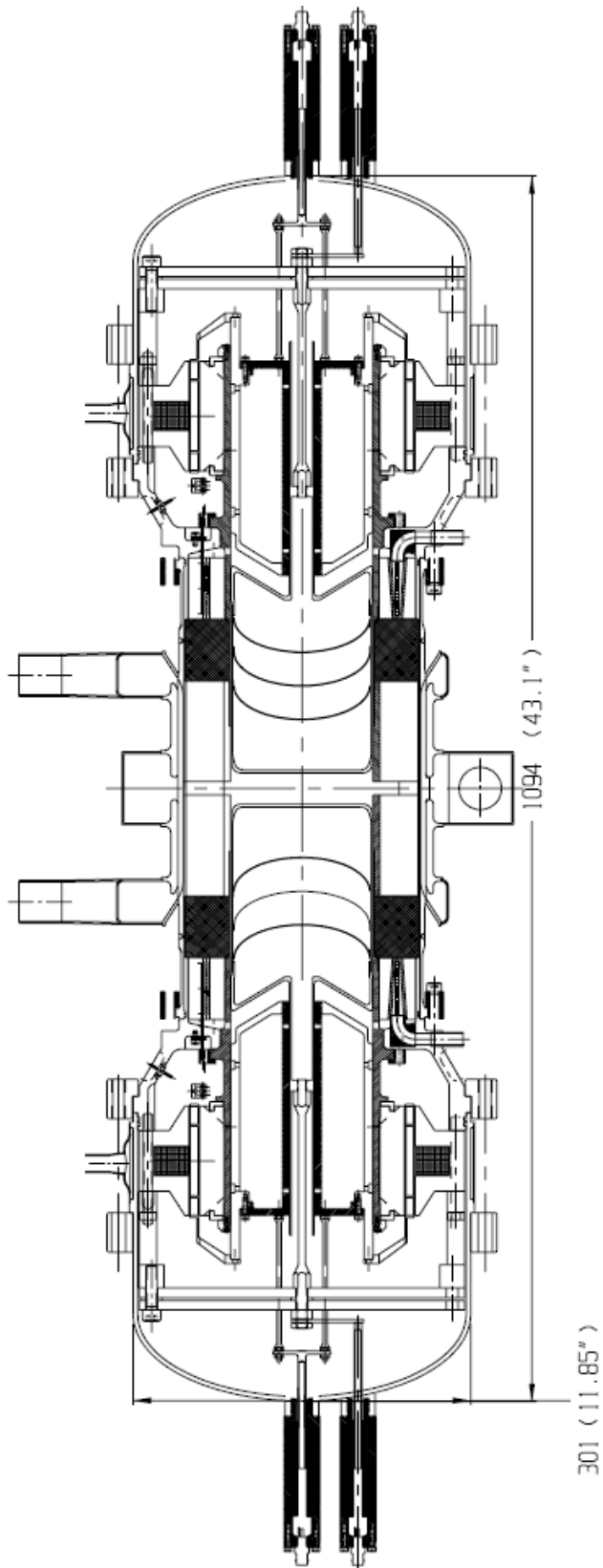


TABLE 1.—MAJOR DESIGN PARAMETERS

Power (Wac).....	6000
Hot HX max metal T (°C) .....	570
Cold HX min wall T (°C) .....	111
Eff % AC out/heat in .....	27
Mean operating pressure (MPa).....	6.2
Frequency .....	60
Piston amplitude (mm) .....	16
Displacer amplitude (mm) .....	12
Displacer phase (deg) .....	60
L acc (mm) .....	90
L reg (mm).....	55
L rej (mm) .....	55
D cyl (mm) .....	127
ID head (mm) .....	210

Figure 2.—Cross-section of bolted convertor.

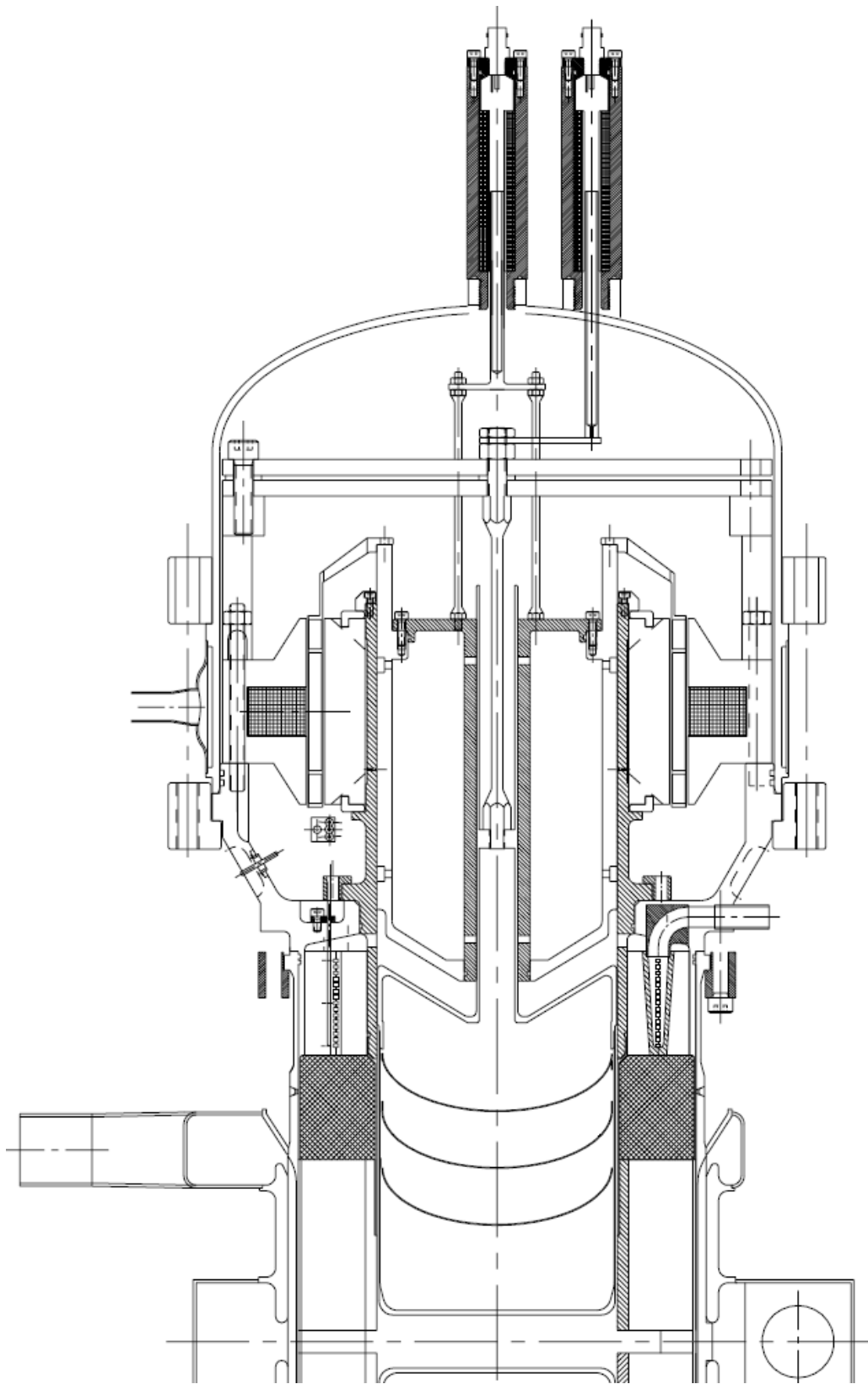


Figure 3.—Cross section of one half of the converter.



# Contents

Summary .....	iii
Design Overview .....	1
Design Features.....	2
Heat Source and Sink Requirements .....	2
Constant Bore.....	2
Rod-Through Piston, Resonated by Planar Mechanical Springs.....	2
Piston-Based Gas Bearings .....	2
Simple Monolithic Heater Head.....	2
Internal Circumferential Coolant Passages .....	3
Displacer.....	4
Regenerator .....	4
Alternator .....	5
Internal Acceptor Design .....	5
Summary of Heat Exchanger Dimensions .....	6
NaK Heating Circuit Design .....	6
Prototype Bolted Convertor With O-Rings .....	9
Alternator Cooling.....	10
Design Point.....	10
Materials and Adhesives .....	11
Cost Savings with Stainless Steel (SS) Vessel.....	12
Instrumentation .....	12
Mass Breakdown.....	13
Alternator Design, Trades and Analysis .....	14
Testing and Development Plans.....	20
Convertor Development/Testing Plans Prior to Delivery .....	20
Developmental Testing With Electric Heating.....	20
Laboratory Cooling .....	21
Charging Circuit.....	21
Mounting of Opposed Unit.....	22
Outer Heat Exchanger Flow Testing .....	22
Heater Head Stress Analysis .....	24
Material Properties .....	24
Finite Element Model.....	26
Finite Element Mesh .....	27
Finite Element Analysis, Boundary Conditions and Contact Sets .....	28
Finite Element Analysis, Loads.....	29
Finite Element Analysis, Results.....	32
Conclusions .....	36
Engine Coupling Study .....	37
Selection of Mechanical Layout, Displacer Drive, and Springing.....	38
Off Design Projected Performance .....	43
FSP LM Acceptor Heat Exchanger .....	45
Design Goals .....	45
FSP System Imposed Constraints.....	45
HX Configuration Options .....	46
Semi-Tubular.....	46
Monolithic Configurations .....	47
Evaluation/Trade Study.....	48
Available Energy Loss Evaluation .....	53

Specific Concept Evaluation .....	53
Semi Tubular Configuration .....	53
Monolithic Configuration.....	54
Concept Rating/Trade Study .....	56
Selected Concept.....	57
Design Details .....	57
Integrated LM Manifold/HX Design Evaluation Process .....	60
Summary/Conclusions .....	60
Operating Parameter Trades.....	61
Projected Efficiency for a 12 kW Convertor .....	62
CFD Modeling of Water Circuit .....	63
CFD Modeling of NaK Circuit .....	66
Original Radial Inlet Manifold.....	66
Final Tangential Inlet Manifold .....	68
Regenerator Flow Entry Effects.....	71
Applied to FSP .....	72
Applied to ASC .....	72
Influence of Heater Head Wall Thickness .....	72
Concept to Reduce Internal Acceptor Mass.....	74
Control Electronics .....	75
Virtual Tuning Capacitor Controller Power Stage .....	76
Convertor Voltage LC Filter .....	78
DC/DC Converter.....	78
Control DSP Module.....	81
Shunt Regulator and Output Disconnect Switch.....	81
Summary .....	81
References.....	82

## Design Overview

The design in bolted laboratory form is shown in cross section in Figures 2 and 3. Early in the design selection process, we performed trades on all primary design details which are described later in this report. In the end, this design looks very much like a scaled-up Sunpower P2A (approximately 1200 W<sub>ac</sub>) engine, operating at twice the pressure (6.2 versus 3.1 MPa) and running at 60 Hz as opposed to 50 Hz.

The similarity of the FSP design to the P2A offers a large degree of confidence in the projected performance and reliability of the design. It is therefore viewed a low risk design, not only in terms of performance and reliability, but also in development cost.

Sunpower together with the experienced group of consultants assembled for this project (Barry Penswick, David Gedeon, David Berchowitz, and James Cairelli) after detailed study found no strong reasons when scaling up in power to change the basic design aspects of the machine. In the end, we realized that there are good reasons why Sunpower machines have evolved to a certain basic machine layout. Given the chance to change major details in a new larger machine most alternatives such as the virtual rod seemed to offer little or no advantage while adding significant complication.

We predict the FSP efficiency will be 27 percent AC<sub>out</sub>/heat in. For a comparison to other convertors, we have added the FSP to the following plot (Fig. 4) that we have presented in several papers. This compares engine-only efficiencies (without alternator) to other engines for which there is published data. Included in the plot is the Curzon-Ahlborn efficiency ( $= 1 - (T_c/T_h)^{0.5}$ ) which, while not an absolute limit, appears to be a reasonable benchmark for efficient machines. It should be noted that most modern steam power plants approach the Curzon-Ahlborn efficiency

One will notice that in certain cases (FSP, SPRE, and Mod 2) vertical bars are shown on efficiency. Typically, efficiency increases at reduced powers to a point (usually between 25 to 50 percent power). These bars show the design efficiency at the lower end and a higher value at part load at the upper end. One reason for higher efficiency at lower power is reduced heat exchanger loading, leading to improved interior cycle efficiency.

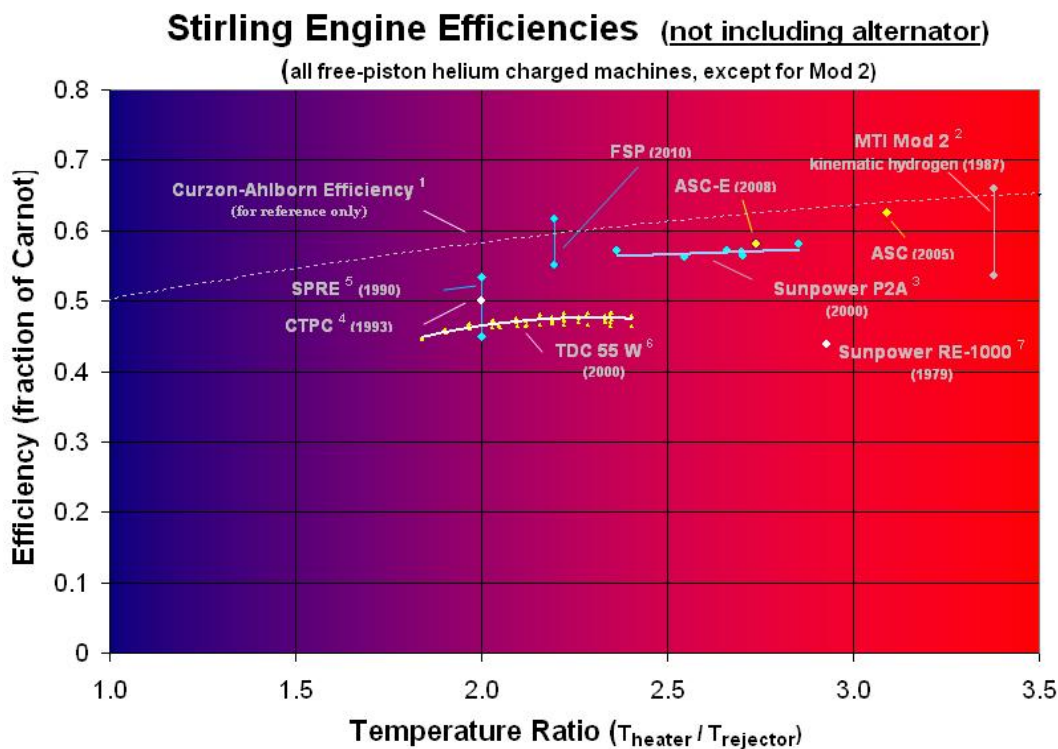


Figure 4.—Comparison of engine efficiencies.

## Design Features

In this section, we outline the basic aspects of the design. Several areas are also discussed in more detail in later sections.

### Heat Source and Sink Requirements

The following lists the heat source and sink requirements given in the statement of work.

- Heat Source:
  - Fluid NaK (78 percent K, 22 percent Na)
  - Supply temperature  $850\text{ K} \pm 25\text{ K}$
  - Supply pressure 150 kPa
  - Flow rate  $1.75\text{ kg/s} \pm 0.25\text{ kg/s}$
  - Allowable NaK-side heat exchanger pressure drop  $<7\text{ kPa}$  (1.02 psi)
- Heat Sink:
  - Fluid  $\text{H}_2\text{O}$
  - Supply temperature  $375\text{ K} \pm 25\text{ K}$  (same as SOW)
  - Supply pressure  $<700\text{ kPa}$  (but high enough to prevent boiling)
  - Flow rate  $0.375\text{ kg/s} \pm 0.125\text{ kg/s}$
  - Allowable  $\text{H}_2\text{O}$ -side heat exchanger pressure drop  $<15\text{ kPa}$  (2.18 psi)

### Constant Bore

The design uses a constant cylinder bore diameter where the displacer and piston diameters are equal. The piston is resonated entirely by the pressure swing in the working and bounce spaces which avoids the complication of an added piston gas or mechanical spring.

### Rod-Through Piston, Resonated by Planar Mechanical Springs

The displacer rod passes through the piston, and the displacer is resonated by planar mechanical springs located in the bounce space. A flexible coupling is used to connect the displacer to the springs, to ease alignment requirements and to not introduce side loads on the displacer gas bearings which are located between the displacer rod and the piston bore.

### Piston-Based Gas Bearings

The gas bearings are completely contained within the piston. The piston interior is pressurized with an internal check-valve which picks peaks of pressure off the compression space. This pressure source then feeds the piston/cylinder bearings (located on the outer diameter of the piston) and the piston/displacer rod bearings (located on the bore of the piston).

### Simple Monolithic Heater Head

We chose a simple monolithic externally reinforced heater head design. Machined axial slots on the outer diameter of the head provide the flow passages for the NaK heating fluid; at the same time the fins transfer the engine pressure load to an outer support structure consisting of a thick stainless steel ring. All head materials in the hottest parts of the machine are 316 SS. A primary feature of this head is that it has no high pressure joints in the hottest region of the machine. The head transitions to IN718 (Inconel 718) in a cooler region part way down the regenerator wall with the joint achieved by using IN625 filler rod.

Internal heat transfer is accomplished with a brazed-in internal copper structure with wire-cut axial helium passages. This design offers simplicity, reliability and low cost manufacture.

### Internal Circumferential Coolant Passages

Next to the regenerator, the rejector (Figs. 5 and 6) is the second most critical heat exchanger to the performance of a Stirling engine. While we are transferring less heat here (73 percent of the acceptor), the importance of temperature on performance is more important by the Temperature Ratio (TR) of the engine (TR=2.2 in the case of the FSP). Thus, the influence of temperature is 1.6 ( $=0.73 \times 2.2$ ) times more important at the rejector. In other words, for every degree drop (coolant to gas) at the rejector, one needs to increase the heater temperature by 1.6° to maintain performance.

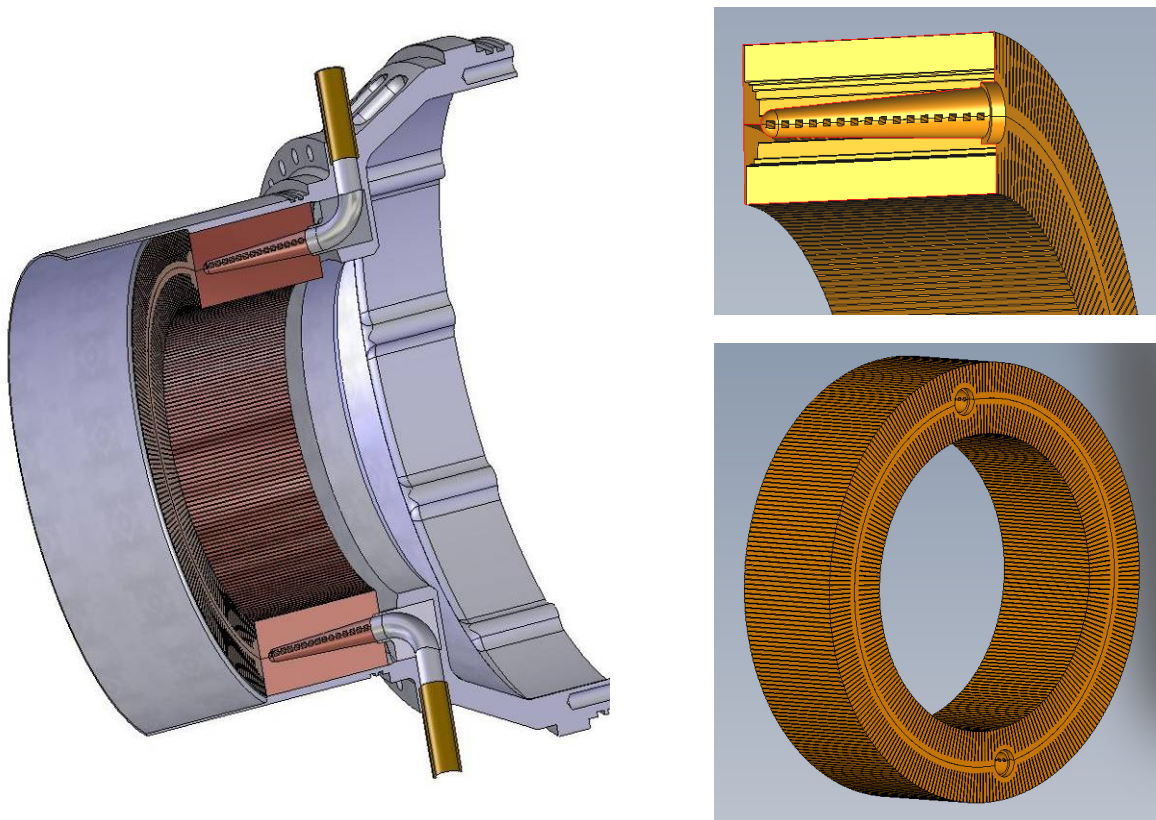


Figure 5.—Rejector construction.

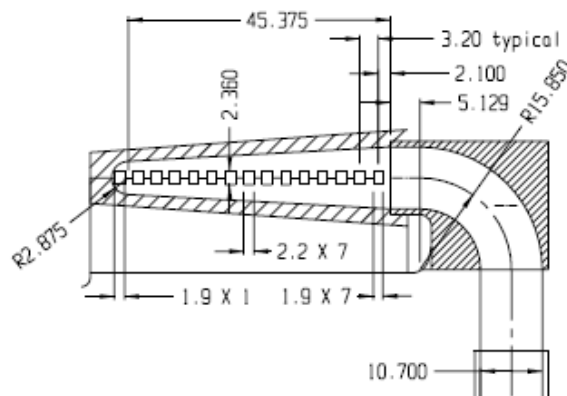


Figure 6.—Water passages.

The rejector design was particularly challenging because of the low water flow rate and low pressure drop requirements given in the statement of work. The requirement is less than 15 kPa (2.18 psi) at  $0.375 \pm 0.125$  kg/sec. We originally tried axial water flow, but the low velocity because of the large perimeter gave very poor heat transfer; also the manifold plumbing proved to be difficult. We therefore chose a circumferential water flow arrangement.

We bring the coolant through the pressure wall of the machine to minimize temperature drops that would exist if transferring the heat through the pressure boundary. To further minimize temperature differences between the coolant and the helium, we bring the coolant to the (radial) center of the heat exchanger. This allows for shorter, more effective fins on both the outside and inside of the rejector water circuit.

Water enters through the transition (conical part of the pressure vessel) then crosses the compression space helium manifold and into a conical water distribution manifold. The water flow then splits into two parallel paths which continue  $180^\circ$  circumferentially. These then combine and exit the machine in a similar arrangement. Each half of the circumferential flow passes through 15 rectangular flow passages. Two different widths of water passages were selected for the design which is discussed more in a later section of this report.

The rejector is machined as an inner and outer half, the water contact surfaces are nickel plated, and then the two halves brazed together and to the inlet and outlet elbows. The elbows are also brazed to the transition joint. Actually, these elbows are fabricated as two (split) halves. This total assembly has only eight pressure joints; six small diameter joints at the inlet and outlet elbows (the split, and the joining to the transition and the rejector), and two larger joints at the ends of the inner and outer main rejector halves. The large joints are deemed low risk as the helium pressure tends to compress these joints.

Half the circumferential water passage is machined into both parts of the rejector so that brazing is not required internally since the heat flux across the water fin contact area is zero. On the helium side surface, there are 520 total (290 outer and 230 inner) helium passages 0.396 mm wide 13.77 high.

Our P2A engine and the production machines derived from it, also have a similar circumferential flow circuit with water being brought in through the pressure boundary. However, as the heat transfer is less challenging and the radial width of the rejector is shorter in the smaller machine, the water flow circuit is adjacent to the outer pressure wall instead of being in the radial center of the heat exchanger.

### **Displacer**

There is little difference in the displacer design than that of our other machines. The only difference, except for size, is that we have selected a flat top design for the displacer. Based on the engine coupling trade-space discussed later, we selected a common expansion space with a simple straight tube form for the heater head.

With the common expansion space, we first considered making the displacer of one machine with a conventional convex dome, and the other with a concave dome. While some raised the question of non-symmetric flow within the expansion space, we doubted that this was a significant concern. However, in performing stress analysis of the convex dome, we found the stresses to be quite high which led us to the flat top design for both displacers. We also investigated supporting the flat displacer tops with an added domed baffle to minimize the thickness. However, this would have required a braze joint for support which was both critical and not easily inspected. For simplicity and reliability, we decided to use the simple flat topped form and simply thicken this to achieve adequate stress levels. The entire displacer assembly is fabricated of IN718.

### **Regenerator**

The regenerator is made of sintered random 91 percent porosity fiber. For fiber size, we used that of Bekaert 22  $\mu\text{m}$  material.

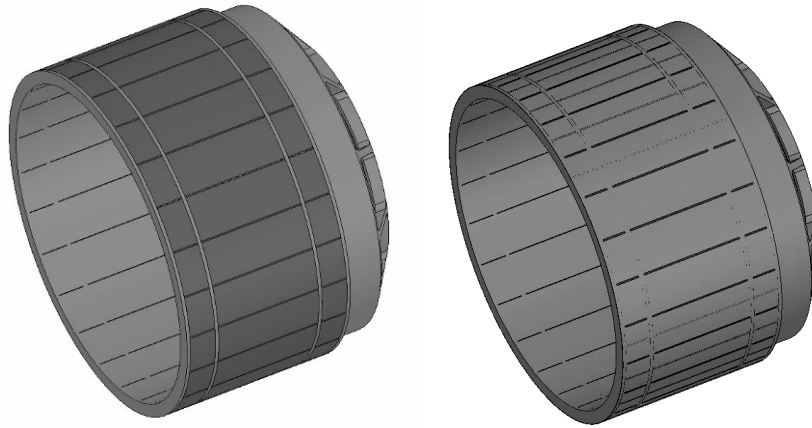


Figure 7.—Magnet can construction (without and with the outer cover sheet).

### **Alternator**

The alternator design is a typical Sunpower single-window moving-magnet arrangement. The magnet can is titanium with integral machined stiffening rings that besides providing circular rigidity also contain the magnets axially. R29HS Sm-Co magnets are bonded with Master Bond EP21TCHT-1 (4 to 478 K°C) epoxy to the outer surface of the magnet can. For added reliability, an outer containment sheet of titanium will be laser welded to the outside of the assembly. The outer shell, as well as the inner can will have axial slits aligned with the axial center of the individual magnets to reduce eddy current losses. All the enclosed magnet space gaps will be potted with the adhesive. The magnet can with and without the cover sheet is shown in Figure 7.

The longer central magnets are the main magnets. The short magnets at each end are spring magnets that will provide static centering of the piston, and also add to the power capability of the alternator. These have the opposite polarity of the main magnets (all main or spring magnets each have the same polarity). Spring magnets are used in several of our commercial machines but usually with only a few magnets at each end because of the added cost. There are 24 individual magnets per ring; the large number of magnets in each ring helps reduce eddy current losses within the magnets themselves. More information on the alternator is provided in a later section.

### **Internal Acceptor Design**

As mentioned earlier, the internal acceptor is OHC copper and brazed to the inside of the heater head. There are 150 helium gas passages 0.516 mm wide by 34.81 mm high cut into this by wire EDM. The outer diameter of the copper is solid 1.5 mm thick material. The inner diameter of the copper is also solid, here being 6 mm thick.

The expansion space end of the acceptor, shown in Figure 8, includes additional short tapered fins which serve two purposes. First, they fill some manifold volume at the outer diameter where the manifold gas flow is the least. Secondly, they transfer heat from the stainless heater head wall to the leading edge of the heat exchanger where the heat flux is the largest. The heat flux profile along the acceptor is shown later in the CFD modeling section of this report (Fig. 86), the expansion space end heat flux is over twice that of the regenerator end, and these short tapered fin sections help to reduce the heat load on the leading edge. The internal acceptor for the two convertors will be machined separately to ease fabrication, then brazed to the inside of the head as well as to each other where the short fins meet on the centerline.

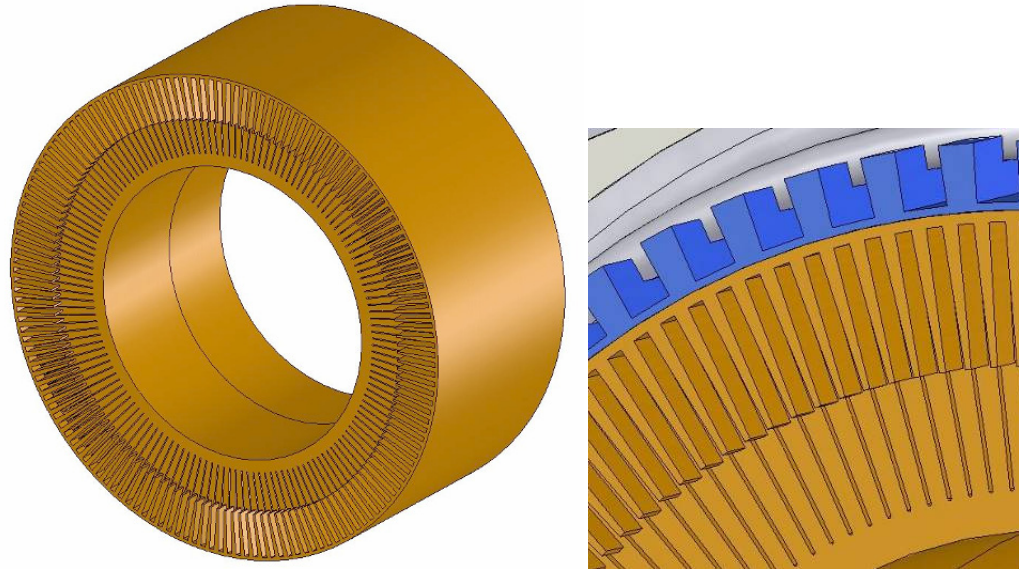


Figure 8.—Short tapered fins in expansion space manifold.

### Summary of Heat Exchanger Dimensions

Table 2 summarizes the heat exchanger passage geometry.

TABLE 2.—HEAT EXCHANGER PASSAGE SUMMARY

	Number	Length (mm)	Width (mm)	Height (mm)
NaK Passages	66	84	6.00	4.50
Acceptor Internal Helium	150	90	0.516	34.81
Water Passages (180° circumferential flow)	15 by 2	259	Variable: 1-7= 1.9, 8-14= 2.2, 15= 1.9	2.36
Rejector Internal Helium	520	55	0.396	13.77

### NaK Heating Circuit Design

After much study and review, we selected a tangential-inlet scroll manifold and an offset circular outlet manifold with a radial-outlet for the NaK circuit design (Fig. 9). Early attempts with an inlet of the same design as the outlet (radial flow) did not give uniform flow. Largely, this was because of flow impingement on slots directly under the inlet. Several attempts with CFD modeling were made to design internal baffles to prevent this non-uniform flow, but no adequate solution was found. The tangential inlet selected gave very good results after only one design iteration. Basically, this involved sizing the amount of “recirculation flow” or the minimum area of the scroll where excess fluid feeds back into the initial flow. Consultant David Gedeon proved insightful here, and after reviewing the flow fields and pressures in the original design predicted the next iteration, which proved to give very good flow uniformity.

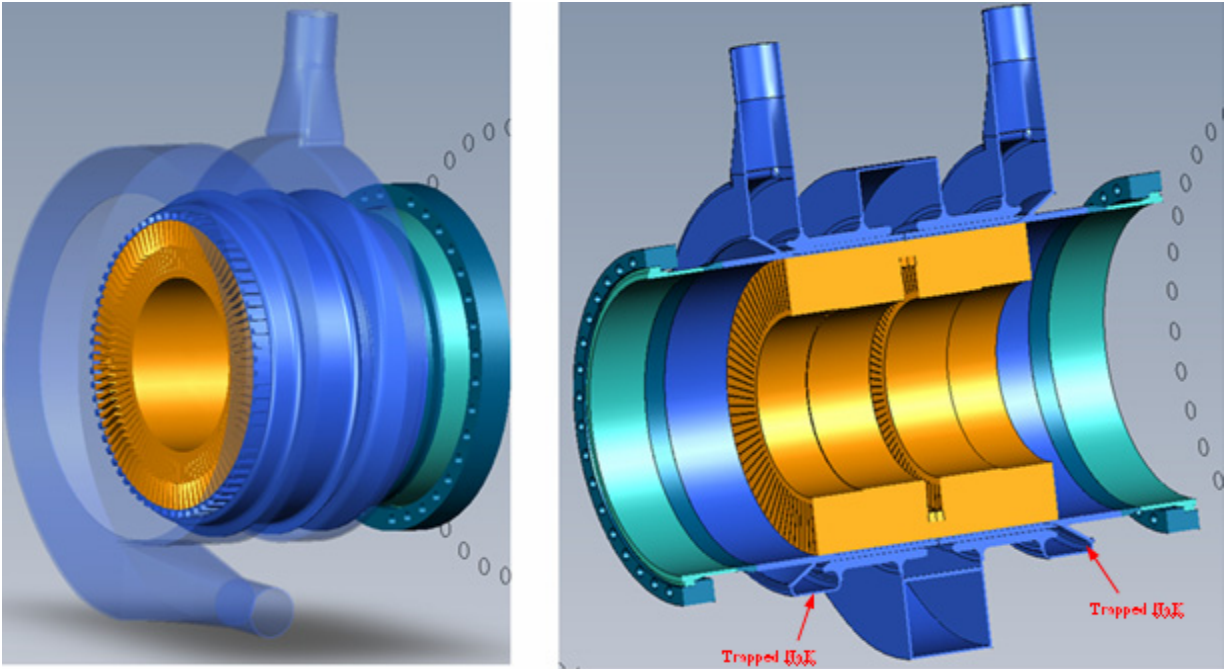


Figure 9.—NaK heating circuit.

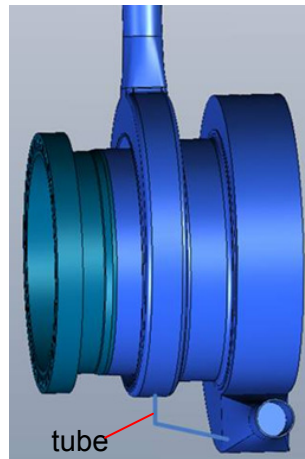


Figure 10.—Possible tubing to drain NaK (not used in the design).

To minimize pockets where NaK would remain after draining of the heating system, we decided to place the tangential inlet at the bottom and the radial outlet at the top. In this case, only about 50 cc of NaK in each outlet will not drain, located in the narrowest part of the outlet manifold below the axial slots.

Complete draining would be possible with the use of a small tube (Fig. 10) on each head from the bottom of the trapped outlet pocket to the inlet pipe. This would, of course, allow a small amount of flow to bypass the main heat exchanger passages during normal operation. Subcontractor Rocketdyne (who acted in an advisory role on the NaK circuit and heater head design) advised that such a tube was a reliability risk and not worth the effort. They advised it would be better to plan for flushing out the small amount of trapped NaK.

We expect the outlet manifold will be fabricated by spinning because this is basically a circular shape. The tangential inlet is more complicated to manufacture and we anticipate it to be fabricated by the welding of separate sheets of material.

Basic dimensions, materials and joints for the heater head assembly are shown in Figure 11. The maximum scroll height is 70 mm at the inlet from the tops of the fins and 14 mm at its shortest height. The inlet NaK pipe is 38 mm (1.5 in.). The outlet manifold is 295 mm inside diameter and its axis is offset 16.25 mm from that of the convertor. The outlet piping is also 38 mm diameter (1.5 in.) in diameter. The thick head support tubes are 6.5 mm thick and heat shrunk onto the head fins.

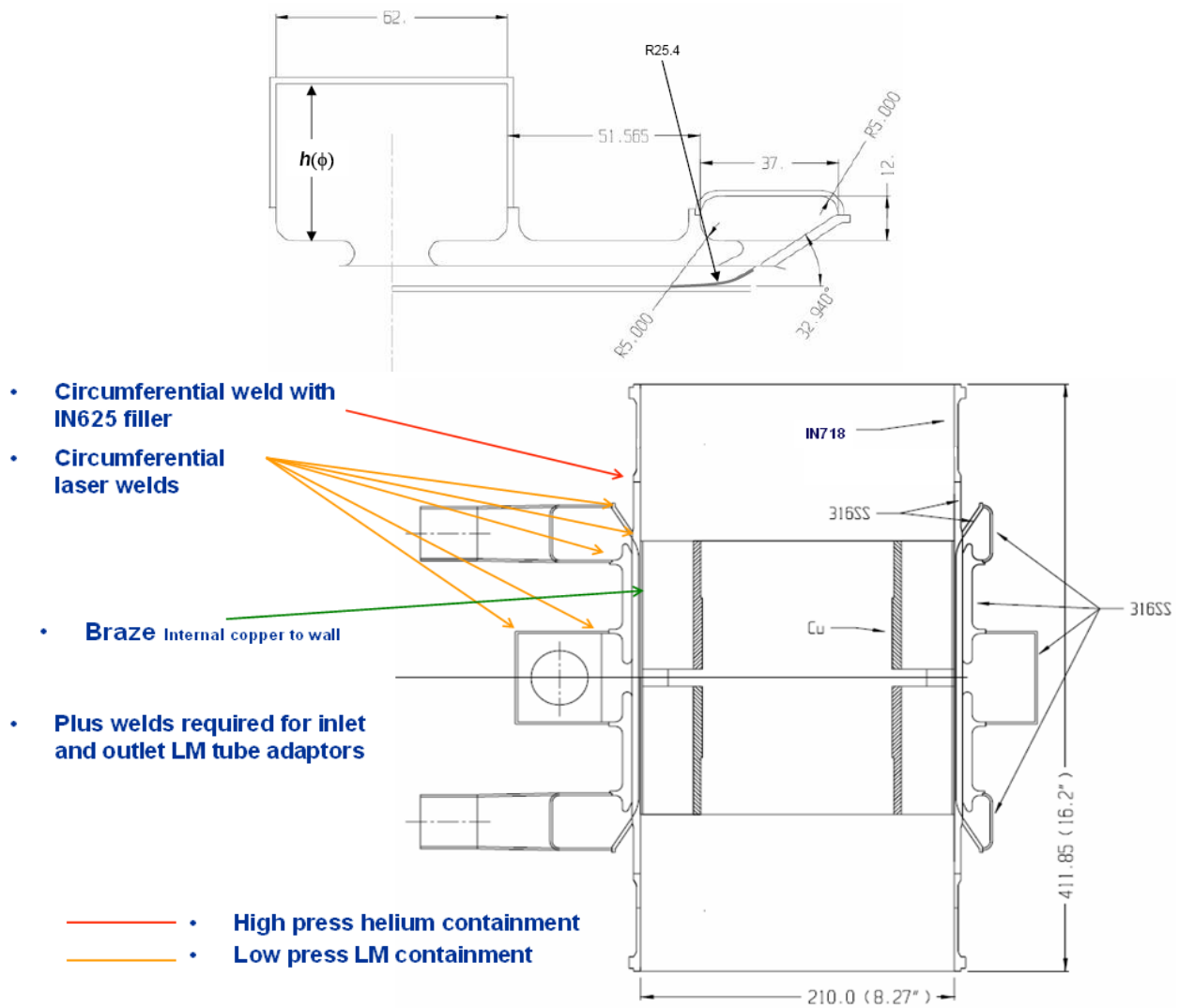


Figure 11.—NaK manifold construction arrangement and all head joints.

## Prototype Bolted Converter With O-Rings

In the design, we gave consideration to the basic design for final sealing, although the prototype to be delivered is not required to, and likely will never, be hermetically sealed. Figure 12 shows the bolted converter which would be fabricated and delivered. Two large removable clamping flanges are utilized on each converter. Long bolts here are used to pass over the outside of the alternator cooling jacket. Each head attachment uses a single captured loose flange with bolts that thread into the transition. “Captured” implies that these head flanges must be in place during head welding and they are not removable except by cutting. The bolted converter thus has a total of six loose flanges that ultimately could be removed after welding.

In the design, we have provided for two O-rings in series at the four large diameter sealing joints (two pressure vessel and two head joints). The series O-rings reduce the permeation rate of helium and will thus extend the charge life of the unit. We plan to use polyurethane O-rings because of their very low permeability. However since this unit can be subject to cold soaking in a vacuum chamber the question arose as to the survivability of polyurethane at temperatures approaching  $-100\text{ }^{\circ}\text{C}$ .

We, therefore, placed a polyurethane O-ring on a stainless rod and placed this in liquid nitrogen ( $\sim -200\text{ }^{\circ}\text{C}$ ) for 15 minutes to test its survivability. The O-ring survived this test and was still flexible on the return to room temperature. Thus we have selected polyurethane as the baseline with the back-up option of silicone as it is known good to  $-100\text{ }^{\circ}\text{C}$ , however, silicone has a permeability of 17 times that of polyurethane at  $80\text{ }^{\circ}\text{C}$  where data is available. Silicone will be used for the internal cylinder seals (one on each converter) because permeability is not a concern in these areas.

Series polyurethane O-rings were also used in field trials of our P2A units in Europe. Units in that application would not need to be recharged for more than 3 months, although the pressures in that application was half that of the FSP. The seals there were smaller diameter of course, but also the volume of gas contained was lower.

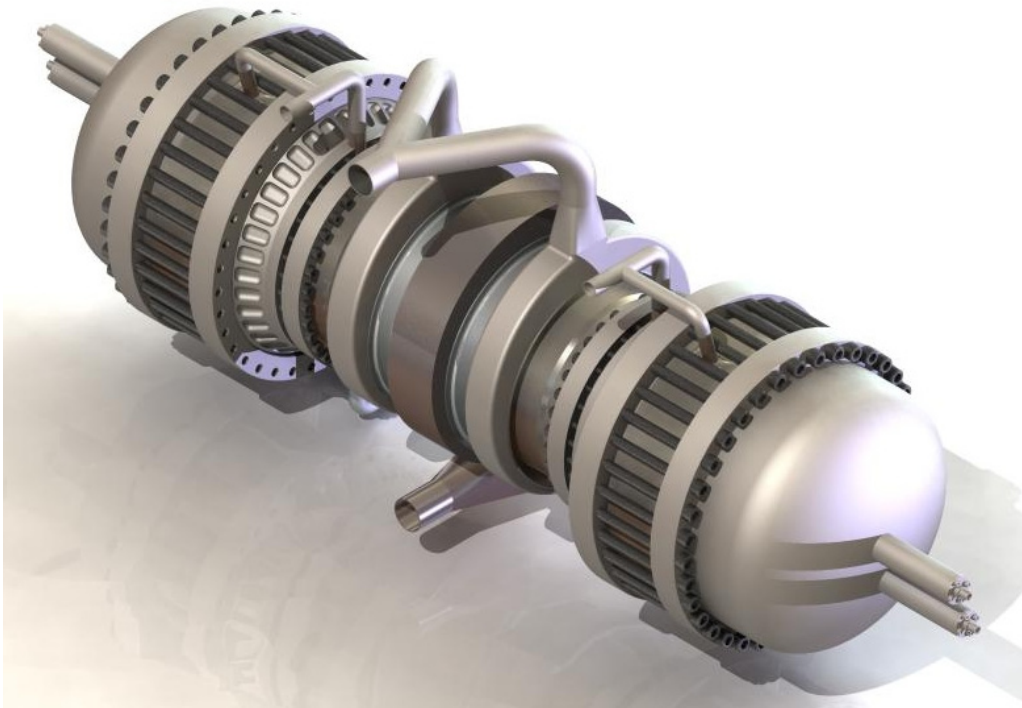


Figure 12.—Outer view of bolted converter.

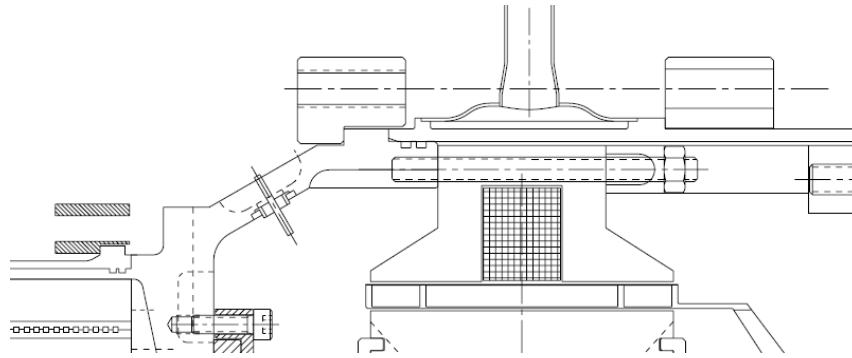


Figure 13.—Cross-section showing vessel cooling water jacket.

### Alternator Cooling

The design alternator efficiency of 90 percent indicates that we will be generating 670 W of heat at the alternator, which equals 4 percent of the total heat rejection. We, therefore, will provide 4 percent of the coolant flow to the outside of the pressure vessels. The design (Fig. 13) includes an annular gap around the pressure vessel, to which a closeout sheet-metal strip will be welded. As in the rejector, the flow here splits and proceeds half way around the vessel. Inlet and outlet manifolds for the water flow will be formed into the closeout sheet.

We estimate about a 30 °C temperature difference between the alternator and the vessel. Our instrumentation detailed later includes alternator thermocouples which will be used to check this number in early testing.

### Design Point

Table 3 lists the basic design point conditions.

TABLE 3.—DESIGN POINT CONDITIONS

Power output (Wac) .....	6000
AC eff (see note) % .....	27
Mean operating pressure (MPa) .....	6.2
Frequency (Hz) .....	60
Piston amplitude (mm) .....	16
Displacer amplitude (mm) .....	12
Displacer phase (deg) .....	60
Pressure amp comp space (MPa) .....	0.789 at -14.9°
Pressure amp bnc space (MPa) .....	0.22 at -180°
Pressure amp exp space (MPa) .....	0.755 at -16.6°
Mass piston (kg) .....	5.2
Mass displacer (kg) .....	1.41
K displacer (N/mm) .....	224.1
Volume bounce space (liter) .....	9.2
Drod (mm) .....	19.8

Note: Uses 12.5% correction factor on SAGE

As noted, a 12.5 percent correction factor has been applied to Sage, meaning that this value is 87.5 percent of the prediction. This factor is a bit arbitrary as we have no recent experience with an engine of this power level. The ASC class machines typically require a 14 percent correction; where little if any correction is required for our P2A. Thus, this 6 kW size may be closer to the Sage prediction, but we felt it unwise to not include a good bit of conservatism in the prediction.

## Materials and Adhesives

The materials of construction (shown by color code for materials in Table 4) are shown in Figure 14.

Adhesives are used primarily as potting in the construction of the alternator. Master Bond EP21TCHT-1 (4 to 478 K) was chosen because the convertor must survive possible low temperatures in the thermal vacuum when not operating and generating heat. The epoxy is used for potting of the coil winding, and for attaching the outer laminations to the coil. It is also used to bond the magnets and as potting of the magnets to the magnet can. The fanned inner laminations will also be potted with this material.

TABLE 4.—COLOR CODE FOR MATERIALS

UNS	Common Name	Trade Name	Color Code
A94032	Aluminum 4032-T6		
A97075	Aluminum 7075-T6		
C10100	Oxygen-free Copper		
F41000	Type 1 Austenitic Cast Iron	Ni-Resist Type 1	
G41300	Steel 4130		
N06625	Inconel 625		
N07718	Inconel 718		
R56400	Ti-6Al-4V		
S31600	Stainless Steel 316		
	Martensitic Stainless Steel	Uddeholm 716	
	ASTM A801 Alloy Type 1	Hiperco 50	
	High Temperature Material		
	Feedthrough Ceramic	Kryoflex	
	Sm-Co Magnet	R29HS	
	400 Series Stainless Steel		

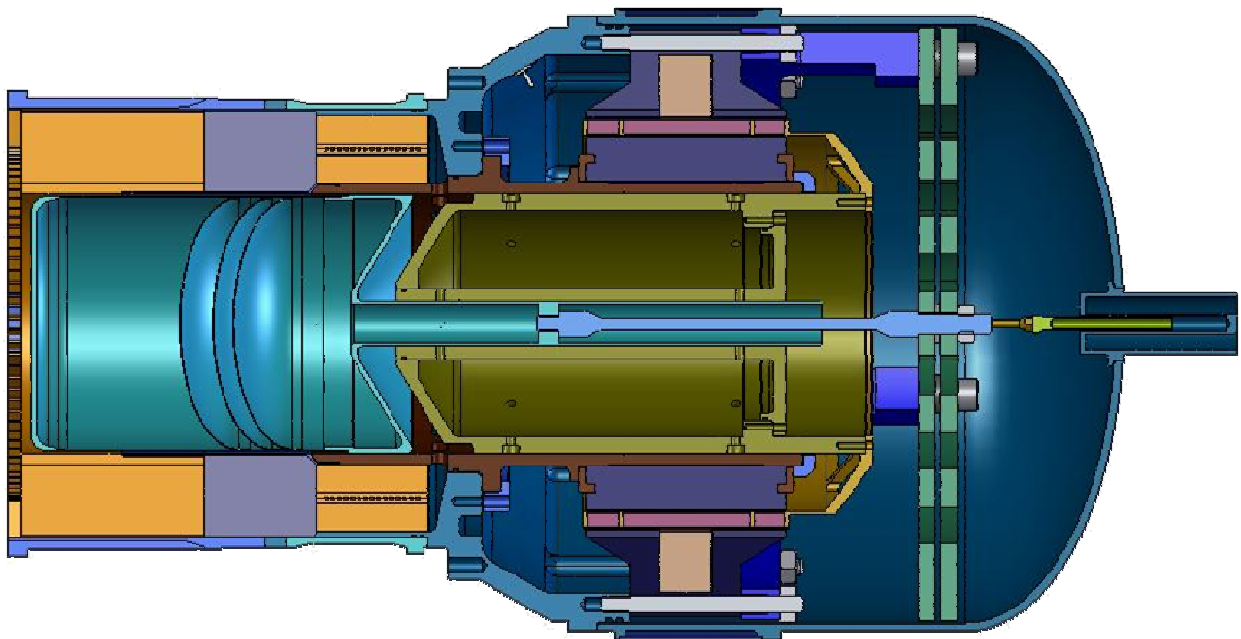


Figure 14.—FSP materials.

## Cost Savings with Stainless Steel (SS) Vessel

Table 5 gives an estimate of the cost savings of making the pressure vessel and transition of SS-316 compared to the baseline IN625 vessel.

TABLE 5.—COST SAVINGS USING STAINLESS STEEL IN CONSTRUCTION  
OR COST SAVINGS IN REDUCING PRESSURE VESSEL DIAMETER

	Material	Shop (hr)	Shop	Per conv	Total	Save
IN625	\$28,100	208	\$16,600	\$44,908	\$89,816	
SS-316	\$4,000	96	\$7,700	\$11,796	\$23,592	\$66,224
If reduce diameter by 3 mm and take alternator penalty						
IN625	\$23,700	192	\$15,300	\$39,192	\$78,384	\$11,432

Also, presented in Table 5 is the savings if the IN625 vessel diameter was reduced by 3 mm, since this would allow the use of 12 in. instead of 14 in. bar stock which is adding to the cost. As shown later, in Figure 23 in the alternator section, this would drop convertor efficiency by only between 0.2 and 0.3 percent, and reduce mass by about 0.5 percent. The same could be done with the SS-316 vessel but this would require a drop in diameter of 8 mm which would result in a larger penalty (~1 percent) and only save an additional \$2500 for the opposed unit. Note here that the IN625 test vessel maximum diameter is 308 mm which includes a 3.5 mm radial step that forms the water jacket, and provides a lip for the clamping flange.

The use of SS-316 requires that the wall be increased to 6.5 mm thick compared to 4.0 mm for IN625. Also we would omit the lightening pockets in the transition. This would add about 14 kg of mass to the opposed pair.

## Instrumentation

The following is a list of instrumentation planned for testing. The number listed is per convertor unless noted: (TC=thermocouple; Tr=thermistor)

- Acceleration
  - One Accelerometer: One axial located on alternator enclosure of one convertor
- Pressure
  - Mean bounce space pressure: Electronic pressure transducer
  - Dynamic pressure in working space (removed prior to thermal vacuum)
- Position
  - Two FLDTs (displacer and piston):
- Temperature (all TCs are type K)
  - Four TC-Alternator Enclosure: at mid-length (spaced 90°)
  - Two TC-Alternator winding: (top and bottom)
  - Two TC-Bounce space gas: (top and bottom)
  - Six TC-Rejector copper solid: three each along the length near both the inlet and outlet axial water plenums (may or may not be connected during thermal vacuum testing)
  - Six TC Hot end of regenerator wall (60° spacing)
  - Four TC NaK outlet manifold wall (top, bottom, and two sides)
  - Four TC NaK inlet manifold wall (top, bottom, and two sides) \*
  - Four TC Head Support Tube (top, bottom, and two sides) \*
  - One TC + one Tr Water inlet
  - One TC + one Tr Alternator water jacket outlet
  - One TC + one Tr Rejector water outlet

\*Because of the larger outer diameter

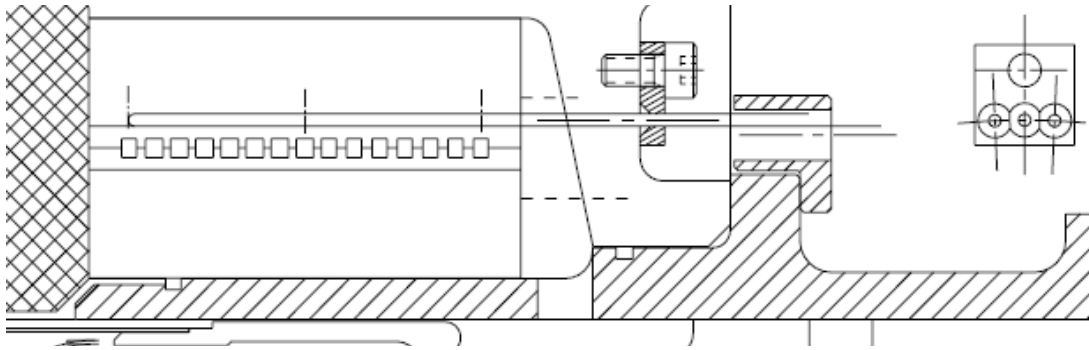


Figure 15.—Planned implementation of rejector solid thermocouples.

Certain of these instruments need not be connected when placed in thermal vacuum, and would thus simplify the connecting cabling. For instance, it is not absolutely necessary that both or either of the bounce space gas thermocouples in both convertors be connected. Also, the rejector copper solid thermocouples listed are intended primarily for early testing to verify the predicted temperature distribution here, and are not needed during later testing.

Both displacer and piston FLDTs are included on the prototype convertor. However, a final hermetic convertor would likely have only the piston FLDT. In a hermetic unit, we envision this as having a special construction with the winding located outside the pressure boundary as shown in Figure 14. The prototype convertor will have more conventional FLDTs for both the displacer and piston as shown in Figures 2 and 3. These FLDTs are threaded into the vessel and sealed by O-rings. These threaded FLDTs have been used extensively with our P2A engine.

Note, as shown in Figure 2, that the displacer FLDT is off-center and driven by a leg attached to the inner spring connection. The piston FLDT is driven by a 'bridge' that passes through the displacer spring. This requires that the piston not rotate more than  $\sim \pm 30^\circ$  during operation. The piston will be prevented by rotating by leaving a small circumferential gap in the magnets, and an equivalent gap in the outer laminations where they touch at their inner diameter. This will form a rotational magnetic spring which makes these gaps want to line up. The magnet gap is formed by pushing all magnets together so they touch except at one location. The gap in the laminations is also beneficial in coil winding and allows the wire at the inner diameter of the coil to exit the alternator.

The means of installing the thermocouples for measuring the rejector solid temperatures (three near water inlet and three near the outlet) is shown in Figure 15. Axial holes will be put in three adjacent fins at differing depths and thermocouples brought out through holes in the transition. Sealing is accomplished by small O-rings in the clamping plate.

## Mass Breakdown

Tables 6 and 7 give the mass breakdown for the convertor and the controller respectively. The combined convertor mass for the convertor plus controller is 256 kg ( $= 94 \times 2 + 68$ ).

TABLE 6.—CONVERTOR MASS BREAKDOWN  
 (Convertor masses are for a hermetically sealed IN625 Vessel)  
 (316 SS vessel and transition would add ~14 kg and save \$66,000)

Part	Mass (kg)	Weight (lb)	Percent
Alternator	24.051	52.9	25.60
Internal acceptor	16.296	35.9	17.35
Transition	9.891	21.8	10.53
Thin DV dome	9.348	20.6	9.95
Internal rejector	7.102	15.6	7.56
Springs (2)	6.174	13.6	6.57
Cylinder	4.71	10.4	5.01
Head (support cylinder)	3.737	8.2	3.98
Outer piston	2.25	5.0	2.40
Head (finned tube)	1.814	4.0	1.93
Spring support	1.8	4.0	1.92
Head (flange end)	1.732	3.8	1.84
Displacer body	0.811	1.8	0.86
Regenerator	0.766	1.7	0.82
Displacer dome	0.542	1.2	0.58
Magnet can	0.482	1.1	0.51
Inner piston	0.464	1.0	0.49
Inner iron end rings	0.458	1.0	0.49
Hot cylinder	0.327	0.7	0.35
Cylinder clamping flange	0.302	0.7	0.32
NaK ring	0.294	0.6	0.31
Inner iron clamp ring	0.276	0.6	0.29
Displacer baffle (3)	0.208	0.5	0.22
Flex rod	0.1	0.2	0.11
Total	93.935	206.7	

TABLE 7.—CONTROLLER MASS BREAKDOWN

Qty	Description	Unit Mass (kg)	Extended Mass (kg)
2	LC Filter	18	36
2	Convertor Power Stage	0.2309	0.4618
5	730 $\mu$ F HV Bus Capacitor	1.3	6.5
2	Heat Sink for Power Stage	1	2
1	DSP Board	0.08543	0.08543
1	DC/DC Power Stage	0.089	0.089
3	600 $\mu$ F 120 V Bus Capacitor	0.544	1.632
1	DC/DC Heat Sink	1	1
1	DC/DC Transformer	2.5	2.5
1	Synchronous Rectifier	0.12	0.12
1	Shunt Controller	0.8	0.8
1	Shunt Heat sinks	1.5	1.5
1	Shunt Resistors	15	15
	Total		67.7

## Alternator Design, Trades and Analysis

The magnetic Finite Element Analysis (FEA) results are shown in Figure 16. For simplicity, these are modeled as representative axisymmetric two-dimensional models while the alternator is not truly axisymmetric. To account for this, the lamination form is adjusted to give the correct magnetic material area. As our outer laminations are in stacks (seen in Fig. 17), these are modeled in the 2D FEA by tapering the radial lamination legs and thinning the outer axial leg to give the correct volume. Fields are

presented in Tesla, and flux is in Webers. Local areas shown in red represent local saturation, which in itself is not a problem as long as the entire cross section is not saturated.

Presented are results at maximum current (peak piston velocity or mid-stroke), maximum magnet induced flux (peak position and zero velocity), and the peak flux level which occurs between the first two cases.

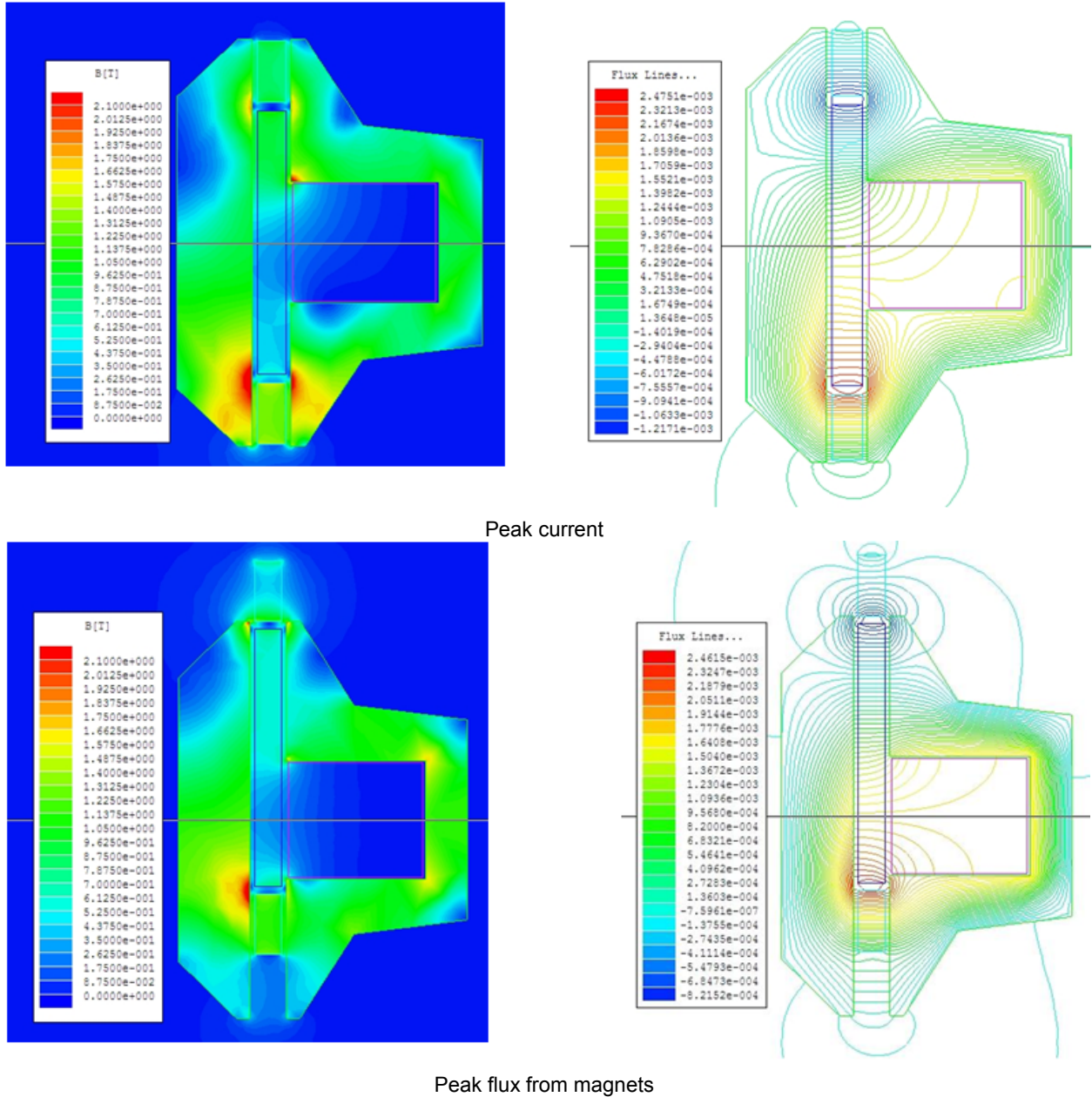
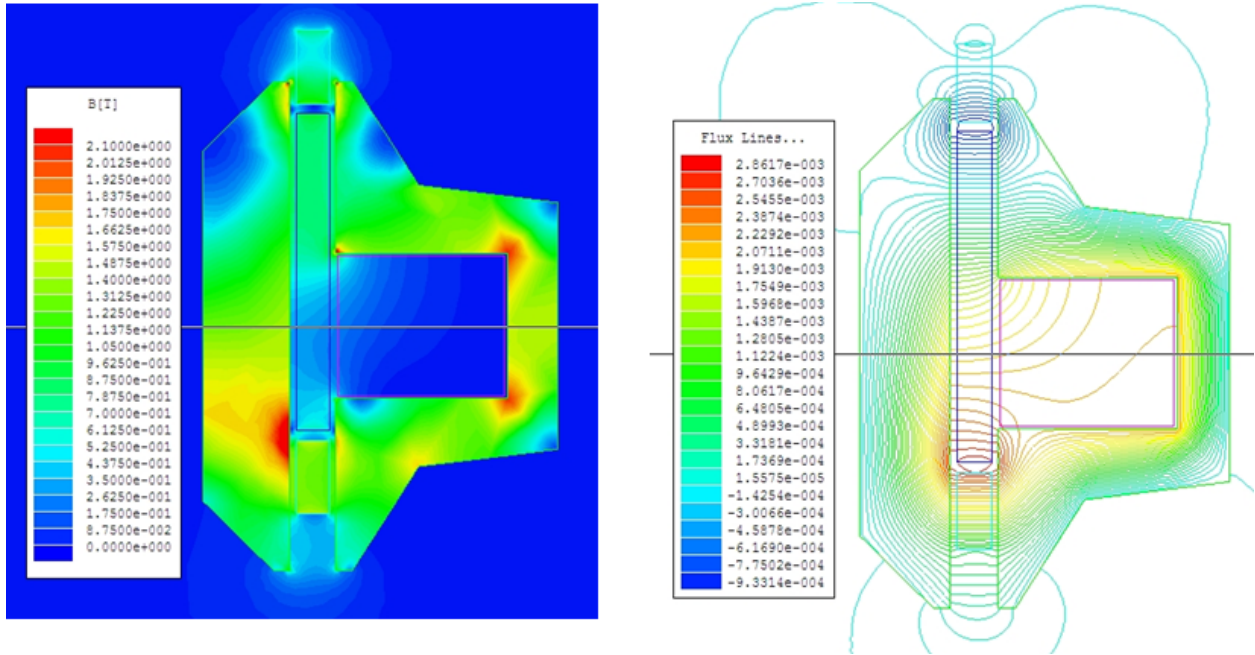


Figure 16.—Alternator flux.



Peak flux in laminations

Figure 16.—Concluded.

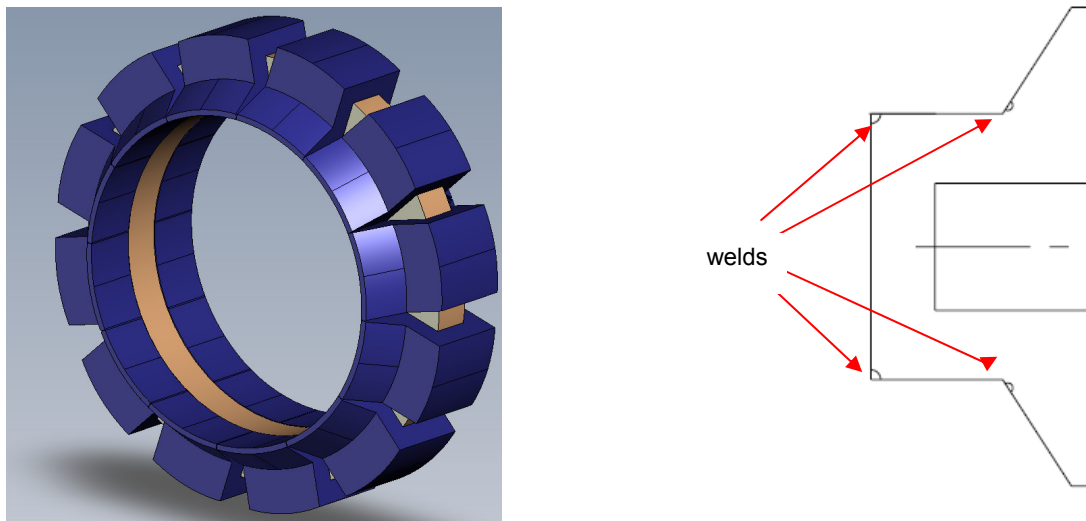


Figure 17.—Outer stator and location of stack joining welds.

The inner lamination will naturally fan because of the design of the end rings. These will then be potted, with the same adhesive as used to bond the magnets. The individual outer lamination stacks will each be welded in four locations as shown in Figure 17. These also are then potted to the coil winding to complete the outer lamination assembly.

In essence, the epoxy is only required to be a bond agent during assembly. Once the magnet can and outer laminations are finished and installed, the epoxy acts much more as a filler or potting material. Thus, the strength requirements are minimal.

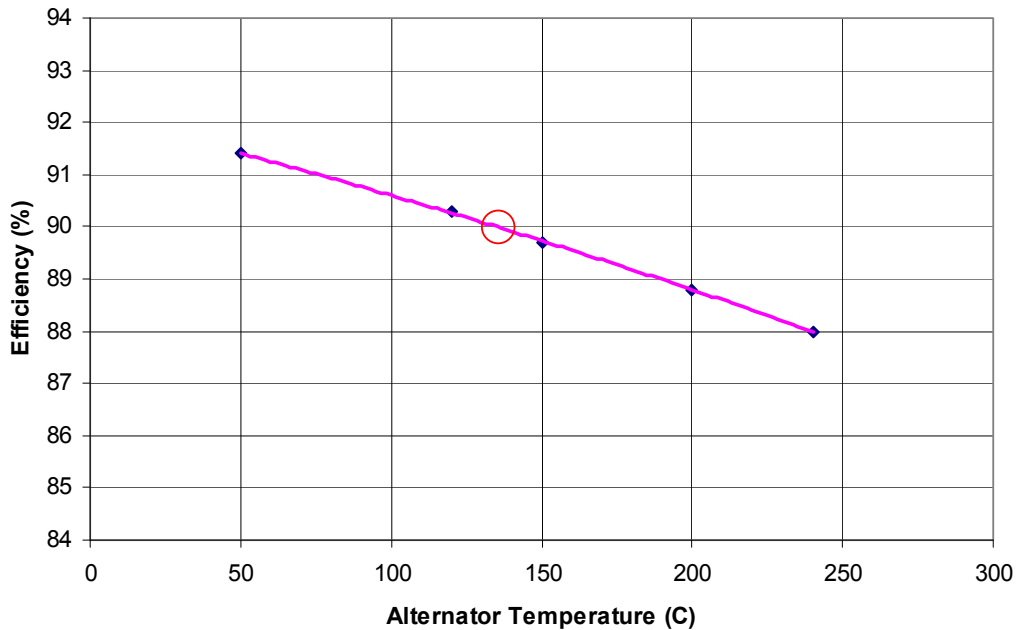


Figure 18.—Alternator efficiency versus temperature.

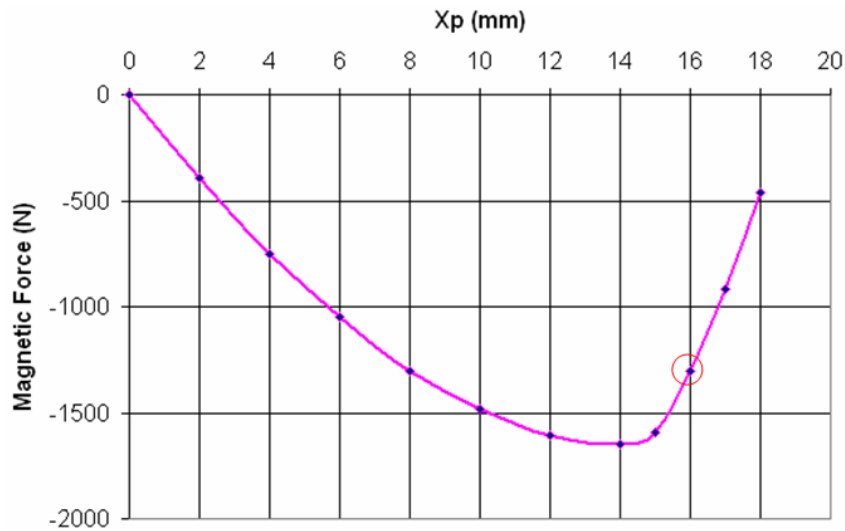


Figure 19.—Alternator magnet spring force versus position.

Figure 18 presents the alternator efficiency as a function of temperature. The primary reason for efficiency falling with temperature is the increasing resistance of the copper coil winding, which increases RAC (AC resistance) losses. The red circle indicates the design point.

Figure 19 presents the magnetic spring force. The effective spring at 16 mm amplitude is 139 N/mm, which will resonate 978 gm of mass at the 60 Hz. operating frequency. The mass of the spring magnets is 1090 gm so that the spring magnets essentially resonate their own mass. The effective spring constant (based on stored energy) does change with amplitude as is shown in Figure 20. This will result in a small change in alternator power factor since the frequency is fixed by the controller. The net increase or drop in magnetic spring is a small number compared to the entire spring acting on the piston (caused by the workspace and bounce space pressure waves).

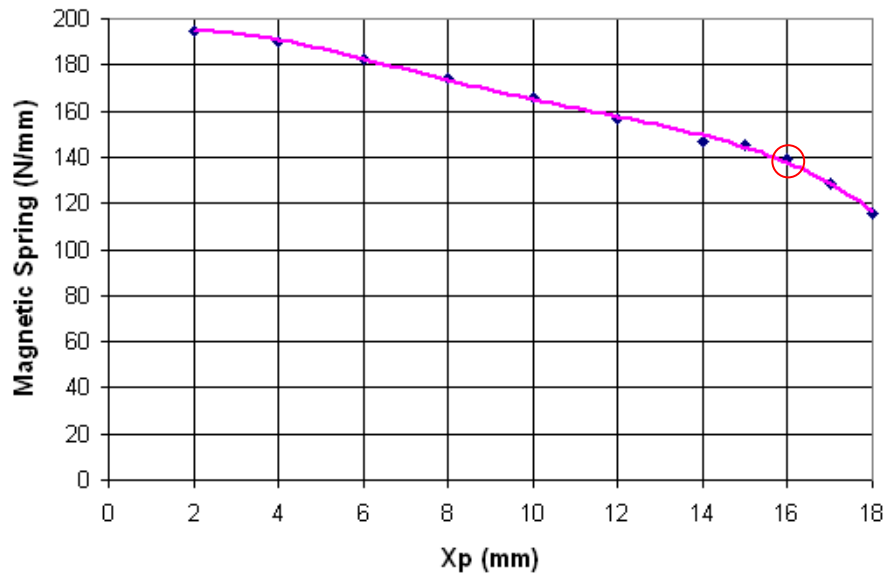


Figure 20.—Alternator effective spring constant versus piston amplitude.

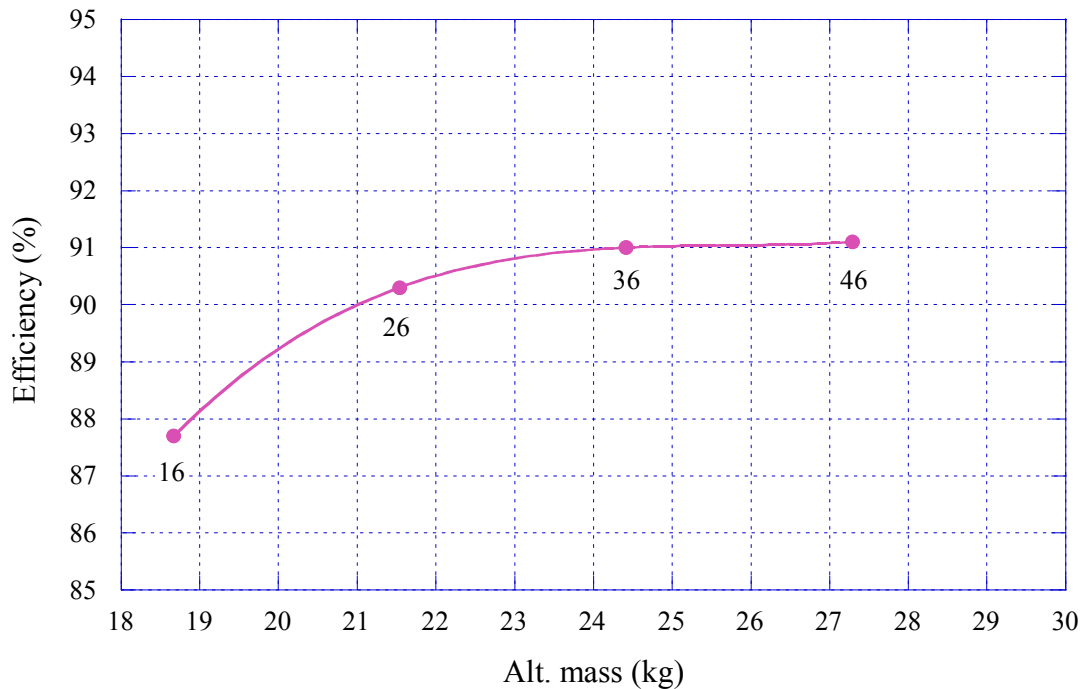


Figure 21.—Alternator efficiency and mass with different coil winding widths (OD=290 mm).

Figures 21 and 22 show the tradeoffs in the single window alternator design with values presented at 120 °C. Our design point is 21.5 kg, 290 mm outside diameter, and a 26 mm copper window width operating at 135 °C. Although these plots are at a different temperature than the design, the trends will be the same. As seen, our design falls roughly at the knee of the curves. Of course, the alternator diameter influence on converter mass is magnified since this also determines the vessel diameter. Also, a smaller diameter would influence the displacer planar spring design and would typically require that more springs of reduced thickness be used. It should also be noted that changing the window width will change the length of the main magnets and thus the total moving mass of the piston.

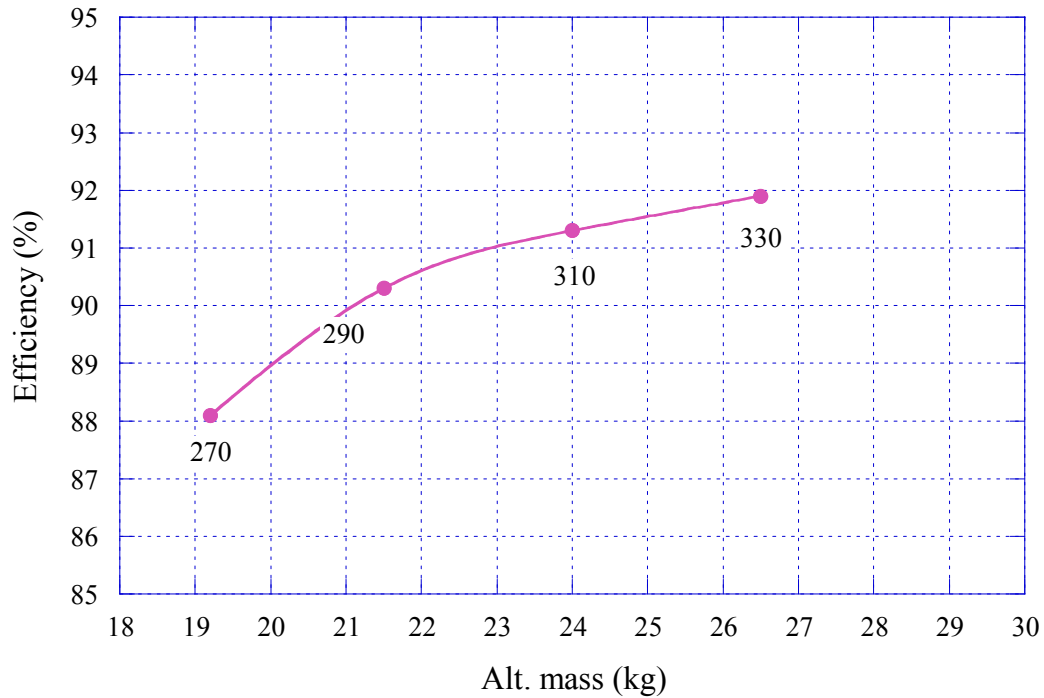


Figure 22.—Alternator efficiency and mass at different outer diameters (window width = 26 mm).

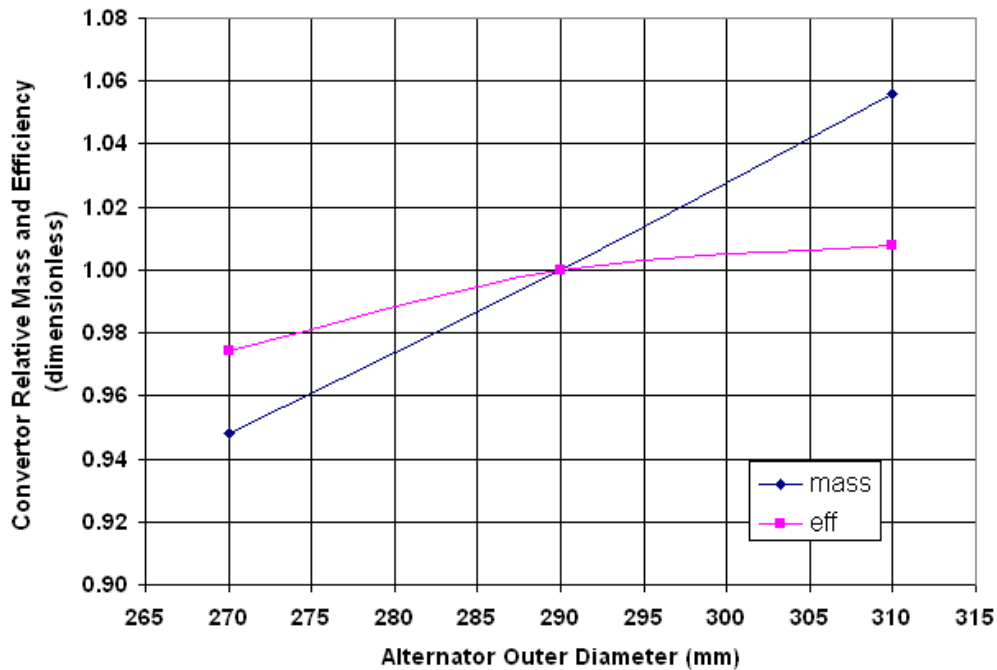


Figure 23.—Converter relative efficiency and mass with different alternator diameters (w = 26 mm).

An approximate calculation can be made regarding the influence on converter mass and efficiency with a change in alternator diameter. If it is assumed that the mass of the pressure vessel and transition (19.2 kg total from Table 6) varies as the square of the vessel diameter, then this is added to the alternator mass change alone. Figure 23 shows this trade. Note that the “square” term comes from the fact that as the vessel diameter increases the wall thickness must also. This of course assumes all other design parameters are not changed.

## Testing and Development Plans

### Convertor Development/Testing Plans Prior to Delivery

We plan to test individual convertors first, before combining the opposed unit. This is the technique used in the past even on our 1 kW engines. While an absorber could be designed for this testing to limit housing motion so that displacer dynamics would be representative, we decided to bolt individual engines to a large mass. Figure 24 shows such testing on the Sunpower 1 kW P2A convertor where a 1080 lb weight was used. For the FSP individual engine testing, we would scale this up to 4000 lb. One can liken this to how individual convertor testing of the original MTI opposed SPDE convertor was later tested as individual SPRE convertors bolted to very large masses.

### Developmental Testing With Electric Heating

For heating the individual convertors and for the opposed unit at Sunpower, we will utilize special heater heads (both a single and an opposed head) that are all IN718 and have a smooth heated outer surface instead of fins. Electric heating will be supplied by strapped on heaters shown in Figure 25.

This will consist of 10 sections of copper each containing three 1 kW stock cartridge heaters for a total of 30 kW available heat. The reason for separate sections is to allow replacement, as it can often be difficult to remove these heaters from the conductive material. The sections will be bolted to a split outer Inconel sheet (bolts not shown) and clamped to the head with draw bolts and Inconel Bellville washers. The baseline design is to nickel plate the copper sections, but an alternate corrosion resistant coating such as Cu ~20 percent Cr will be used if we can find a plating house capable of applying this coating. The opposed convertor would use two of these heater assemblies.

Because this will give a more uniform axial temperature distribution than the NaK heated head, we will use Sage to predict the uniform temperature which should give the same performance as with NaK heating.

As stated, testing would be performed on individual convertors and then on the assembled opposed pair. Prior to delivery, the LM head would be installed and the unit motored as a cryocooler to check out operation prior to delivery.



Figure 24.—P2A tested on 1080 lb weight.

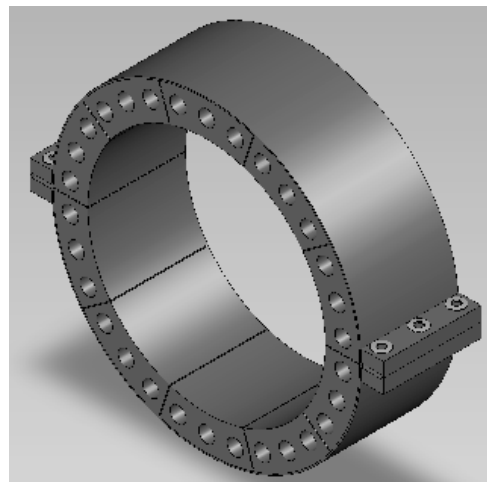


Figure 25.—Clamp-on electric heating arrangement

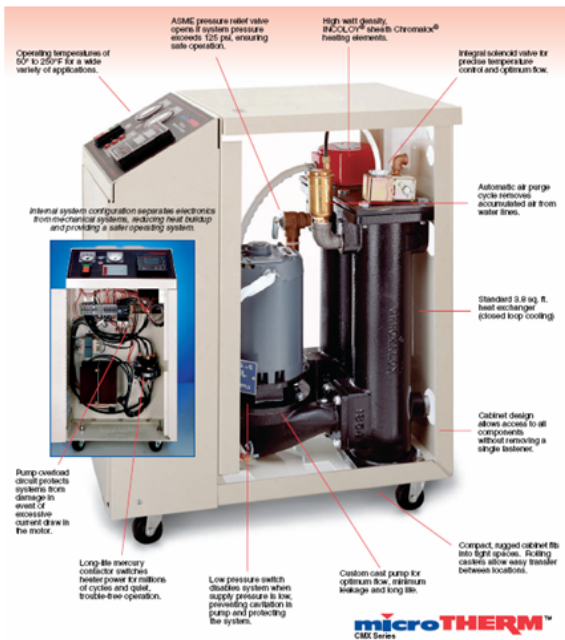
## Laboratory Cooling

For testing at Sunpower, we plan to use a commercial system to supply cooling (Fig. 26). These are commonly used for plastic injection molds but appear will work well for our use. These units first cool the incoming recirculated water (using a heat exchanger cooled via tap water) and then heat it to the desired outlet temperature.

## Charging Circuit

The charging system will be fairly typical for free-piston Stirling engine (FPSE) work and shown schematically in Figure 27.

- **Chromalox standard system**



- digital communications interface for remote PC/PLC control systems.
- rated at 50 to 250 degrees F and pressures up to 135 PSI.

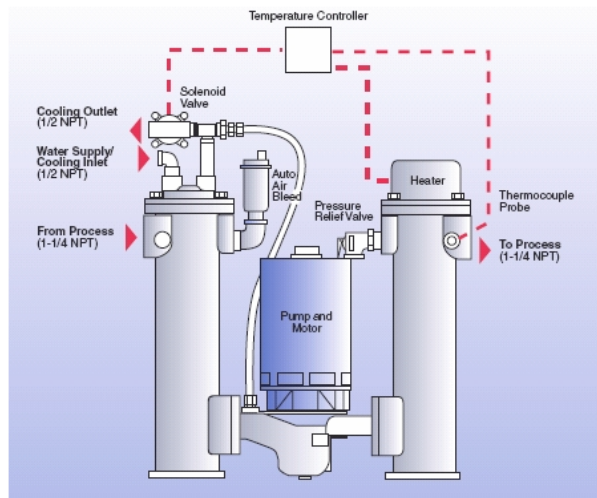


Figure 26.—Stock cooling system planned for use with FSP.

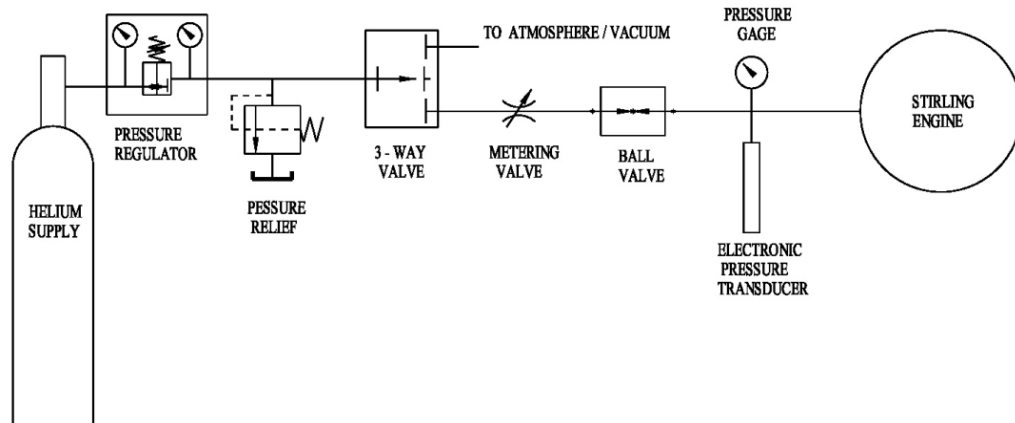


Figure 27.—Charging circuit.

## Mounting of Opposed Unit

We propose mounting the full assembled PCU in a manner which we have used in the past for various horizontal units (Figs. 28 and 29). This uses special flat planar springs which provide high vertical stiffness and at the same time quite low horizontal stiffness. The high vertical stiffness is needed to support the mass; the low horizontal forces allow for thermal expansions and do not transmit substantial horizontal forces to ground.

## Outer Heat Exchanger Flow Testing

To verify the external heat exchangers have the predicted flow fields, we plan to build flow test parts from aluminum and plastic parts as shown in Figure 30. This will allow flow visualization by using ink injection and viewing the flow through the outer plastic parts. Several internal pressure taps will also be used to measure flow at various locations.

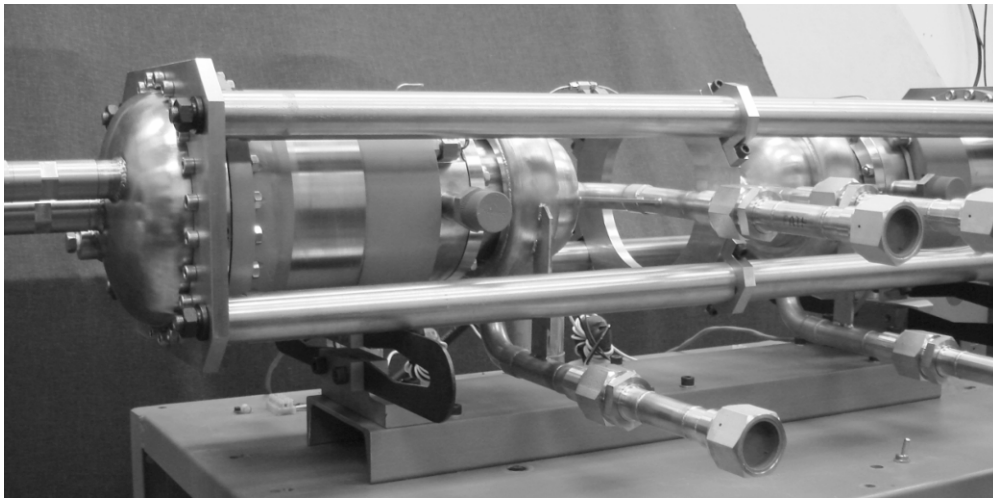


Figure 28.—Mounting of opposed 1 kW engines on flat planar springs.

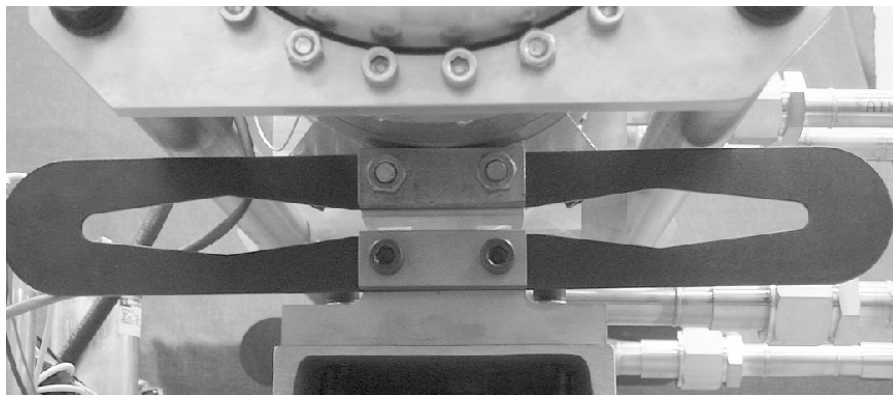


Figure 29.—Close-up of planar spring (two required).

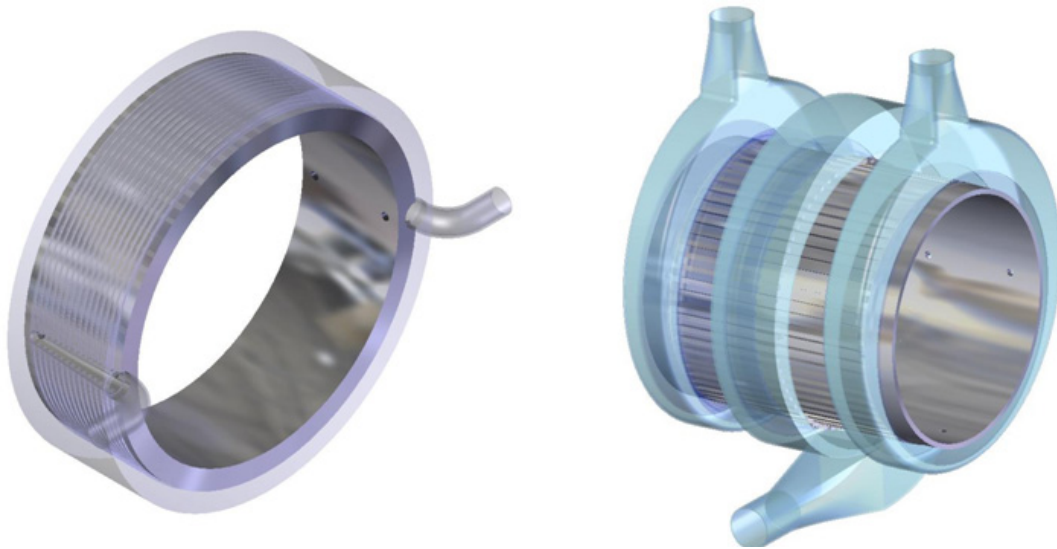


Figure 30.—Flow testing and visualization hardware for outside HXs.

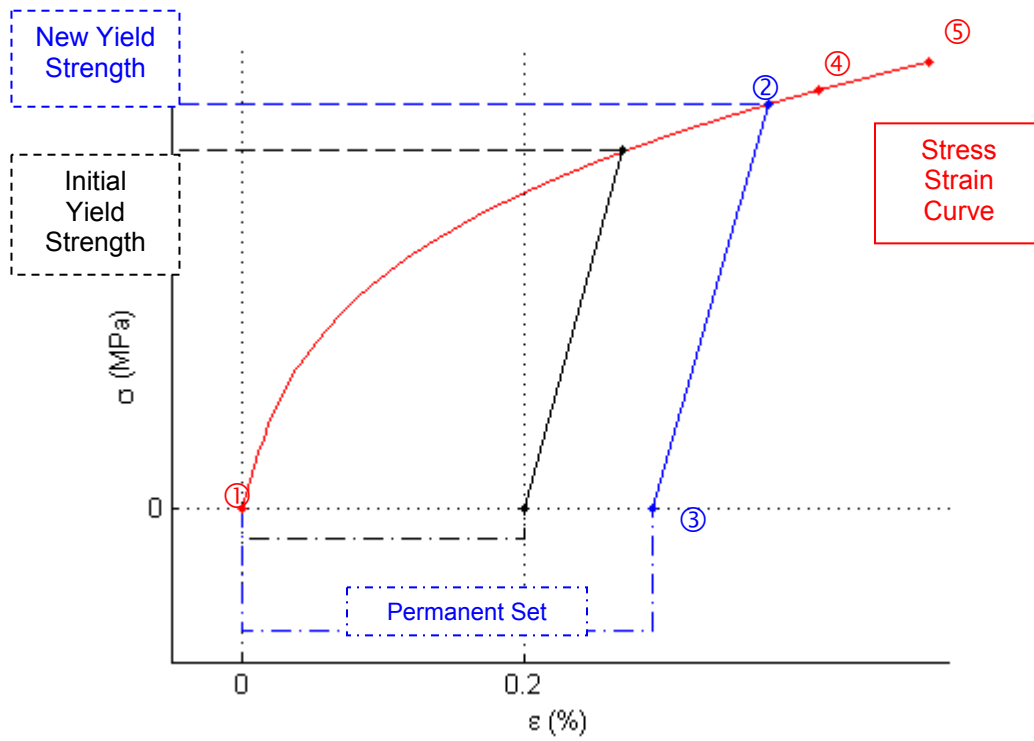


Figure 31.—Simple elastic plastic analysis.

## Heater Head Stress Analysis

Nonlinear elastic-plastic finite element analysis (FEA) was performed on the FSP heater head assembly to accurately model the stress state and relevant design margins (Fig. 31).

Elastic-plastic analysis is path dependent. That is, the final stress state depends on the loading history of the component. A simple exaggerated example is shown in Figure 31. Virgin material is loaded above the initial yield strength (point 2) and then unloaded. During loading, the material follows the stress strain curve from point 1 to point 2. Then, during unloading, the material follows a new elastic curve (parallel to the initial elastic curve) from point 2 to point 3. At point 3 the material exhibits a permanent set and will have work hardened such that its new yield strength is equal to the maximum applied loading; the material will also have accumulated residual stresses. If the material is loaded again it will follow the new elastic curve from point 3 to point 2 until the loading exceeds the new yield strength (point 2); it will then proceed to follow the stress strain curve again until a new yield strength is established (e.g., point 4) or the ultimate tensile strength is reached (point 5).

### Material Properties

Four materials were used in the FSP heater head model: 316 Stainless Steel, Inconel 625, Inconel 718, and Copper Alloy 101. A summary of the material property sources is included in Table 8.

TABLE 8.—MATERIAL PROPERTY SOURCES

Material	UNS Number	Material Property Source
Copper 101	C10100	AMAX OFHC Copper Technical Brochure
Stainless 316	S31600	2007 ASME Pressure Vessel Code Part D
Inconel 625	N06625	MMPDS-02
Inconel 718	N07718	MMPDS-02

It is important to note that material properties values, particularly material strengths, taken from the ASME Pressure Vessel Code and the Metallic Materials Properties Development and Standardization (MMPDS) are minimum values developed using statistical methods. Therefore, the material properties of the actual components will be better than the assumed values.

The material properties used in the FEA are included in Table 9 and Figures 32 through 34. The linear coefficient of thermal expansion (CTE) and thermal conductivity were input as temperature dependent curves; and the modulus of elasticity, yield strength, and ultimate tensile strength were selected at the average operating temperature, after a thermal analysis was performed.

TABLE 9.—MATERIAL PROPERTIES

	Copper 101	Stainless 316	Inconel 625	Inconel 718
UNS Number	C10100	S31600	N06625	N07718
Heat Treatment	Annealed	Annealed	Annealed	Precipitation hardened
Elastic Modulus	100.0 GPa	158.0 GPa	170.5 GPa	190.5 GPa
Poisson's Ratio	0.31	0.27	0.28	0.29
Yield Strength	34.5 MPa	117.0 MPa	285.0 MPa	975.0 MPa
Tensile Strength	220.0 MPa	450.0 MPa	703.0 MPa	1200 MPa
Thermal Conductivity	See Figure 32	See Figure 32	See Figure 32	See Figure 32
CTE	See Figure 33	See Figure 33	See Figure 33	See Figure 33
Stress Strain Curve	See Figure 34	See Figure 34	See Figure 34	See Figure 34

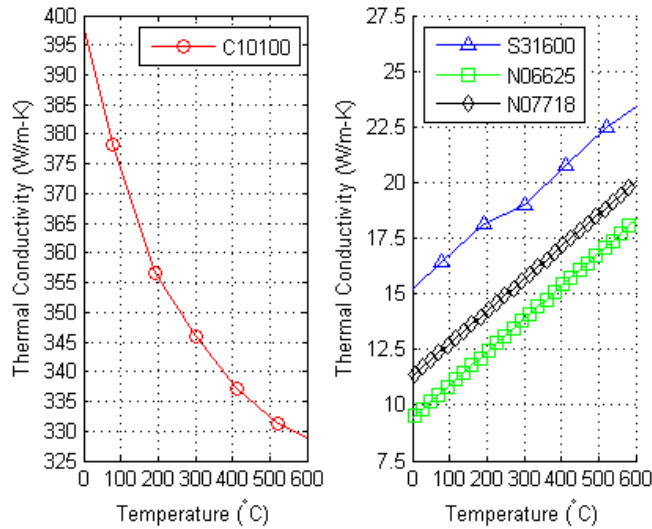


Figure 32.—Thermal conductivity.

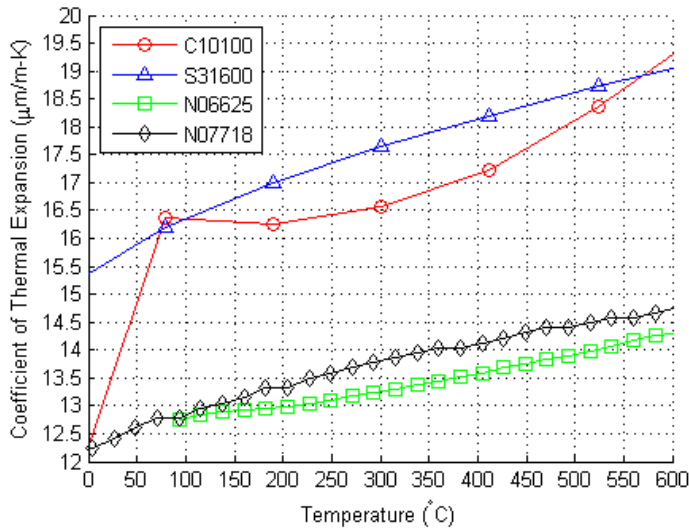


Figure 33.—Coefficient of thermal expansion.

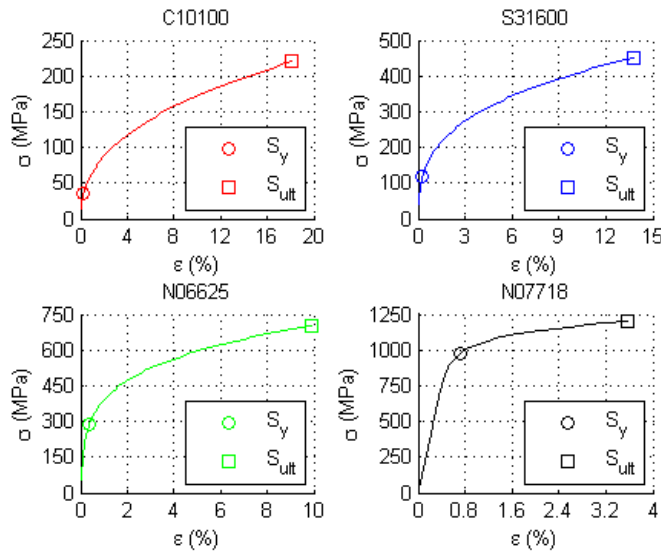


Figure 34.—Stress strain curves.

Ramberg-Osgood stress strain curves were generated based on the material yield and ultimate tensile strengths. The methodology for generating these curves is outlined in the ASM International publication, *Fatigue and Durability of Structural Metals* by Manson & Halford, 2006, Chapter 2, Page 39. The constitutive equations are given below.

$$\left(\frac{S_{ult}}{S_y}\right) = \frac{(500n)^n}{1+n}$$

$$K = \frac{S_y}{(0.002)^n}$$

$$\varepsilon = \left(\frac{\sigma}{E}\right) + \left(\frac{\sigma}{K}\right)^{\frac{1}{n}}$$

A summary of the parameters used to generate the Ramberg-Osgood stress strain curves is given Table 10.

TABLE 10.—RAMBERG-OSGOOD STRESS STRAIN CURVE PARAMETERS

	Copper 101	Stainless 316	Inconel 625	Inconel 718
Elastic Modulus	100.0 GPa	158.0 GPa	170.5 GPa	190.5 GPa
Yield Strength	34.5 MPa	117.0 MPa	285.0 MPa	975.0 MPa
Tensile Strength	220.0 MPa	450.0 MPa	703.0 MPa	1200 MPa
Strain Hardening Exponent (n)	0.4125	0.3201	0.2338	0.0772
Strength Coefficient (K)	448 MPa	855 MPa	1218 MPa	1575 MPa

### Finite Element Model

A simplified axisymmetric Finite Element Model (FEM) was used for the heater head analysis so that computation time could be reduced, while using a finer mesh for increased accuracy. The model consists of a 10.91° arc segment covering two of the 66 ribs in the heater head. The individual components and materials are shown in Figure 35.

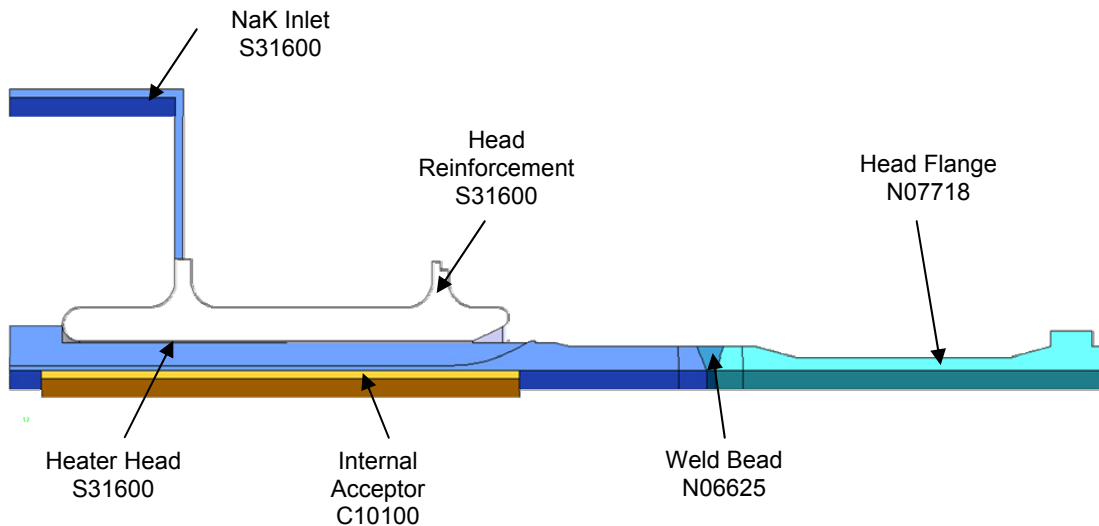


Figure 35.—Finite element model.

Modeling an axisymmetric heater head neglects two effects in the circumferential direction: the first is the eccentricity of the NaK manifolds, and the second is the circumferential temperature gradient imparted by the rejector. The eccentricity of the NaK manifolds can be ignored as they do not contribute appreciably to the strength or stiffness of the head assembly. Similarly, the circumferential temperature gradient can be ignored as it is an order of magnitude smaller than the axial temperature gradient. To further simplify the model, the NaK outlet manifold was omitted completely, and the internal acceptor was simplified to a 1.5 mm thick cylinder. The validity of these simplifications was confirmed with linear elastic FEA.

A more accurate representation of the interface between the Stainless 316 heater head and the Inconel 718 head flange was included in this FEM. The intermediate weld bead geometry is consistent with the use of an Inconel 625 filler material in a Stainless 316 to Inconel 718 weld. This geometry and approach were provided by Pratt & Whitney Rocketdyne as mentioned earlier in this report.

### Finite Element Mesh

A global mesh of 2.0 mm tetrahedral elements was selected for the entire model. The mesh consists of 34,691 elements and 57,859 nodes; 95.9 percent of the elements have an aspect ratio less than 3 and 0.0 percent have an aspect ratio greater than 10. This indicates that the mesh is well conditioned and will yield accurate results. The finite element mesh is shown in Figure 36.

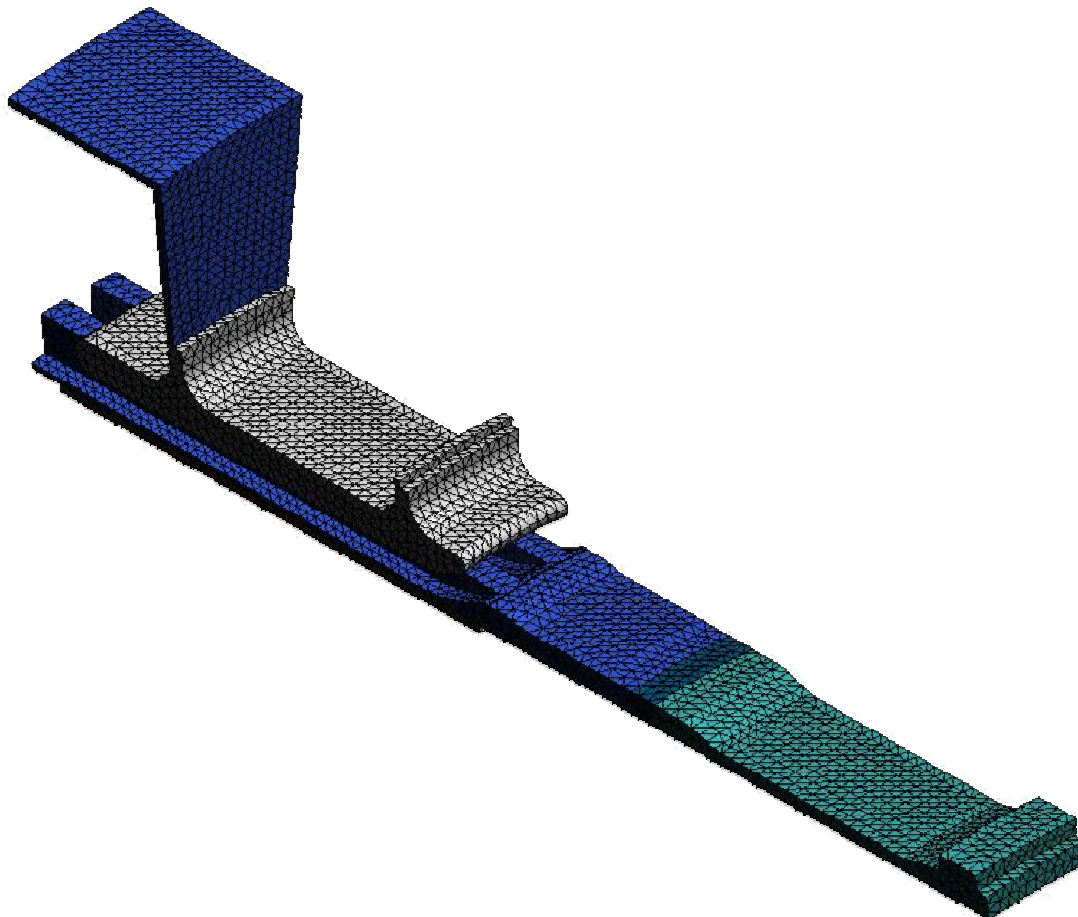


Figure 36.—Finite element mesh.

## Finite Element Analysis, Boundary Conditions and Contact Sets

Symmetry boundary conditions were used along the interface between the two convertor heater heads as well as along the edges of the arc segment. These symmetry boundary conditions are shown in Figure 37.

Two types of contact sets were used in this FEA, bonded contact sets and no penetration contact sets. Bonded contact sets behave linearly and can support tensile loads, compressive loads, and shear loads. No penetration contact sets behave nonlinearly. They can support compressive loads, but not tensile loads or shear loads. Simplified examples of bonded and no penetration contact sets are shown in Figure 38.

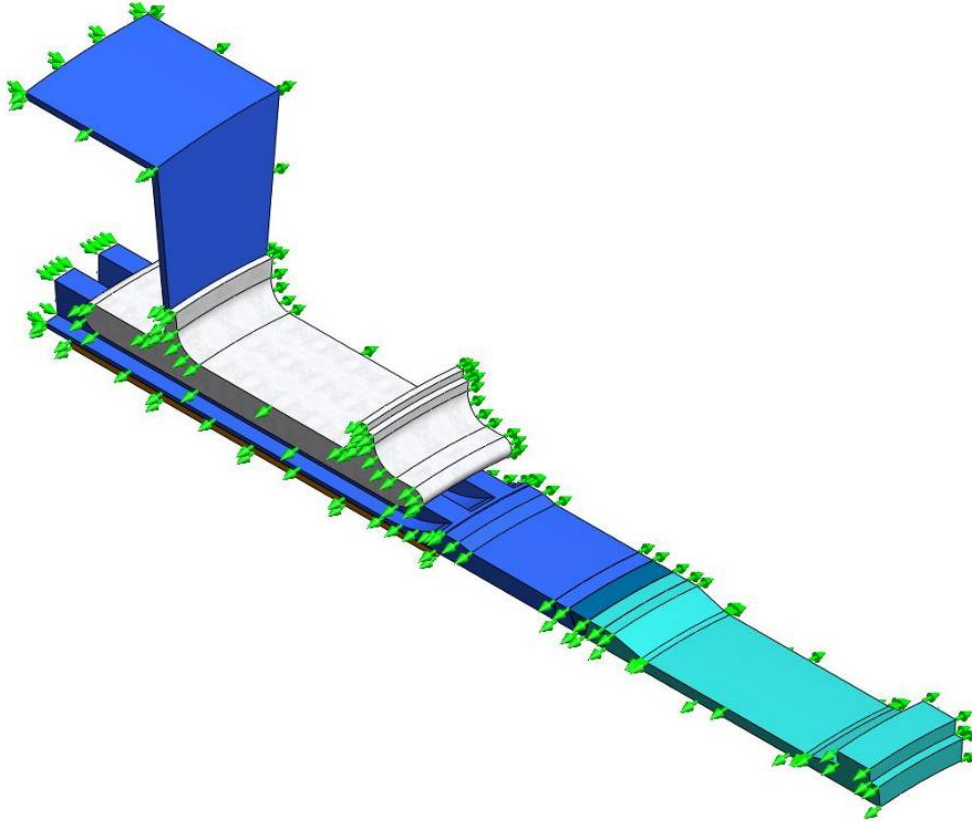


Figure 37.—Symmetry boundary conditions.

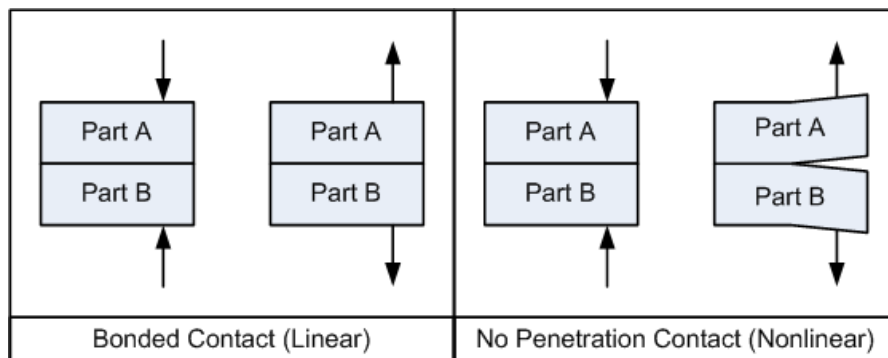


Figure 38.—Simplified contact sets.

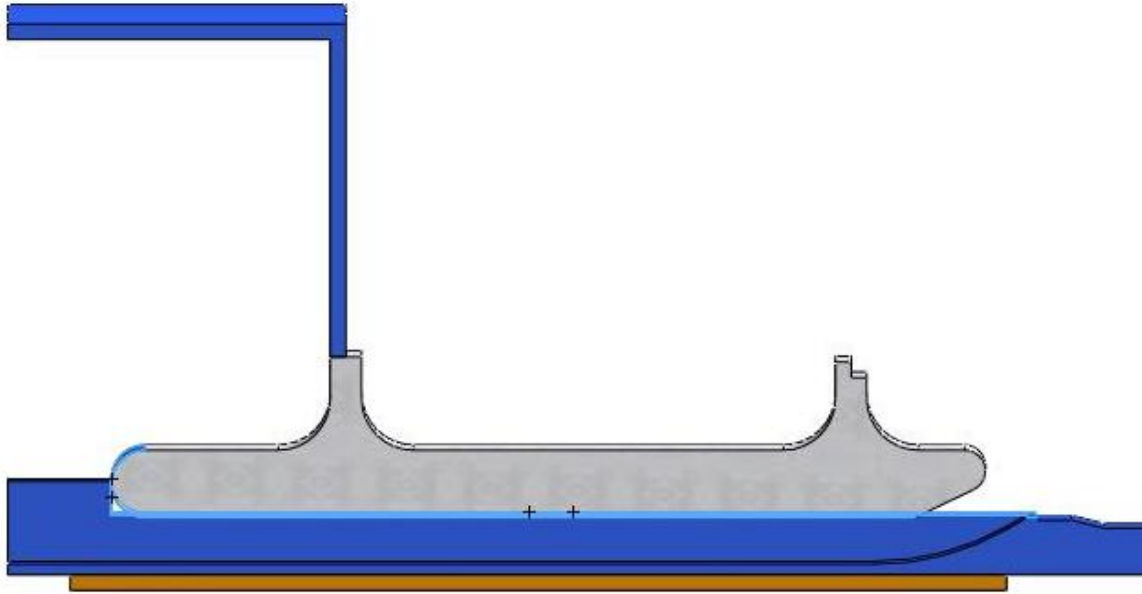


Figure 39.—No penetration contact sets.

For the head assembly FEA, all mating surfaces of components were assumed to be bonded except the interfaces between the heater head and the head reinforcement. These no penetration, contact sets are shown in Figure 39.

### Finite Element Analysis, Loads

The mechanical loading was simplified for the heater head FEA. Rather than including the entire internal acceptor, which would greatly complicate the model, the pressure acting on the inner diameter of the simplified internal acceptor was adjusted. Assuming the internal acceptor does not yield and does not contribute appreciably to the strength or rigidity of the heater head assembly, the internal acceptor can be replaced with an equivalent pressure, determined using the equation below.

$$P_{acc} = P_{tot} \frac{r_{i,acceptor}}{r_{i,head}}$$

Similarly, assuming that the transition does not impose significant bending loads on the heater head, the transition interface can be replaced with an equivalent hydrostatic pressure, determined using the equation below. The validity of these simplifications was confirmed with linear elastic FEA.

$$P_{HD} = P_{tot} \frac{\pi \cdot r_{i,head}^2}{\pi(r_{o,head}^2 - r_{i,head}^2)}$$

The thermal loading was also simplified for the heater head FEA. Three axial temperatures were input to establish the proper temperature gradient along the heater head. Detailed heat fluxes were omitted as they did not contribute significantly to the overall stress state. A summary of the mechanical and temperature loads is given in Table 11, Figure 40 and 41.

TABLE 11.—MECHANICAL AND THERMAL LOADS

Name	Description	Value
$P_{tot}$	Total pressure load*	6.826 MPa
$P_{acc}$	Equivalent acceptor pressure load	4.128 MPa
$P_{HD}$	Equivalent hydrostatic end load	77.97 MPa
$T_{hot}$	Hot end temperature	570 °C
$T_{acc}$	Acceptor end temperature	540 °C
$T_{cold}$	Cold end temperature	110 °C

\*The total pressure load consists of the mean pressure plus the work space pressure swing

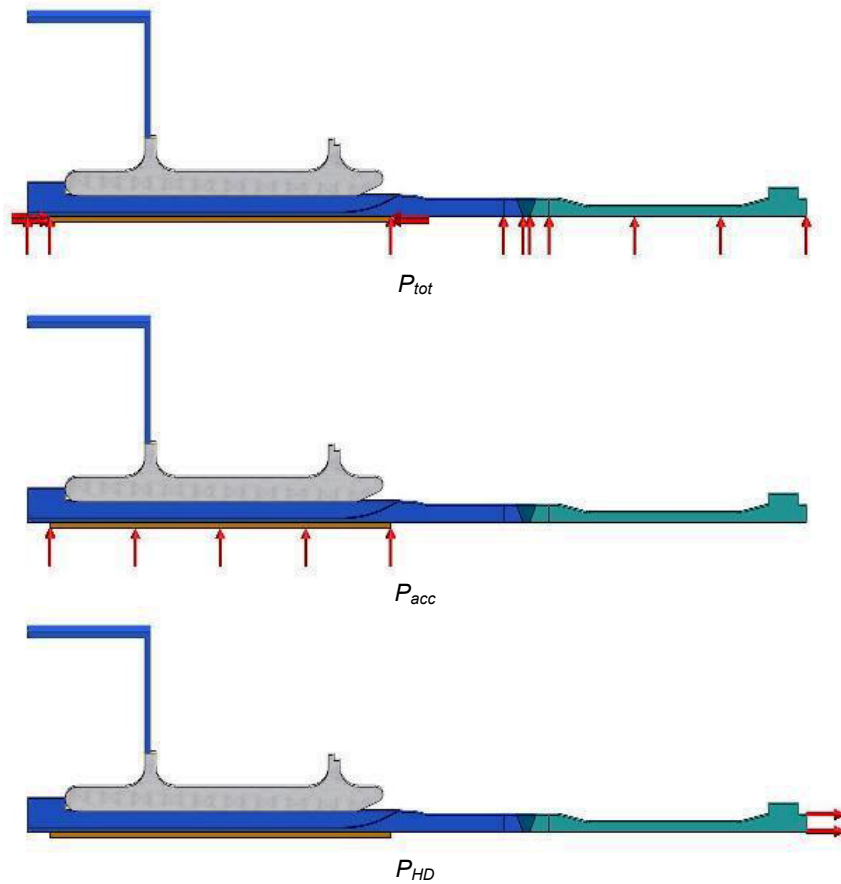


Figure 40.—Mechanical loads.

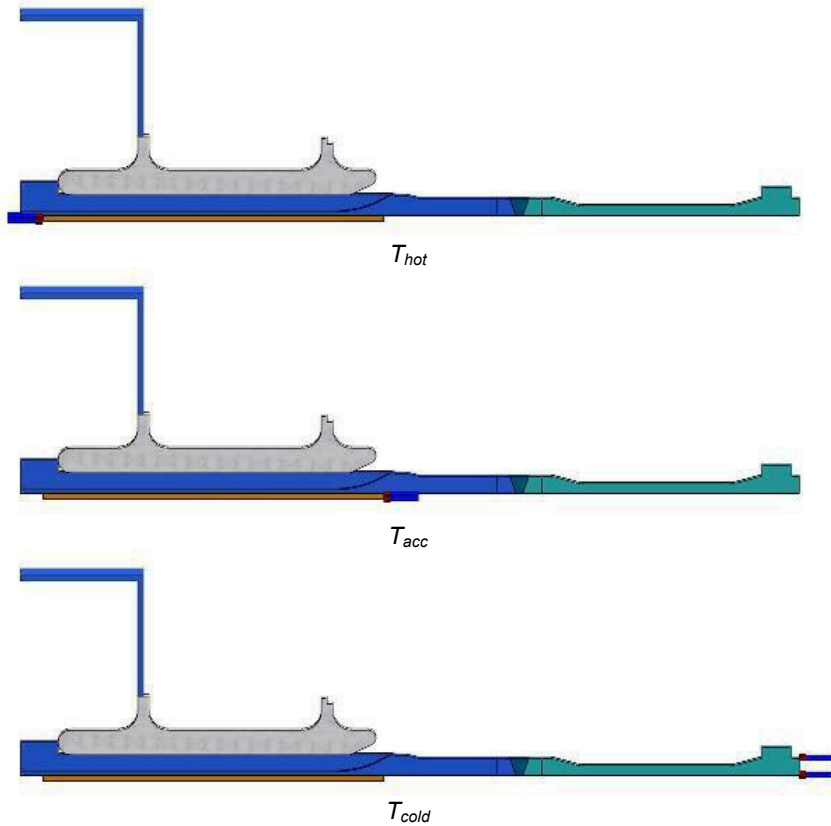


Figure 41.—Thermal Loads

Because elastic-plastic analysis is path dependent, it was necessary to create a realistic loading history for the assembly. Assuming that no appreciable residual stresses exist in the components after fabrication, the first significant load the hardware will encounter will be during the proof pressure test where the hardware is taken to 1.5 times operating pressure. The next significant load the hardware will encounter will be during testing where the convertor is brought up to operating pressure and operating temperatures. Assuming the convertor does not significantly exceed operating temperatures and pressure, no additional yielding loading needs to be considered.

The loading history was applied in the FEA using “pseudo time” curves for the loading factor. The “pseudo time” variable allows the user to create a path dependent load history, but should not be confused with actual time steps associated with time varying dynamic loading. For example, during the first pseudo time interval, from 0.000 to 0.125 s, the internal pressure transitions from atmospheric pressure to proof pressure. The pseudo time variable ensures that this is the first operation in the FEA. However, in reality it would take much more than 0.125 s to ramp up to this pressure.

A summary of the heater head loading history is given in Table 12 and shown graphically in Figure 42.

TABLE 12.—LOADING HISTORY

	Pseudo Time Interval	Pressure Loading	Temperature Loading
1	0.000 to 0.125	Ramp up to proof pressure	Hold at room temperature
2	0.125 to 0.250	Hold at proof pressure	Hold at room temperature
3	0.250 to 0.375	Ramp down from proof pressure	Hold at room temperature
4	0.375 to 0.500	Hold at atmospheric pressure	Hold at room temperature
5	0.500 to 0.625	Ramp up to operating pressure	Ramp up to operating temperatures
6	0.625 to 0.750	Hold at operating pressure	Hold at operating temperatures
7	0.750 to 0.875	Ramp down from operating pressure	Ramp down from operating temperatures
8	0.875 to 1.000	Hold at operating pressure	Hold at room temperature

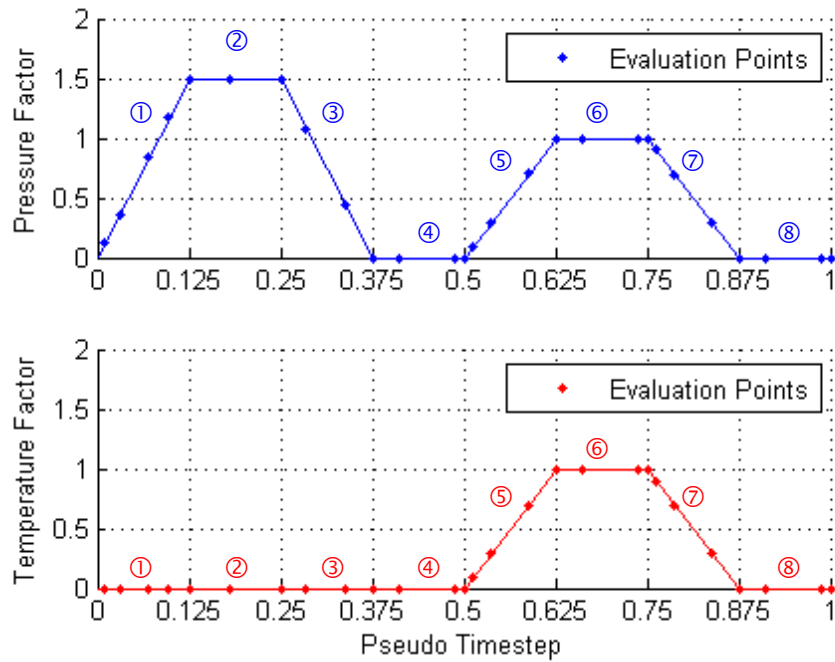


Figure 42.—Loading history.

### Finite Element Analysis, Results

Results of the FEA are presented at the pseudo time steps presented in Table 13.

TABLE 13.—SELECTED FEA RESULTS

Pseudo Time	Description	Figure
0.250	During proof pressure test	Figure 43
0.500	After proof pressure test	Figure 44
0.750	During operation	Figure 45
1.000	After operation	Figure 46

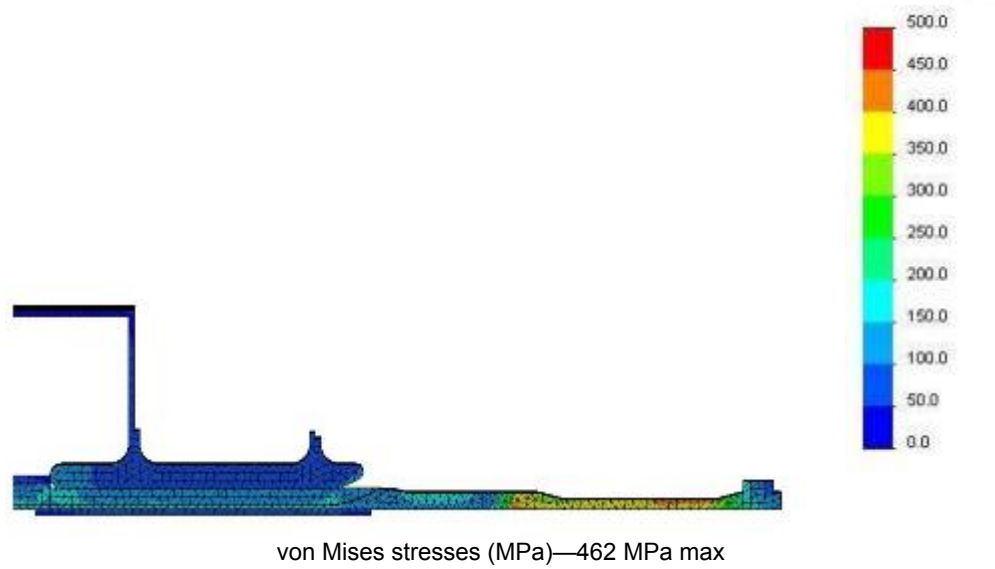
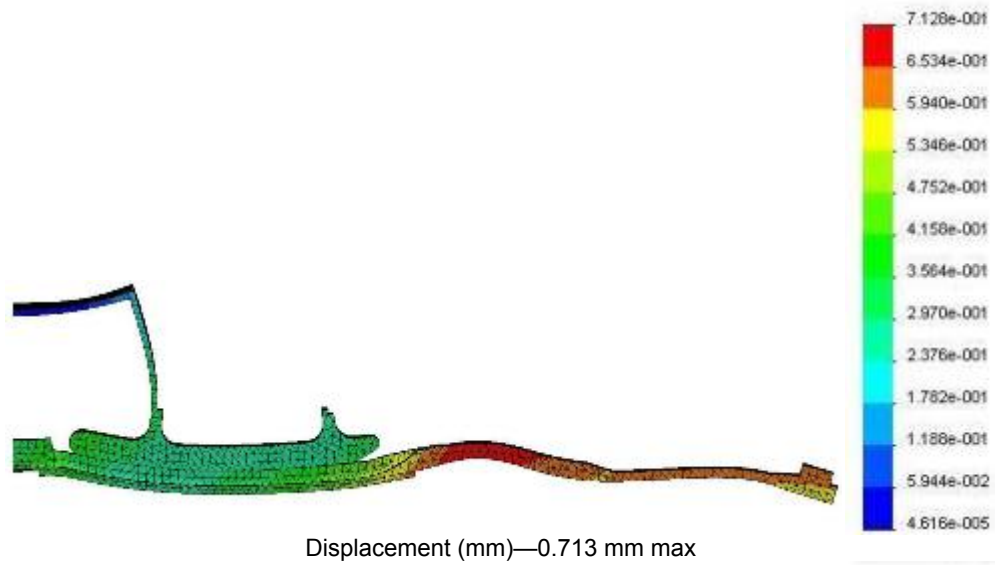


Figure 43.—During proof pressure test (0.250).

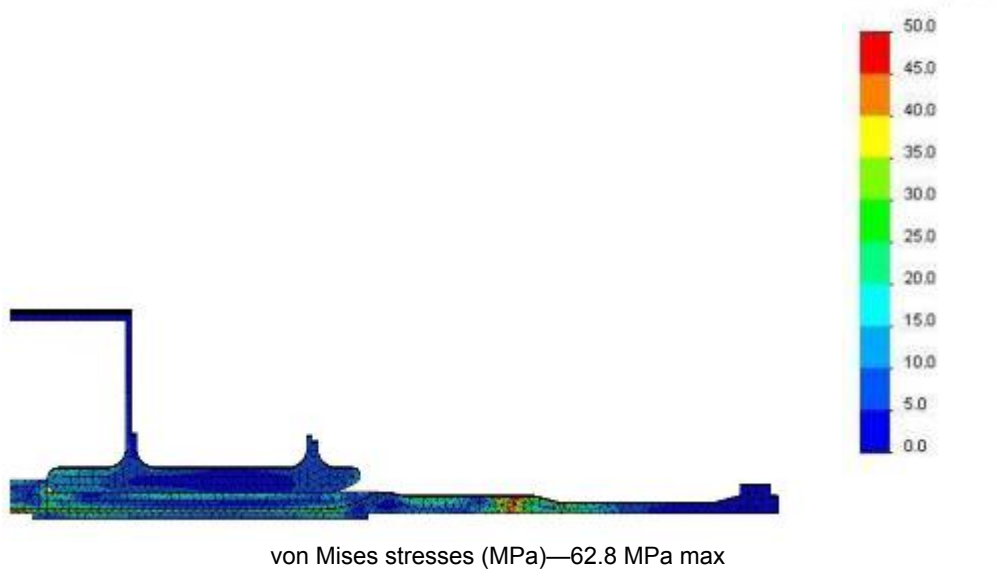
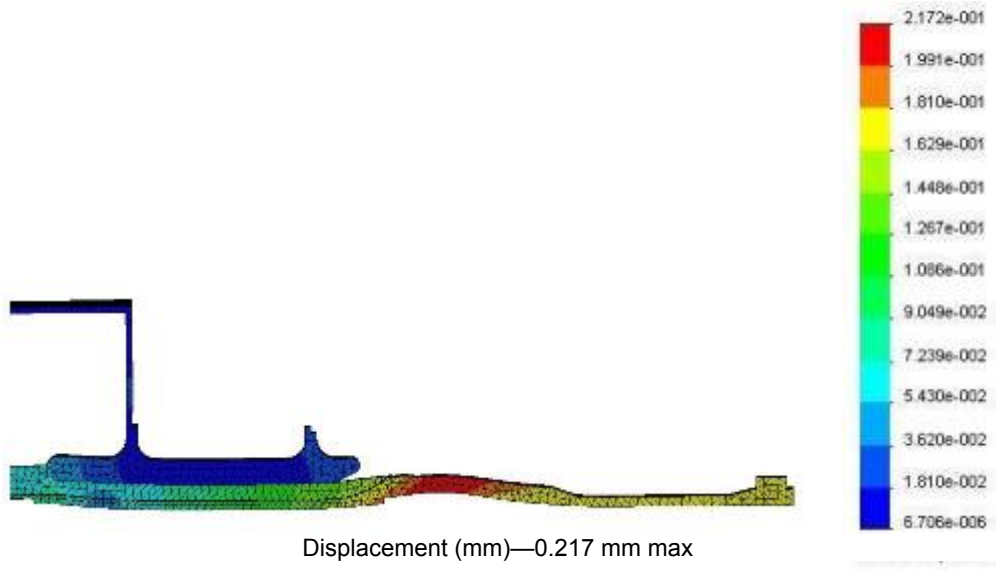


Figure 44.—After proof pressure test (0.500).

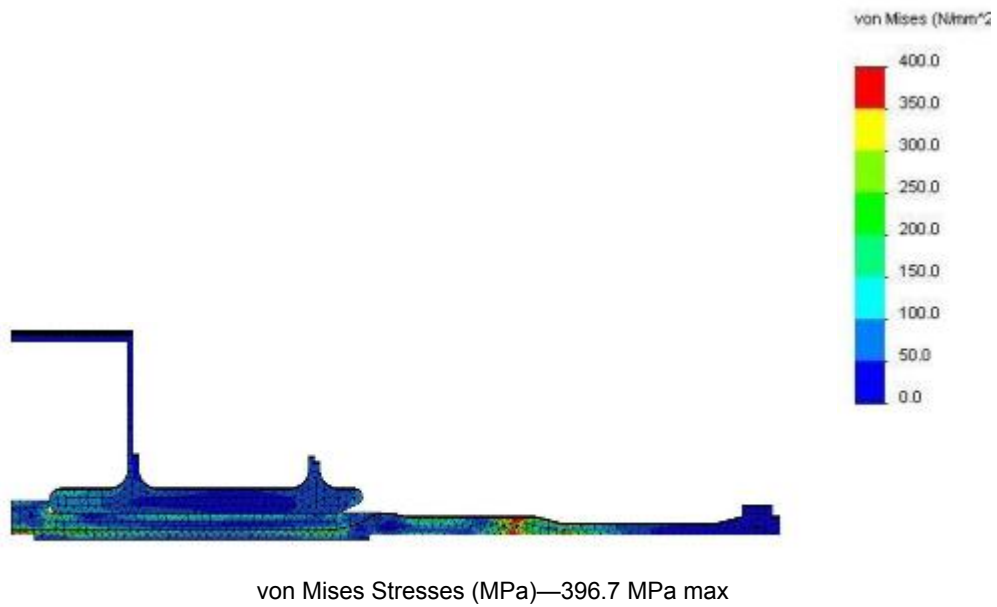
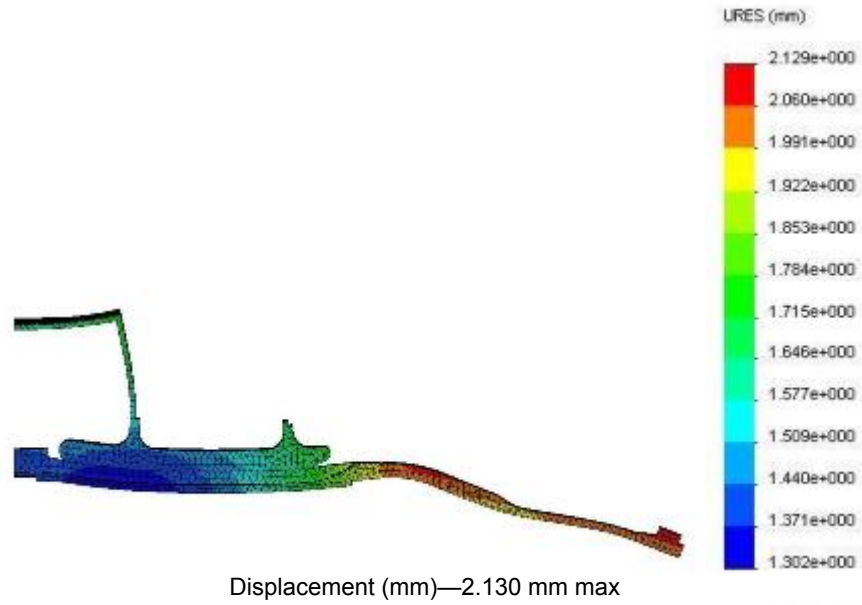


Figure 45.—During operation (0.750).

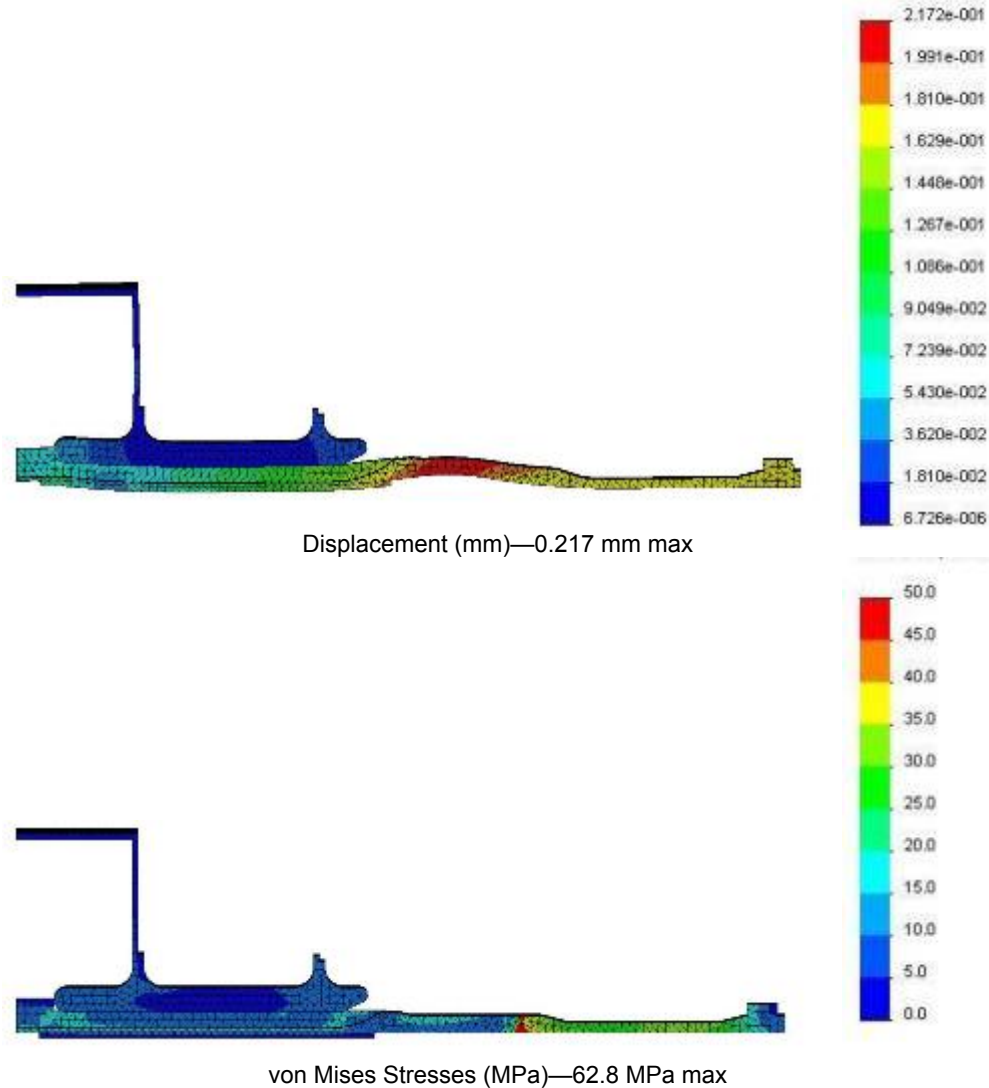


Figure 46.—After operation (1.000).

### Conclusions

The Fission Surface Power heater head design meets the requirements specified by GRC. While significant secondary bending stresses are developed due to the axial temperature gradient and pressure loading, these stresses self-relieve through plastic deformation. The majority of this plastic deformation occurs in the Stainless Steel heater head wall between the ribbed NaK heat exchanger and the Inconel 625 weld joint. In this region, Sunpower anticipates a permanent set of  $\sim 0.200$  mm in the radial direction. This should not affect fit, form, or function, as the transition wall extends from the rejector to the acceptor. In the yielded regions of the stainless steel, residual compressive surface stresses are present. These are roughly 25 MPa von Mises, at room temperature and atmospheric pressure. Residual compressive surface stresses are also present in the higher strength Inconel 625 and Inconel 718 components. These are roughly 62.8 MPa von Mises, at room temperature and atmospheric pressure. Overall the permanent plastic set and residual stresses are relatively minor. The plastic set is  $\sim 0.095$  percent of the overall diameter and the residual stresses are on the same level as those that might be imparted through material treatments such as, forging, cold rolling, or shot-peening. The as-delivered stress state is shown in Figure 47.

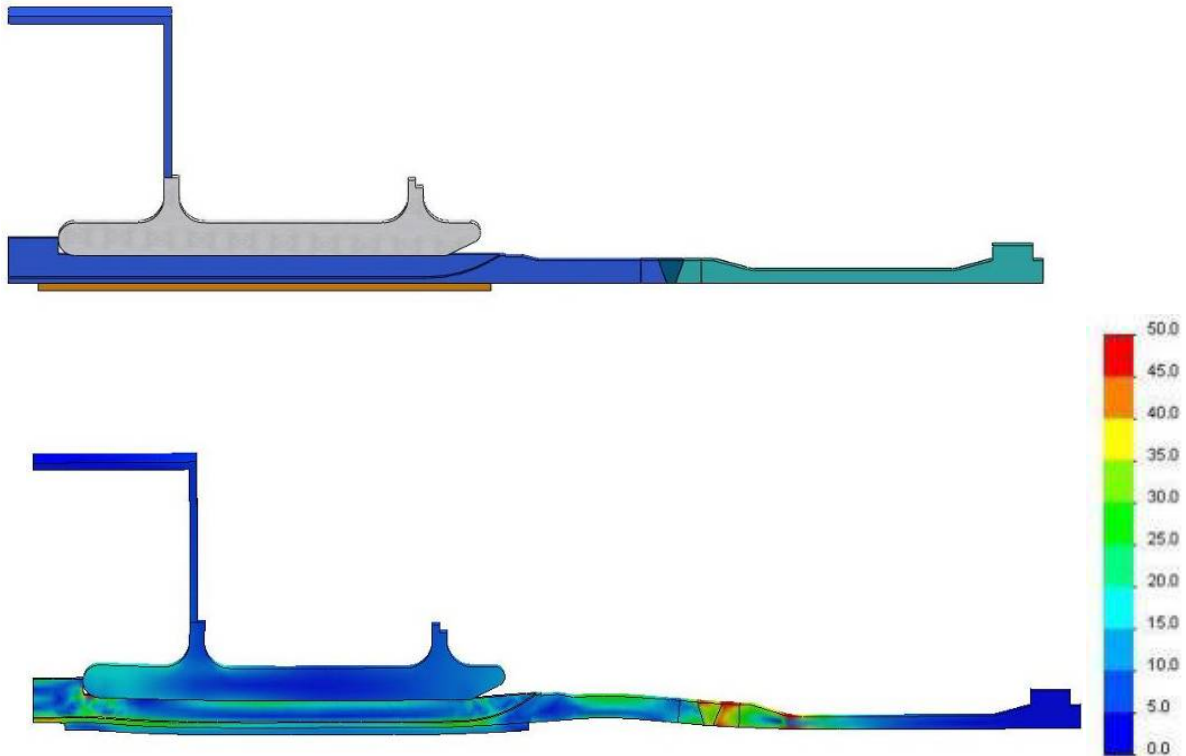


Figure 47.—As delivered stress state.

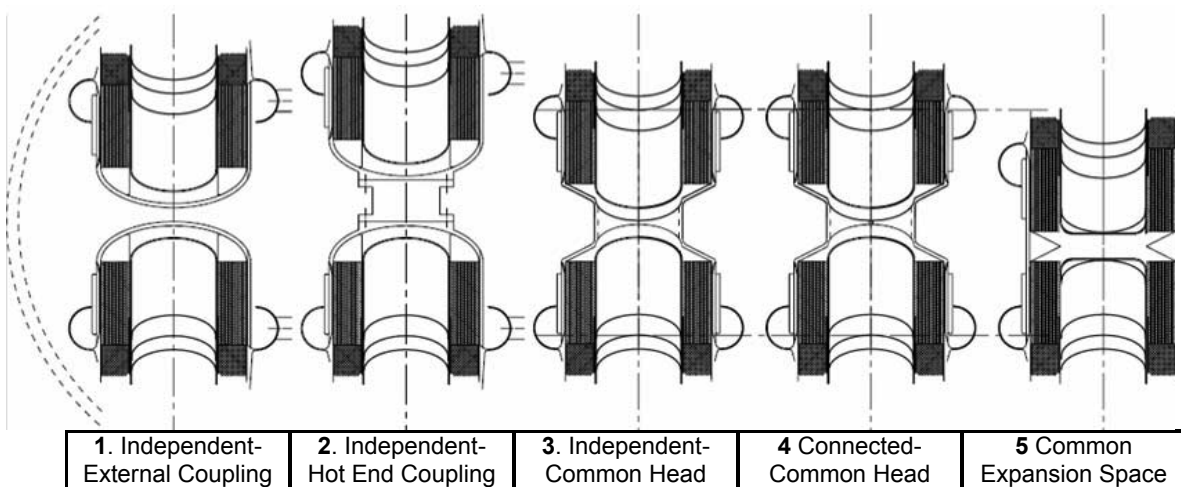


Figure 48.—Different converter couplings considered for FSP.

### Engine Coupling Study

For the opposed converter, a decision needed to be made as to how the machines would be mechanically coupled. To complete this task, we utilized our group of consultants with many years combined experience in Stirling machines.

Figure 48 presents the five different coupling techniques identified and considered.

Note that Concept 4 has a small hole in the center which communicates and equalizes the mean pressure of the two machines. Also, note that Concept 1 requires an external structure to mechanically connect the machines (shown by the dashed lines).

The advantages and disadvantages of the different techniques are summarized in Table 14.

TABLE 14.—ADVANTAGES AND DISADVANTAGES OF DIFFERENT COUPLING CONCEPTS

	1. Independent-External Coupling	2. Independent-Hot End Coupling	3 Independent-Common Head	4. Connected-Common Head	5. Common Expansion Space
Advantages	Single unit operation and replacement	Single unit operation and replacement, Low dome stress	Single unit operation, LM manifold exists, Low dome stress	Possible single unit operation, LM manifold exists, Low dome stress	Short length, Low cost, No dome stress, Lowest vibration due to stiff structure
Disadvantages	Poor stiffness,	Requires anti-seize mounting,	No single unit replacement,	No single unit replacement (possible operation)	No single unit operation or replacement
Comment	Single operation requires dynamic abs	Single operation requires dynamic abs	Single operation requires dynamic abs	Single operation requires dynamic abs	

The first two concepts are completely separate machines and, thus, a single unit could be replaced if so desired. In the case of Concepts 1 to 3, a single unit could be operated should the other fail, provided a dynamic absorber is included in the system. Note however that such an absorber would be rather large and heavy. Concept 4 might allow single unit operation, provided the failure was not a leak that discharged gas from both engines.

During the study, we realized that Concept 5 will result in the least transmitted vibration from the system. It is well known that in Concept 1, while on the whole being dynamically balanced, that some vibration of each half occurs due to flexibility of the coupling. Concepts 2 to 5 are much more ridged but one can still expect some vibration of individual units due to flexibility of the dome at the coupling point. This leads one to the realization that Concept 5 is the most rigid of all connections, and will result in the least force transmitted to attachments such as plumbing.

Concept 5 also is the most compact arrangement with the simplest heater head design. This concept does require some consideration to the displacer design, as is discussed earlier in this report.

Based on the above the decision was made to use Concept 5 with the common expansion space.

## Selection of Mechanical Layout, Displacer Drive, and Springing

An early design trade was to select the basic layout for the FSP dynamic components and displacer drive. The goal here was to study the various options and select the best arrangement for a modern, efficient, high power machine. The SPRE and CTPC space engines, built by Mechanical Technology, Inc. (MTI), had incorporated a “virtual rod” displacer drive with a displacer gas spring; whereas all Sunpower’s modern machines of lower power output had evolved to a mechanically sprung “rod-through-piston” displacer drive. Here, the large accumulated experience of Sunpower and the consultants on the project was utilized to make the selection of the drive arrangement for the FSP.

In this trade, we found it useful to review the evolution of FPSE machines, to understand the reasons why the various concepts were selected, the observed problems and virtues, and to then rate these objectively. In the trade that is detailed in the following, we have omitted the earliest form of the FPSE, the overdriven non-resonant displacer, often termed the “bang-bang” displacer drive. While this was the earliest form of a working FPSE, it was deemed not applicable to a modern long life machine. Note that the area of the displacer rod determines its drive force. The first working machines thus had very large rod diameters which guaranteed the motion of the displacer.

The first resonant displacer design of FPSE evolved from the earlier over-driven displacer concept, where the displacer energy is transferred into the piston. A relative (displacer-to-piston) displacer gas spring was incorporated inside the piston, and is shown in Figure 49 as the first concept in the upper right hand side of the figure. Working machines were built with this concept in the early 1970s. However, the displacer gas spring within the piston was often found to have significant gas hysteresis losses. It was

soon realized that displacer sprung-to-ground (or the housing) required about half the spring rate and this would reduce losses significantly.

Thus, the next evolution was to extend the displacer rod through the piston and to provide a displacer gas spring to ground, as shown in the lower right of Figure 49. This configuration was tried briefly in the mid-1970s but was plagued by alignment problems and rubbing of components. Because of alignment problems, an attempt was made to split the rod below the piston and to add compliance between the parts of the rod.

In light of the earlier problems, in about 1976, the “posted rod” arrangement was devised and implemented (shown at the bottom of Figure 49). This solved the earlier alignment problems and was used on several successful machines including the RE-1000 which was extensively tested at NASA Lewis (now NASA GRC). This design was successful because it decoupled the alignment issues of the displacer and the piston.

The posted rod however did introduce assembly difficulties as the piston cylinder and spider now had to be removed in order to remove the displacer. This arrangement also introduced dead volume in the working space because of the spider that supports the displacer rod. To reduce volume, the nose of the piston included extensions that would pass through the openings in the displacer spider, but this of course required that the piston not be allowed to rotate during operation.

The next arrangement shown in the lower left is the virtual rod. This was originally devised by Sunpower and shared with MTI during the years of collaboration in the late 1970s. The concept here is that the displacer drive area, formally provided by the central rod, is now accomplished by a step in diameter on the outer diameter of the displacer.

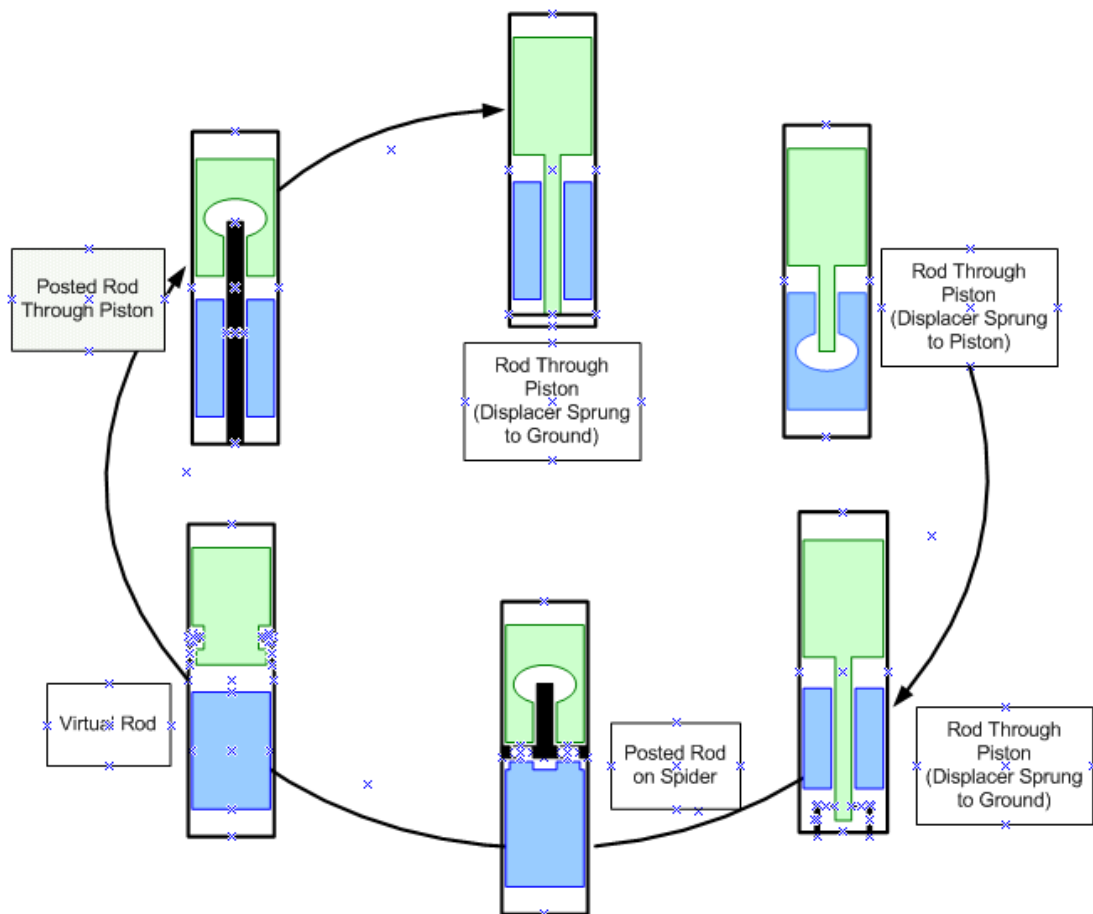


Figure 49.—Different layouts of beta-type FPSEs.

This had the *posted-rod* advantage of independent displacer and piston running surfaces and also eliminated the dead volume in the compression space. The problem with this arrangement is that it introduces significant seal losses because the formerly low differential pressure body seal on the displacer outside diameter is now replaced by two seals having a much higher differential pressure. The expansion and compression spaces of the Stirling engine differ in pressure only by the pumping losses in the heat exchangers. The virtual rod instead requires sealing between each individual working space and a different pressure gas spring.

The above schematic is misleading in its simplicity as the actual implementation of the virtual rod is rather complicated. This is better illustrated by Figure 50 showing how the virtual rod would be implemented into the FSP in a similar way as it was implemented in the SPRE and CTPC designs.

As seen, the implementation is rather complicated and makes assembly of the machine quite difficult. Another drawback of the arrangement implemented by MTI was that the reduced compression space volume was not achieved. The connection from the rejector to the compression space turned out rather long and added volume. Also the connection is believed to have introduced additional losses in the form of gas pumping and hysteresis losses within the connecting duct.

An advantage of the virtual rod is that it provides a very ridged gas bearing support for the displacer. This results from the very large diameter gas bearings.

Sunpower also built several machines after the rod posted to spider where the rod was anchored in the bounce space and passed through the piston as shown in the upper left of Figure 49.

Sunpower machines (both engines and cryocoolers) then evolved into a design much like the first displacer sprung to ground machines. However, the gas spring was replaced by a planar mechanical spring. In order to avoid the earlier alignment difficulties, a flexible link was used to connect the displacer to the spring. Thus, the alignment of the spring was not critical. This concept is shown at the top of Figure 49; only the flexible coupling to the spring is not shown.

As a summary, Table 15 lists the different types of displacer arrangements together with the identified advantages and disadvantages.

As part of the study, consideration was also given to the type of displacer spring. Basically, three options exist: 1) single-sided gas spring 2) dual gas springs created with a “puck” added to the end of the displacer rod, and 3) mechanical.

The first three engine concepts and the fifth shown in schematic form in Figure 49 illustrate single sided gas springs. Here, the rod area is simply used as the piston for the gas spring. The Figure 51 illustrates the dual gas spring where the puck is added to the end of the displacer rod and a mechanical planar spring.

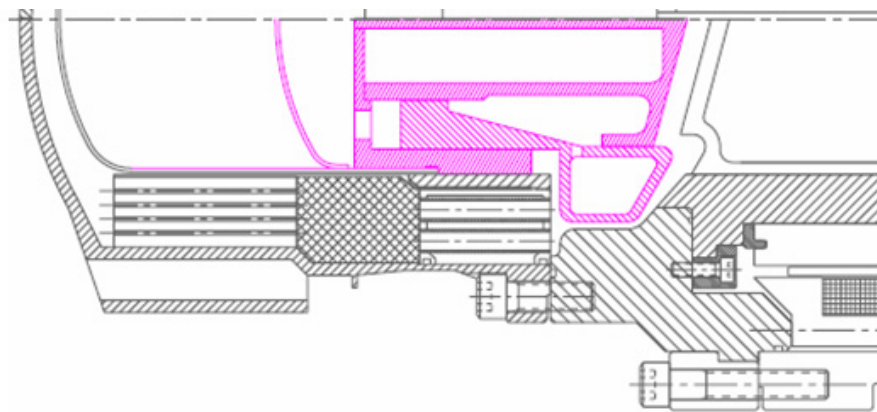


Figure 50.—Virtual rod arrangement with dual displacer gas springs.

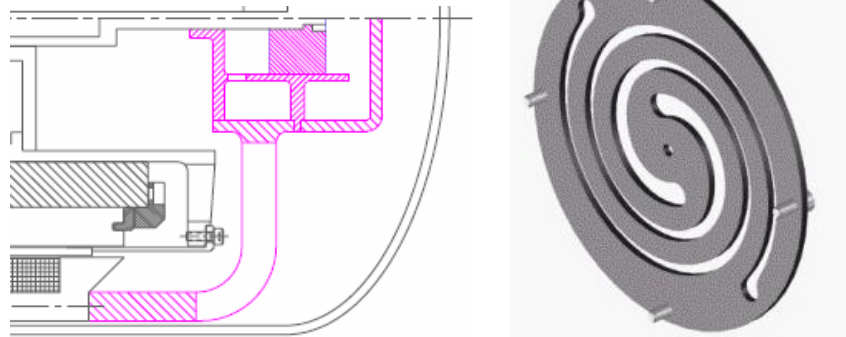


Figure 51.—Displacer gas spring utilizing a puck and alternate mechanical spring.

TABLE 15.—ADVANTAGES AND DISADVANTAGES OF BASIC FPSE LAYOUTS

Arrangement	Advantages	Disadvantages
Displacer Sprung to Piston	Low dead volume Ease of Assembly	Large spring constant introduces losses Spring must fit within piston
Rod through Piston Sprung to Ground	Low dead volume	Difficult alignment
Posted Rod on Spider	Decoupled displacer and piston running surfaces	Added complexity Difficult assembly Added volume Spring must fit within displacer
Virtual (or Annular) Rod	Decoupled displacer and piston running surfaces	Added complexity and more difficult seals Difficult assembly Added volume and losses Spring must fit within displacer
Rod through Piston fixed in Bounce Space	Low dead volume	Difficult alignment Spring must fit within displacer
Rod through Piston Mechanically Sprung to Ground	Low dead volume Low spring losses Spring need not fit in displacer or piston Ease of Assembly	

Table 16 summarizes the trade-offs between the types of springs:

TABLE 16.—ADVANTAGES AND DISADVANTAGES OF TYPES OF DISPLACER SPRINGS

Type	Advantages	Disadvantages	Other
Single-Sided Gas	Mechanical simplicity Ease of assembly	Limited spring constant High losses	Generally limited to low frequency and/or high pressure machines Requires gas centerports
Dual Gas with Puck	Increased spring constant Reduced losses	Mechanical complication Difficult assembly	Require centering gas ports
Planar Mechanical	Low losses Provide mean running position centering	Spring constant does not change with mean pressure Difficult to implement within moving component	Spring constant changes slightly with temperature Often used in stacks to reduce stresses
Coil Mechanical	Low losses Provide mean running position centering	Spring constant does not change with mean pressure Are generally long Required use of pairs of compression springs Introduce side loads	To avoid pairs of springs or side loads a spring machined from tube resulting in a square wire spring is possible

As stated in Table 16, single gas springs are generally limited to low frequency ( $\sim < 30$  Hz.) and/or high pressure engines. We have also included mechanical coil springs in Table 16, although they have found no use in modern machines because of their listed disadvantages. Coil springs machined from tube can avoid some of the problems of common compression springs, but still are rather long and have not been used in any known machines. In the final decision, we selected a planar mechanical spring.

As part of the study of displacer drives and springing, we created representative layouts of how the concepts would be implemented in a full size 6 kW convertor. The virtual rod and rod through piston with a mechanical spring have been shown in earlier figures. Figures 52 and 53 show how the posted displacer with spider, and the posted displacer with the rod fixed in the bounce spacer would be implemented. Note that these are shown in an earlier layout of the convertor although the size is representative of the final design.

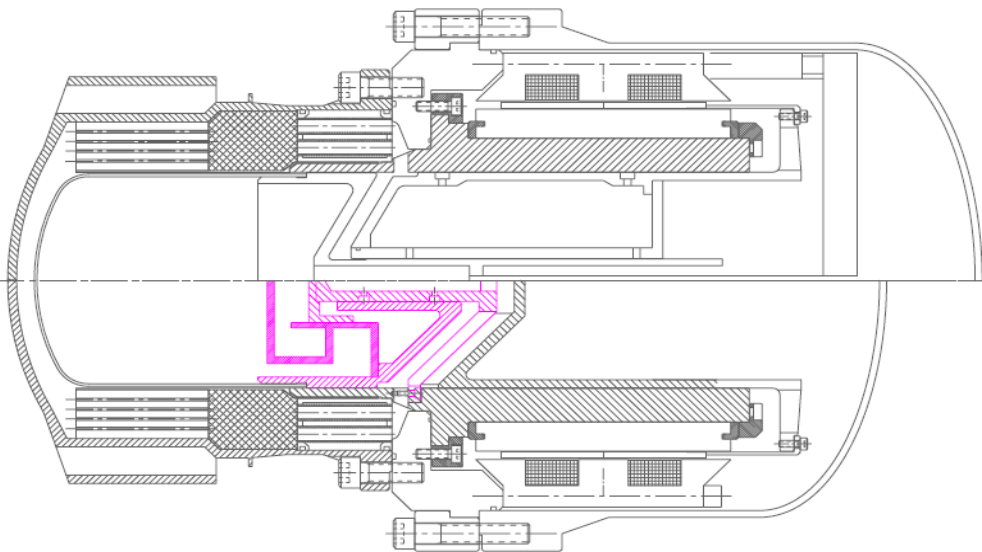


Figure 52.—Posted displacer with spider (and gas spring puck).

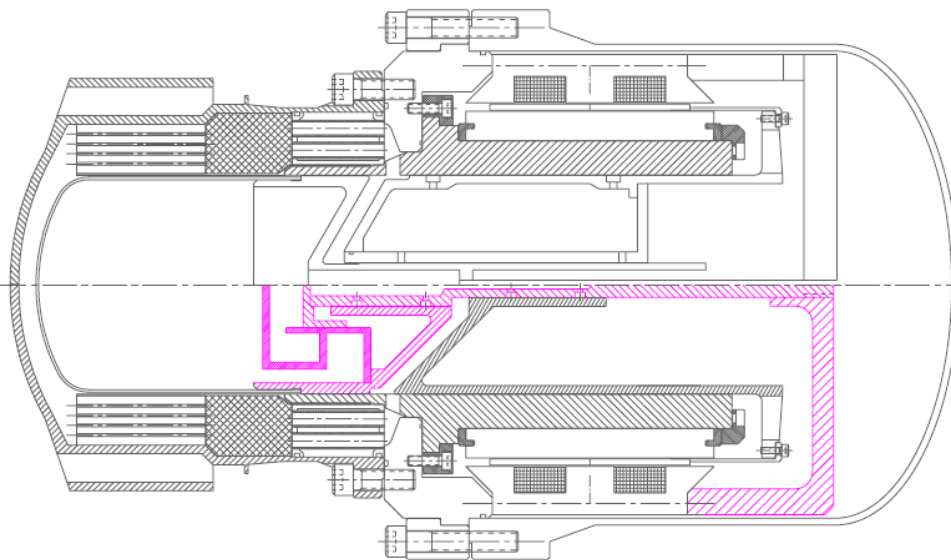


Figure 53.—Posted displacer rod fixed in bounce space (and gas spring puck).

## Off Design Projected Performance

This section presents the performance at off-design conditions. Figure 54 shows predicted performance as a function of piston amplitude.

Figures 55 and 56 show efficiency increases at lower power output. The increasing efficiency at reduced powers is typical of Stirling machines. For simple monolithic head machines, this is easily explained since as the power is reduced, the through-wall temperature drops decrease resulting in better cycle performance at lower powers. This is also the characteristic of our P2A engine. However, this is less obvious for machines with more complicated heater heads such as the Mod-2 and the SPRE.

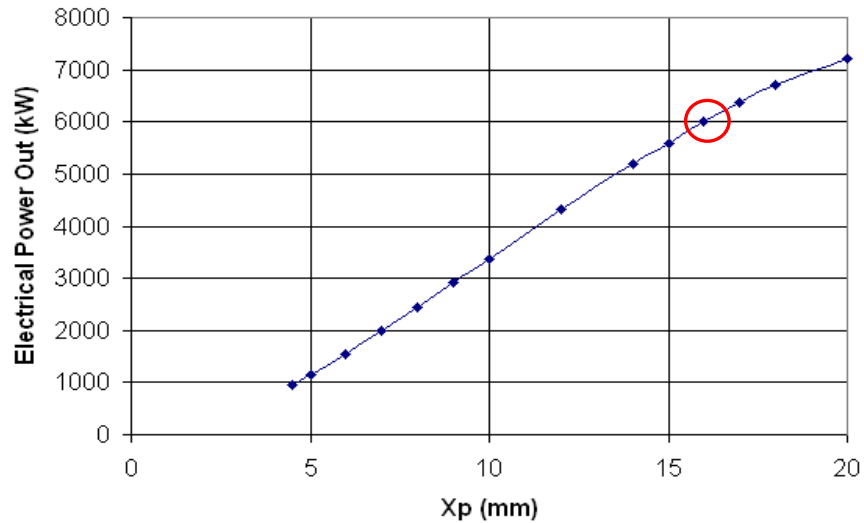


Figure 54.—Convertor power versus piston amplitude.

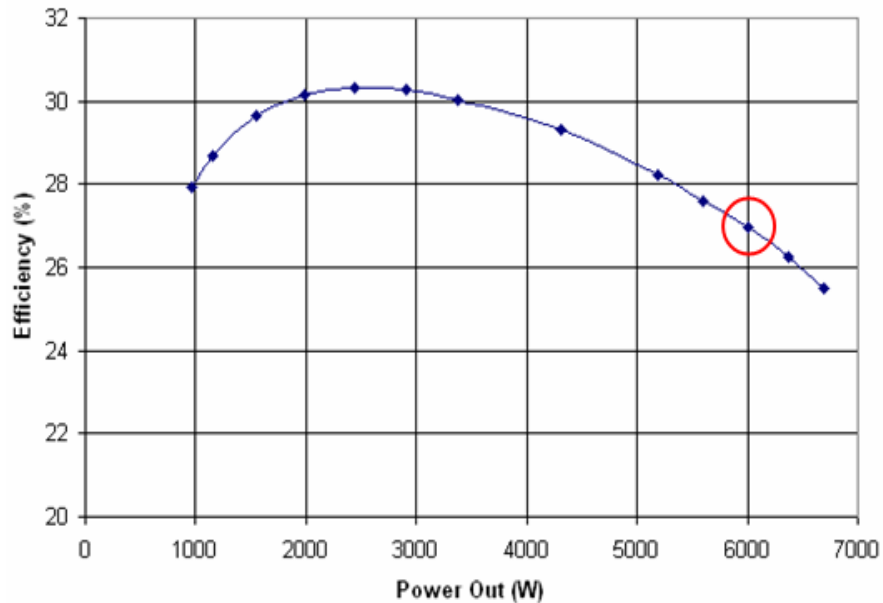


Figure 55.—Convertor efficiency (AC out/heat in) versus power.

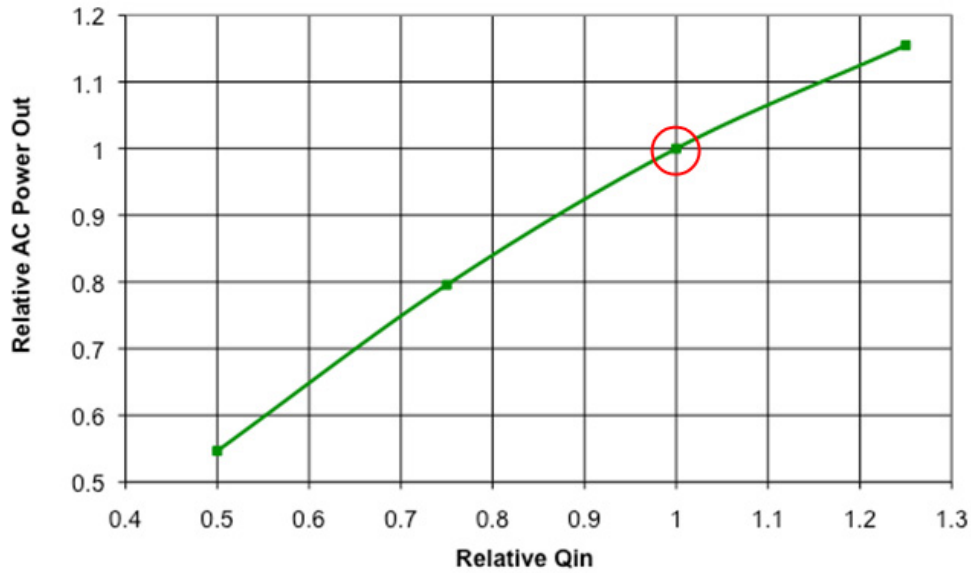


Figure 56.—Influence of  $Q_{in}$  on power out (converter is more efficient at lower  $Q_{in}$  because of reduced wall  $\Delta T$ ).

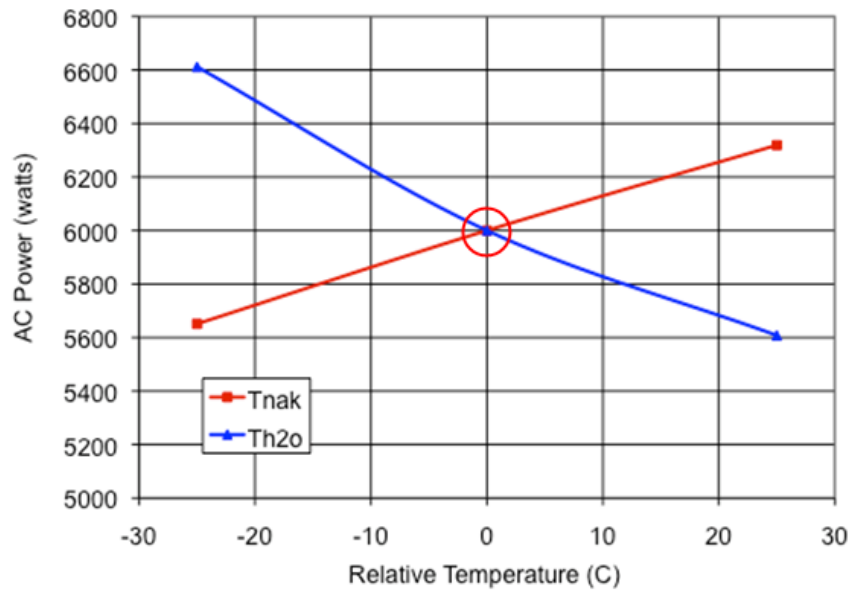


Figure 57.—Influence of NaK or H<sub>2</sub>O inlet temperature.

Figures 57 and 58 show the influence of the NaK and water inlet temperatures and flow rates on predicted performance. Figures 57 and 58 are for a fixed heat input. Figure 57 shows that for higher hot end temperatures, or lower reject temperatures, power output will increase. The higher flow rates simply result in lower temperature drops along the heat exchanger and either a higher average temperature for the acceptor or a lower average temperature for the rejector. As is seen the water flow rate has a very strong influence on power output.

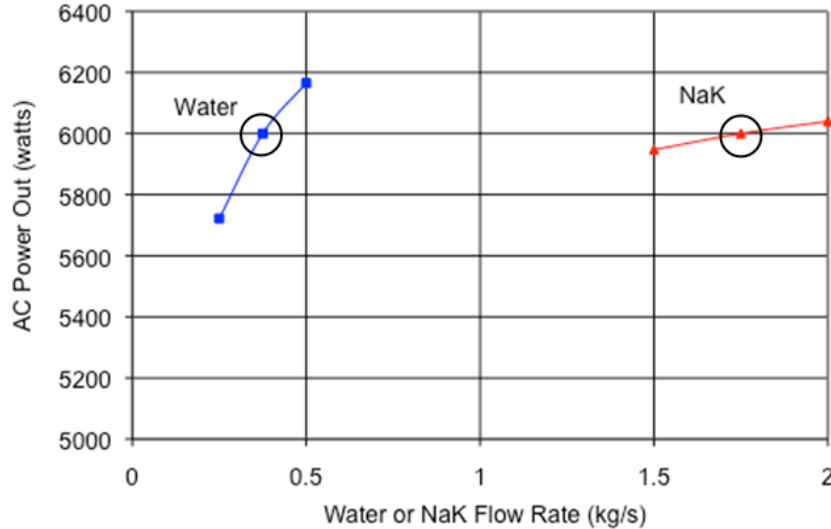


Figure 58.—Power versus fluid flow rate.

## FSP LM Acceptor Heat Exchanger

The selection and detailed design of the acceptor heat exchanger (HX) plays a significant role in the overall performance of the FSP. The following describes the process used to carry out the selection of the proposed acceptor HX for the FSP convertor followed by a detailed discussion of the characteristics of the selected design. Due to the nature of the FSP application, a number of constraints were imposed on the design; the impact of these will also be addressed throughout the review of the acceptor HX development process.

### Design Goals

The primary design goal for the FSP acceptor HX was to 1) maximize reliability under the FSP operating conditions over the design life of the system, while 2) providing highly effective thermal input to the convertor, and 3) be capable of being fabricated via proven manufacturing techniques. In addition, it would be advantageous if the specific concept had been demonstrated successfully in other Stirling cycle convertor hardware. These above goals tended to place a premium on reliability over pure performance issues.

### FSP System Imposed Constraints

The primary constraints placed on the evaluation of the acceptor HX represent a combination of those imposed by the test facility along with those that were utilized due to the unique characteristics of the LM heat transport fluid properties.

*Working fluid.*—The working fluid for the acceptor HX is a liquid metal mixture of 22 percent sodium (Na) and 78 percent Potassium (K). The thermophysical properties of this liquid metal (LM) are defined in (Ref. 1) which is based on an extensive database. In addition to the fluid selection, the facility imposed a number of constraints that had to be incorporated into the acceptor design process:

- Nominal LM inlet temperature = 850 K,  $\pm$  25 K (575 °C)
- LM supply (note for PCU) = 1.75 Kg/s,  $\pm$  0.25
- Maximum pressure drop across entire acceptor HX, 7000 Pa

Note that in the latter requirement, this includes not only the core of the actual acceptor HX, but also the required LM inlet and exit manifolds that provide the proper distribution of the LM to the HX. This represented a key factor in the design process since the actual pressure drop across the core of the HX was relatively low and small effects in the manifold design geometry could lead to significant difference in LM flow between individual HX passages.

*Interface materials.*—The chemical properties of the LM are such that unless a narrow field of materials is employed, there is the strong possibility of corrosion occurring in the assembly during the life of the hardware. To minimize this possibility, it was defined that only stainless steel alloy 316 would be employed as the material that comes in contact with the LM (Ref. 2). This simplified a number of issues in the design process from the viewpoint of the structural design since the maximum operating temperature, defined by the LM inlet temperature, the basic material properties at these temperatures, defined by extensive data in (Refs. 3 and 4), and the stated design life goals of the of the FSP were all readily available.

In some HX configurations, the use of another stronger material as the primary structure was an option. In this case the SS-316 to LM interface is still required. After discussions with the sponsor and evaluation of the extensive material/life database for this material/LM combination, it was agreed that a minimum of 1 mm of SS-316 material would be present at all LM interfaces. In addition to the purely chemical interaction between the LM and structure, there also exists the potential for local “erosion” of the wall material if the LM flow velocities are excessive. This issue was investigated in conjunction with the minimum wall material thickness constraint discussed above and it was determined that if the LM flow velocity were at or below 1 m/sec the erosion effects would be very small and would not compromise the HX life.

## **HX Configuration Options**

A number of Stirling cycle acceptor configurations have been developed and implemented in a wide range of power levels since the start of the “modern” Stirling engine efforts in the 1950s. During the 1990s, a number of higher power designs were proposed and /or built that focused on space applications. Initially, a number of these designs involved “tubular” acceptor HX (Ref. 5) where many (1000+) tubes were employed. While performance was very good with these HXs, serious issues existed on the overall reliability particularly when the tube joints are exposed to a LM heat transport fluid. These reliability and overall reactor/convertor issues led to the development of “modular” acceptor HX configurations (Ref. 6) and the “semi-tubular” Starfish concept (Ref. 7). The other fundamental acceptor configuration is generally described as a “monolithic” configuration where the HX is an integral portion of the primary pressure vessel containing the Stirling cycle. Because of the reliability goals of the FSP project, the conventional multi tube tubular HX configuration was eliminated from contention prior to the technical trade study used for the down select process. The following material provides a detailed description of the fundamental HX configuration considered. Due to their mechanical configuration, they can be generically categorized as either “semi-tubular” or “monolithic”.

### **Semi-Tubular**

It is extremely important to note that the specific HX configuration in this family evolved directly from the use of heat pipes coupling the reactor working fluid with the acceptor HX, not a LM pumped loop to be employed in the FSP. This fact plays an important role in defining a realistic FSP acceptor HX concept.

The Starfish configuration eliminated the need for tube joints by drilling the helium flow passages through ribs making up the HX structure while still retaining some of the thermal/structural advantages of the tubular HX. The basic configuration is shown in Figure 59. In this arrangement, the majority of the pressure induced loads are carried by the cylinder wall at the base of the ribs which is not involved in the process of transferring thermal energy to the cycle working fluid. The helium flow passages can be treated essentially as small diameter tubes from the viewpoint of the required wall thickness. This allowed

the effective wall thickness, through which the thermal energy must flow to reach the helium, to be on the order of 1 to 2 mm. The latter was defined primarily by the manufacturing issues involved with fabricating the desired passage diameter and the overall length of the heat exchanger.

For the FSP application, the previously discussed constraint of at least 1 mm of wall thickness in the areas exposed to the LM represents an additional limitation on the minimum wall thickness. While it is possible to fabricate the HX from a single piece of material (eliminating all joints between the helium and LM) there may be requirements when this configuration is used with a LM to incorporate one or possibly two welded or brazed joints which represent potential paths between the helium and LM working flow fluids. As noted previously, this configuration was employed as the condenser of a heat pipe with the sodium vapor condensing on the exposed surface of the ribs. This provided excellent uniformity of the temperature and heat flow to the engine due to the intensity of the condensation process. To incorporate this concept for the pumped LM loop utilized in the FSP would require that the outer spaces be reconfigured so as to provide the necessary flow conditions between the LM and the exposed rib structure. Since the fundamental heat transfer processes and densities of the heat transport fluids are dramatically different (condensation versus forced conduction and gas versus liquid) the changes required are significant.

### Monolithic Configurations

This widely used acceptor HX configuration is shown in Figure 60. This configuration is considered “monolithic” since the pressure vessel is one continuous metallic structure and as such totally eliminates any joints between the LM and helium working fluids. The LM would flow over the exterior surface of the pressure vessel through flow passages effectively forming the outer acceptor HX.

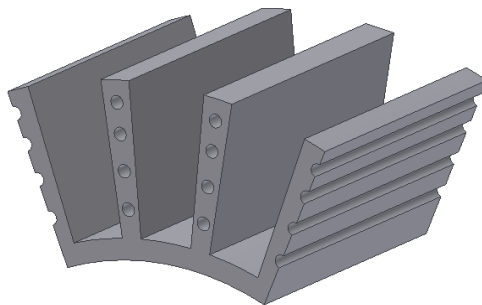


Figure 59.—Reference “Starfish” configuration—heat pipe condenser (semi tubular).

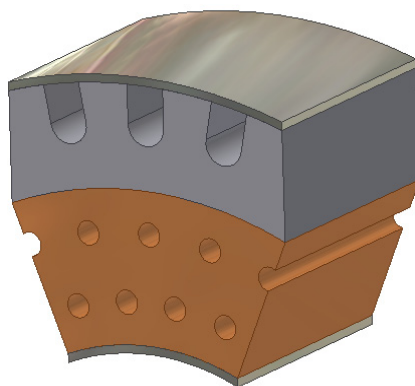


Figure 60.—Monolithic HX configuration.

This concept has found wide use due to its intrinsic simplicity and reliability. However, the heat flow from the LM to the helium must pass through the pressure vessel wall. The temperature drop between the outer wall surface and the side exposed to the helium is dependent on the wall thickness. It is the wall temperature adjacent to the helium working fluid that defines the Stirling cycle's hot end temperature that plays a significant role in defining cycle efficiency. The latter is defined by the pressure vessel material, the operating pressure of the convertor, and the diameter of the required HX. This combination of parameters has in some cases limited this configuration to power levels below 3 to 5 KW output power where the efficiency losses due to the temperature drop across the vessel wall are considered manageable and its low cost and high reliability characteristics are clearly retained.

### **Evaluation/Trade Study**

The overall evaluation process considered the details of the two basic HX described above as applied to the pumped LM heating system to be employed in the FSP. To carry out this evaluation, a number of specific issues needed to be addressed, which include among others: 1) details of the heat transfer between the LM and the surface of the basic HX structure 2) the effectiveness of the transfer of this thermal energy through the HX structure to the surfaces which are exposed to the helium, and 3) various structural/material parameters impacting the mechanical design of the potential HX configurations. The latter represents the starting point for the conversion of this energy into useful power via the convertor.

*LM heat transfer.*—The proposed LM working fluid (NaK 78) has thermophysical properties that differ dramatically from those associated with Stirling cycle devices heated either with combustion products or vapors via a heat pipe. In particular, the fluid density along with fluid thermal conductivities are much greater (the latter nearly the same as stainless steel) while the Pr number is very small. Other operating parameters of the FSP are also unique, such as the small temperature drop in the fluid passing through the HX and the essentially fixed inlet temperature.

In the case of the forced convection heat transfer for the LM to the HX wall, a very large, but dated, database exists for the determination of heat transfer coefficients of LM's flowing through passages under turbulent flow conditions and Reynolds number in the ranges expected in the FSP LM HX (Refs. 8 to 13, and others). This database was developed during the 1950s through the 1970s in support of the nuclear industry consideration of LMFBR (liquid metal fast breeder reactor) and potential space power related programs. This data is extensive not only in heat transfer but also in the area of material compatibility, with much being available for the preferred SS-316 at temperatures very similar to those proposed for the FSP.

With the exception of the effects of the high thermal conductivity and low Pr number values of the LM fluid, the basic relationships are very similar to those employed for other fluids such as water. Of importance is the fact that various relationships available, along with the associated test data and test conditions, are also available for the entrance/developing flow portions of the flow passages and for passages with relatively low L/D ratios since the values expected in the FSP application are  $<50$ .

Figures 61 and 62 give the Nusselt number relationship used in the evaluation of the heat transfer process, note the effects of the low Pr number for the LM is captured in the Pe number which is the product of the Re number and the Pr number. A Nu multiplier is also shown which was applied in cases where the flow passage entrance conditions were a significant proportion of the overall HX length – these effects become relatively small at passage length to diameter ratios  $>20$  (Refs. 9 and 10). Because of the small bulk fluid temperature changes over the length of the HX, it was possible to use properties at the average bulk temperature of the fluid in the HX. Properties employed for the NaK 78 in the evaluation process are based on the relationships noted in (Ref. 1).

As noted above, the LMs unique thermophysical properties will impact the definition of the basic HX geometry in a manner which is considerably different relative to conventional single phase working fluids. These LM characteristics when combined with the constraints imposed by the material selection must be carefully considered during the HX evaluation process.

At the LM fluid velocities and expected flow passage geometries, the flow conditions will be turbulent throughout the “core” of the HX. Under these conditions the heat transfer coefficients will be well in excess of  $10,000 \text{ W/m}^2 \text{ }^\circ\text{C}$ . As noted in Figures 61 and 62, and schematically in Figure 63, the LM passage geometry is essentially one in which the flow is through slots of width “a” and height “H” with the number defined by the specific HX configuration and convertor basic dimensions. The best HX performance, defined as the smallest difference between the bulk LM temperature ( $T_{lm}$ ) and the effective surface temperature of the HX at the LM interface ( $T_w$ ), occurs as the rib or fin width decreases— basically moving down in Figure 56. This is due to the fact that the ribs or fins have very poor fin efficiency with the combination of the LM heat transfer and SS-316 thermal conductivity.

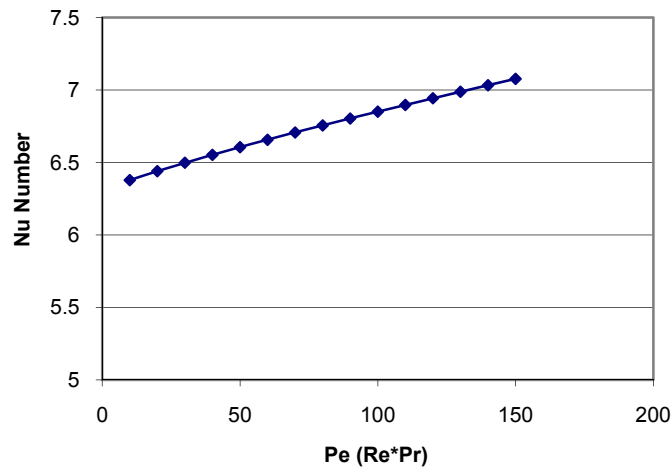


Figure 61.—LM heat transfer relationships.

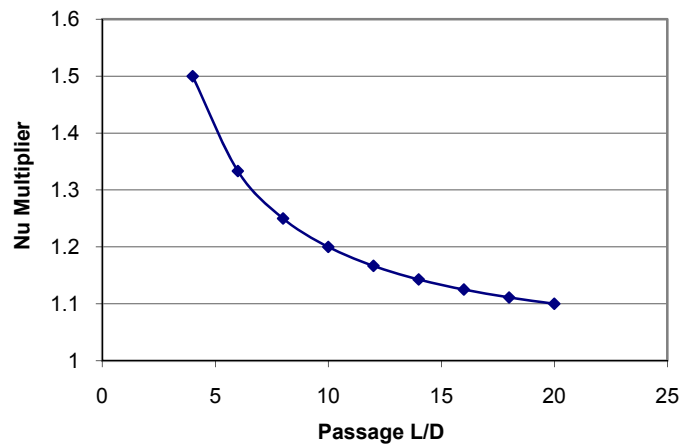


Figure 62.—LM heat transfer multiplier for passage  $L/D < 20$ .

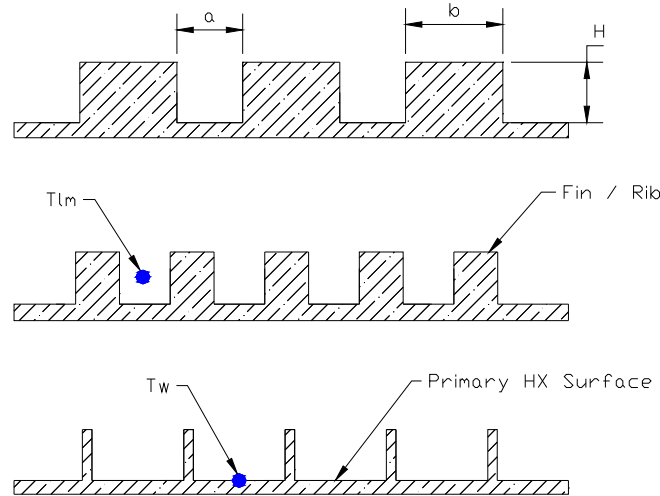


Figure 63.—LM HX flow passage geometry.

Therefore, the most effective surface for overall heat transfer is the surface noted as “primary HX surface”. This is maximized when the ribs are essentially eliminated—i.e., an annular gap HX. However, there are a number of reasons and advantages for utilizing the rib structure: 1) it is required in the externally reinforced configuration which will be discussed in a later section, 2) the flow passages are fully defined, 3) there is no chance for circumferential flow once the LM has entered a passage, and 4) the design of the inlet/exit flow manifolds is simplified since there is a well defined passage distribution. In addition to the above factors, design and analysis of a simple annular gap LM HX currently entering testing (Ref. 14) indicates a strong, very complex coupling between the inlet flow manifold and heat transfer characteristics/distribution both axially and circumferentially with the annular HX configuration. For these reasons the annular configuration was eliminated from further consideration.

In addition to the heat transfer effects, the fluid pressure drop across the HX is a design constraint as noted previously. For the “core” of the acceptor HX that is made up of a relatively large number of small channels, the pressure drops could be incorporated into the initial analytical models to size the HX for heat transfer. It was expected that these pressure losses would be relatively low due to the low flow velocities occurring in the HX ( $\leq 1$  m/sec constraint). However, the total loss across the entire HX and its associated flow manifold system is very hard to evaluate via simplified analytical models due to the complexity of the flow path and the close coupling of various geometrical changes in the flow passages. The latter was addressed via more sophisticated CFD modeling tools.

In practice, the basic approach employed for the evaluation of the heat transfer and pressure drop though the core portion of the HX was carried out by breaking the HX down into sections along its axial length and evaluating the conditions in each section. Various boundary conditions for each section were developed based on an iterative approach that involved estimating a wall heat flux axial distribution from the Sage simulation model for a specific wall temperature distribution. This was used as the input to the LM HX model from which a new wall temperature distribution would be developed and applied to Sage for updating. For initial screening, the nominal LM flow rate was employed. As the modeling continued, the conditions over the entire allowable flow range were considered.

The primary result of this process was a LM flow passage geometry and flow passage number that met all of the imposed constraints. This was used as the starting point for the CFD based evaluation. In the case of the acceptor HX, the vast majority of the CFD effort focused on developing the manifold geometry so as to insure that the flow was as close as possible to being uniform. The flow velocity constraints were met in the manifold, and the overall system pressure drop was within specifications.

*Heat exchanger thermal characteristics.*—The heat transfer through the structure of the possible acceptor HX concepts is relatively straight forward since the number of acceptable materials is limited and the operating temperatures are not particularly high.

All materials in contact with the LM are constrained to be SS-316 for which a number of excellent sources are available for detailed mechanical and physical properties (Ref. 3 and 4, and others). Higher strength materials that are not in contact with the LM were limited to those that were compatible with SS-316 via either brazing or welding. For reference purposes, these are IN-625 and IN-718 that while not fully proven to be compatible with LM, are reasonably resistant should they come in contact with the LM during testing. The primary internal heat exchanger material (exposed only to helium) is OFHC Copper – due to CTE issues, this material was restricted to being attached only to SS-316. This particular braze joint has been used extensively and has a very high intrinsic reliability. With the exception of the copper, the thermal conductivities of all of the materials under consideration are fairly close and on the order of 1/15<sup>th</sup> that of the copper. This implies that relatively thin sections of these materials will result in significant temperature drops within the HX structure.

The structural design constraints imposed for the preliminary assessment of the HX configurations are summarized in Table 17. In many cases, they represent recommended limits defined by the ASME Code for nuclear industry components. In the case of the copper components within the HX, they were assumed to provide little if any structural support to adjacent elements and did not carry any significant structural loads during convertor operation. Note that as the design process became more detailed, these parameters were also updated so as to take into account effects that were captured in the FEA evaluation of the final configurations.

TABLE 17.—STRUCTURE AND MATERIAL GUIDELINES—ACCEPTER HX AT EXPECTED OPERATING TEMPERATURES

Parameter	Nominal Value	Comments
SS-316		
Yield strength (MPa)	120	ASME
Ultimate strength (MPa)	420	ASME
Creep strength (MPa)	110	ASME
Deformation constraint (MPa)	110	Based on 1% in 100 K hr
Thermal conductivity (W/mK)	22	
CTE (1/°C)	20×10 <sup>-6</sup>	
IN-718		
Yield strength (MPa)	920	MMPDS-02
Ultimate strength (MPa)	1100	MMPDS-02
Creep strength (MPa)	N/A	Design based on yield
Deformation constraint (MPa)	N/A	
Thermal conductivity (W/mK)	20	
CTE (1/°C)	15×10 <sup>-6</sup>	

As noted in Figure 64, the key item of interest is the total temperature difference ( $DT_{total}$ ) between the bulk LM temperature ( $T_{lm}$ ) to the surface exposed to the helium working fluid ( $T_{wg}$ ). As noted previously,  $T_{wg}$  is essentially the starting point for the Stirling cycle.

A number of the intermediate temperature points are also of interest, particularly the difference between the LM interface wall temperature ( $T_w$ ) and the interface with the internal copper heat exchanger ( $T_{wg}'$ ) in the monolithic HX configuration (middle) since this represents the penalty in temperature drop by transferring the thermal energy across the main convertor pressure vessel. In the case of the “Starfish” configuration (top) the thickness of the “structure” is generally defined by the 1 mm minimum SS-316 material requirement (or possibly manufacturing constraints). In the case where the rib containing the helium flow passage is heated from both sides as shown the effective value of the helium side wall temperature ( $T_{wg}$ ) must take into account the non uniform temperature distribution. The latter can be

captured by assuming that the individual passage is essentially bounded by a fin surface, the thickness, and height of which is dependent on the passage number, spacing, and actual structure thickness. Since the material is SS-316, the thermal conductivity is low so the fin effectiveness can be low. If the helium flow passages are constrained to be spaced such that they don't effectively receive heating from both sides, (top right side) the effective temperature at the helium interface ( $T_{wg}$ ) will fall even further relative to the drop occurring across the 1 mm wall structure.

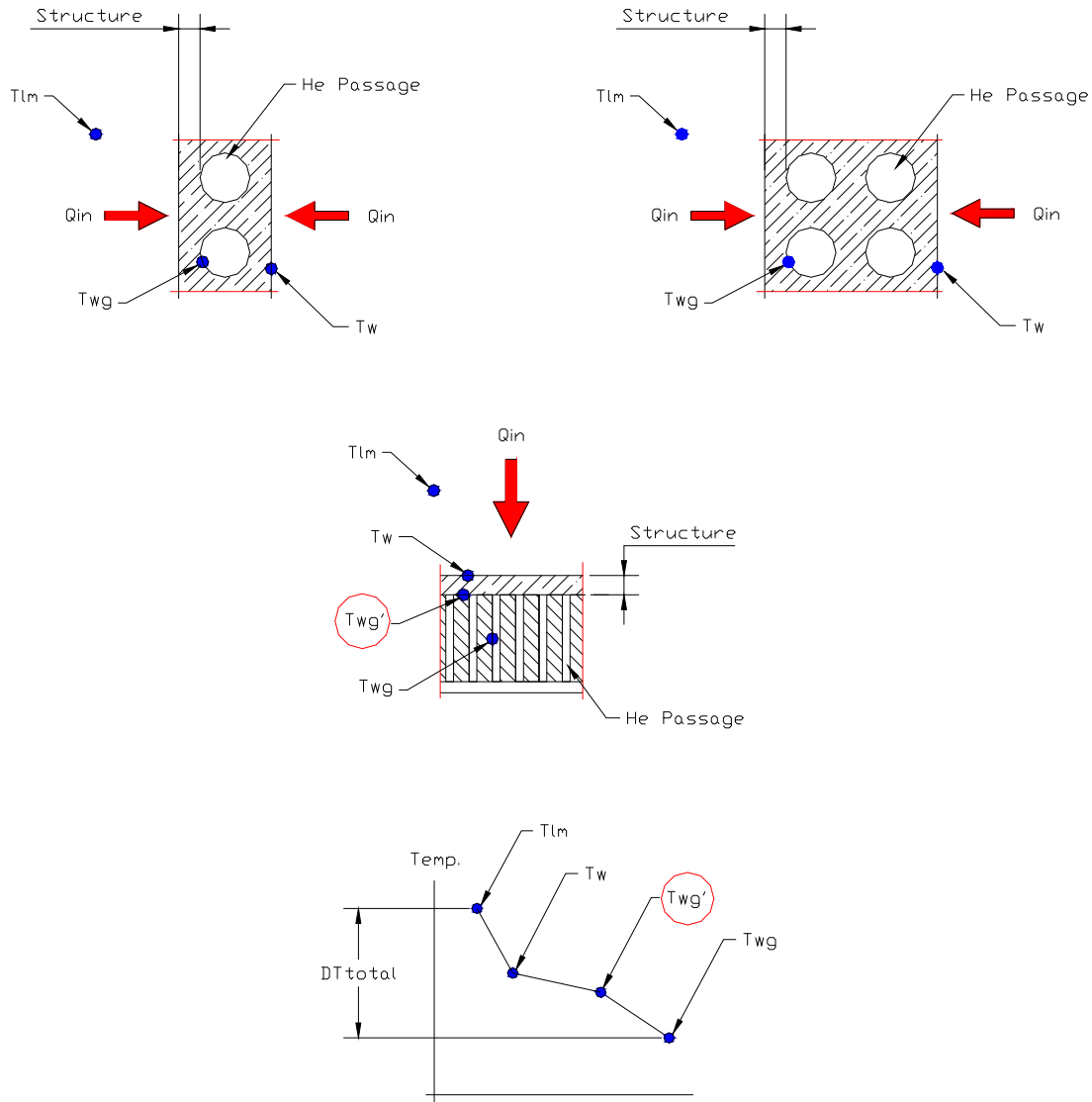


Figure 64.—Acceptor HX thermal environment.

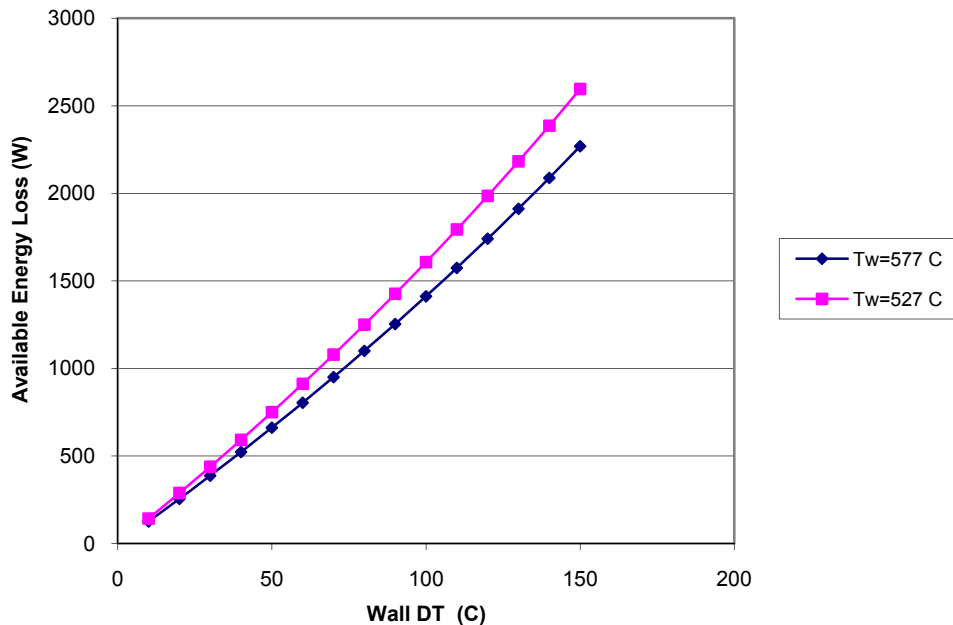


Figure 65.—Relative available energy loss versus HX wall DT.

### Available Energy Loss Evaluation

As discussed previously, the combination of a relatively low source temperature of 850 K (577 °C) and high sink temperature 375 K (102 °C) places a premium of minimizing the various temperature drops in the acceptor and rejecter HX so as to maximize the convertor cycle effective temperature ratio. However it is useful to have an evaluation tool that provides a way to define the relative effects of the specific temperature drops within the HX assemblies. This metric allows the relative sensitivity of the convertor performance to various HX hardware changes.

The “Available Energy Loss” parameter is essentially a measure of the entropy generation and the final sink conditions, which is defined in the current FSP. If it is assumed that the wall temperature ( $T_w$ ) at the interface with the LM is at the LM source temperature (850 K/577 °C), an ideal case that never can be attained, the impact on wall DT (defined as  $T_w - T_{wg}$  or  $T_{wg}$ ) is shown in Figure 65. Also, shown is a more realistic case where the average value of  $T_w$  is 800 K (527 °C).

Using the above relationship it is possible to assess what penalty is imposed on the convertor due to the introduction of the DT’s present in the detailed HX layout. This parameter was used throughout the evaluation process of the various configurations.

### Specific Concept Evaluation

The two basic concepts selected for refined evaluation were the monolithic and semi-tubular configurations noted above. The following material provides a summary of the results of the evaluation.

#### Semi Tubular Configuration

In the case of the “Starfish” variants, the key challenge was to provide the necessary LM heat transfer at the interface between the flowing LM and the rib structure that contains the helium flow passages while simultaneously packaging the desired number of helium flow passages. The basic Sage simulations/optimizations provided a good estimate of the regenerator outer diameter and the displacer diameter which also defines the approximate height of the ribs/LM flow passages. In addition, the number and diameter of the helium flow passages are also defined.

Based on the items discussed above, the minimum LM flow passage dimension allowed is about 1 mm that for the current configuration defines the minimum “width” of the passage. A representative height of the passage is on the order of 32 mm. Note that the passage can be of greater width but the constraint of the maximum LM flow velocity of 1 m/sec must also be met. Spacing between the individual flow passages was set at approximately one tube diameter resulting in a value of 4 mm. With a 2 mm diameter helium flow passage (tube) diameter about 8 or 9 passages are present in each rib assuming they are in line along the length of the rib. Due to the minimum SS-316 material thickness, the minimum rib thickness in this case is somewhat in excess of 4 mm, which is a significant manufacturing challenge. Since it is desirable that the LM passages be of constant width to provide a uniform heat transfer coefficient on the HX surface, the number of potential passages is defined by the sum of the passage width and the rib width that can be placed around the inner PV cylinder OD (about 135 mm in the reference case) which is defined by the displacer diameter. The resulting configuration becomes the equivalent to that shown schematically in the upper part of Figure 66 (note no scale is implied).

Under specific conditions it may be desirable to make the rib wider so as to contain two sets of helium flow passages (see bottom of Fig. 66). In this case, the LM flow velocity can be increased if desired.

In the case of the in-line helium passages, Figure 67 depicts the tradeoff between the number of helium passages available (defined by the Sage simulation model) along with the various mechanical/manufacturing/geometrical constraints. As seen, the temperature difference ( $T_{lm}-T_w$ ) can be relatively small due to the combination of a relatively large surface area at the interface between the LM and the HX wall. However, the number of passages is limited—for example, in the case shown with the minimum LM passage width “a” constraint of 1 and 2 mm diameter helium passages, the number available is somewhat below 600 while the optimum number for the Stirling side is on the order of 1000 or more. Note that while the final design of the internal acceptor has only 150 slots, these are equivalent to more than 3000 circular passages.

### Monolithic Configuration

The basic monolithic configuration as shown previously, has a vessel wall thickness defined by the structural material strength, convertor operating pressure, and the diameter of the vessel which is generally defined by the required regenerator diameter. For the case of the simple monolithic head fabricated from SS-316, the representative wall thickness required is in the range of 6 to 8 mm that would yield a temperature drop across the structure ( $T_w-T_{wg}$ ) on the order of between 120 and 140 °C. These large values would result in significantly lower helium passage wall temperatures ( $T_{wg}$ ) and in turn, low cycle performance. Because of these issues, the simple, all SS-316 monolithic configuration was eliminated as a prime candidate in the monolithic HX options.

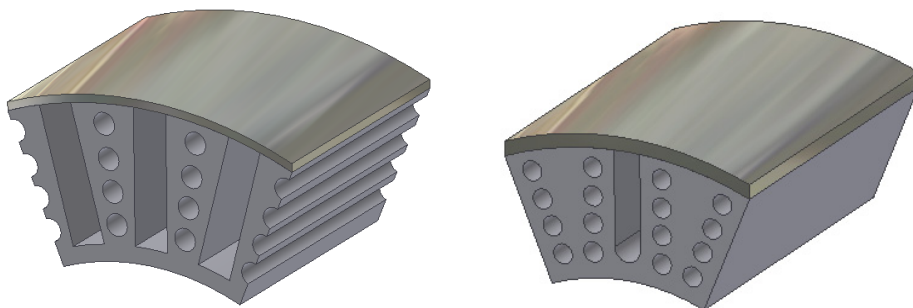


Figure 66.—“Starfish” HX configurations—conventional (left) and multiple set of He passages (right).

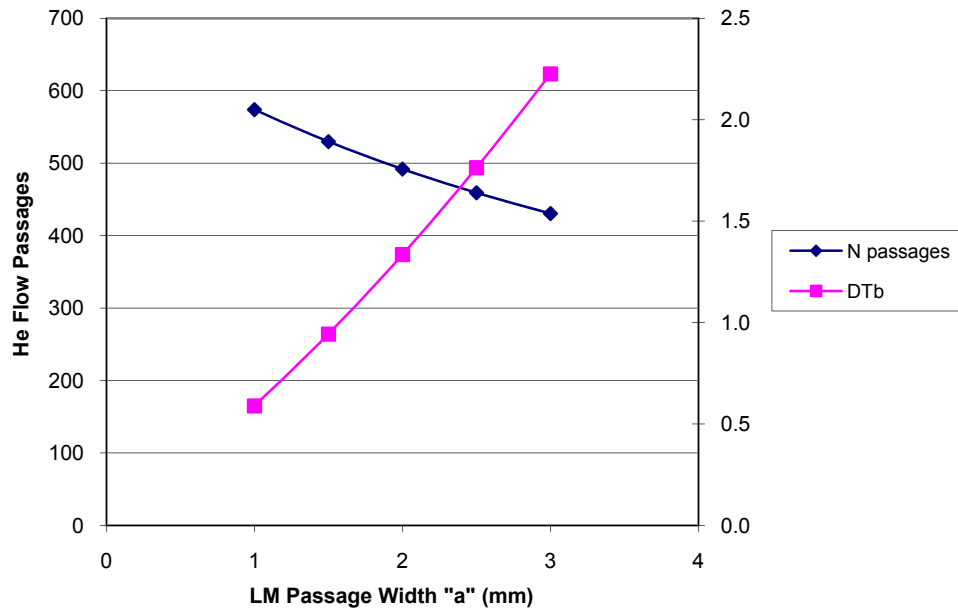


Figure 67.—Relationship between available He passage number and HX operating characteristics.

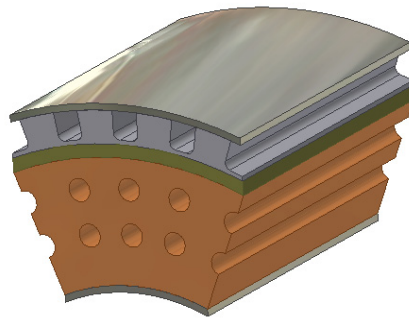


Figure 68.—Internally reinforced monolithic HX configuration.

The next configuration evaluated is shown in Figure 68. In this case, the 1 mm SS-316 minimum wall thickness is retained, but the primary structural loads are carried by a higher strength *internal reinforcement*, such as IN-625 or IN-718. Under comparable operating temperatures, these latter materials have allowable stress levels in the range of 2 to 3 times that allowed for SS-316 (Refs. 3 and 4). If it is assumed that the reinforcing structure carries all the pressure induced loads the resulting total wall thickness is in the range of 3.5 to 5 mm. Since the thermal conductivities of the SS-316 and these Ni based superalloys are relatively close, the resulting temperature differences across the structure ( $T_w - T_{wg}$ ) are on the order of 65 to 90 °C which is still a considerable value. An additional issue in the implementation of this concept was the issue of the difference in the differential expansion coefficients between the SS-316 and the potential Ni superalloy reinforcements. Based on these results, the internally reinforced HX configuration was retained for consideration in the trade study because of its intrinsic high reliability from the viewpoint of overall design. The previously mentioned material considerations and performance losses due to wall temperature drops represented the key negative aspects of this configuration.

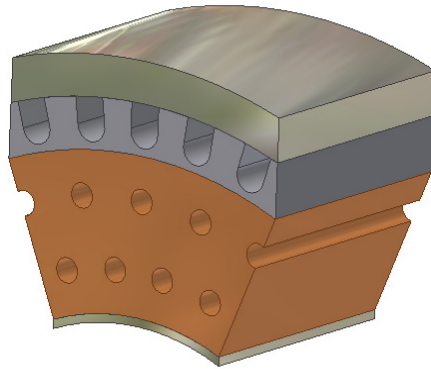


Figure 69.—Externally reinforced acceptor configuration.

The final concept evaluated in detail from the monolithic HX family was an externally reinforced configuration as shown in Figure 69. In this case, the thermal energy flows only through the 1 mm thick SS-316 inner shell while the primary pressure and thermal induced loads are carried by an external reinforcement structure. Here the HX rating temperature drop ( $T_w - T_{wg}$ ) is in the range of 17 to 20, a reduction of a factor of 3 to 6 times over the other monolithic configurations. In this case, the ribs/fins must be sized to carry the compressive load transferred from the inner structure to the outer reinforcement. As shown in Figure 70, the sizing of these ribs, essentially the definition of the parameter “b”, must be incorporated into the design of the HX. In addition, the width of the LM flow channels “a” must take into account the pressure induced loads in the span between the ribs.

To be conservative, it was assumed that the Cu internal HX structure provided no structural support to the SS-316 material. Based on the previously discussed material operating constraints and the operating pressure/diameter of the reference FSP convertor, the allowable passage widths “a” ranged between 5 and 6 mm. Since no thermal energy flows through the external reinforcement, its thickness is defined solely by load carrying requirements. While the possibility exists to employ high strength materials for the external reinforcement, the design constraints would still require at least 1 mm of SS-316 to be present on the inner surface of the reinforcing material that is adjacent to the LM flow. Due to CTE mismatch, there was a concern about utilizing IN-718/SS-316 combination. Because of this concern, it was assumed that the reinforcement would be fabricated from SS-316. This increases the required mass but dramatically reduces technical risks.

### Concept Rating/Trade Study

At the completion of the concept review, the various configurations were rated and a reference configuration was selected. Table 18 notes the criteria used in this evaluation process. A total of 4 concepts were considered: 1) the simple all SS-316 monolithic configuration), 2) the internally reinforced configuration with an IN-718 reinforcement material 3) an externally reinforced configuration fabricated completely from SS-316, and 4) a modified “Starfish” configuration.

TABLE 18.—LM HX RATING CRITERIA

Parameter	Weighting Factor (%)
Reliability	35
Development Risk	30
Cost	20
Efficiency	10
Mass/Volume	5

The resulting rating for the four configurations has the externally reinforced as the best option followed by the internally reinforced configuration. The “Starfish” configuration fell into 3<sup>rd</sup> place with the all SS-316 monolithic in last. It is interesting to note that the monolithic configuration lost due to performance and mass issues but was rated high in reliability, risk, and cost.

The primary differentiation between the internal and external reinforced configurations was the technical risk incurred by the requirement that the SS-316 material had to be attached to the IN-718 reinforcement material. Due to CTE issues between the two materials, there were concerns about the feasibility of the process and in turn an increased risk. The externally reinforced configuration had superior HX performance but did incur some risk due to the limited experience at Sunpower with this concept and issues concerning the installation of the external reinforcement material.

The “Starfish” configuration had good HX performance but there was considerable concern in the areas of fabrication techniques that would actually allow these performance levels to be attained. In addition, there were issues concerning the LM flow characteristics in the thin passages (widths of about 1 mm).

Based on the above results, the externally reinforced configuration was selected as the reference LM HX configuration for the FSP.

### **Selected Concept**

After approval of this selection by the sponsor, the detailed design of the acceptor HX was completed. Since the basic tools for detailed definition of the “core” of the HX were developed in earlier portions of the evaluation, the detailing effort actually focused more on design of the required inlet/outlet LM manifolds and evaluation of the overall LM side fluid pressure drops. This was important since the earlier evaluation indicated that the “core” of the HX had relatively low pressure drop. It was expected that the higher order CFD analysis would confirm these values along with providing the manifold additional pressure drop values.

### **Design Details**

Optimization of the LM side of the acceptor HX was carried out based on the configuration shown schematically in Figure 70. The process involved a number of iterative steps with the LM HX geometry since various parameters in the overall convertor optimization process were introducing changes that in some cases cascaded over into the design constraints imposed on the acceptor HX. These generally involved the overall length of the acceptor HX and some variation in its outer diameter. In addition, other HX related constraints evolved from the evaluation of the FSP structural analysis of the areas of the external reinforcement and the interface of the acceptor HX to the pressure vessel surrounding regenerator.

At the completion of this process, the “reference” FSP LM HX configuration was fully defined. The configuration was evaluated from the viewpoint of its basic operating characteristics over the range of LM inlet temperatures and flow rates specified in the FSP SOW. Concurrently with the latter portion of this effort, the design of the LM manifold started. The then existing LM HX passage geometry was employed in the initial evaluation process. While a few minor variations occurred, the basic LM HX flow passage geometry remained unchanged during the detailed CFD based evaluation of the manifold. The primary output of the CFD based design from the HX viewpoint was a description of the flow rate distribution in the individual LM channels around the circumference. This variation was evaluated from the viewpoint of the change in heat transfer coefficients and LM to wall heat transfer. In addition, the CFD model was also employed to evaluate the change in the inlet temperature and flow rate of the LM as defined in the FSP SOW. Overall, the empirical models employed in the evaluation of the LM HX provided a good match with the CFD results from the viewpoint of the heat transfer process between the bulk LM and the wall along the length of the HX. Details of the CFD based evaluation of the LM manifold are given in a later section of this report.

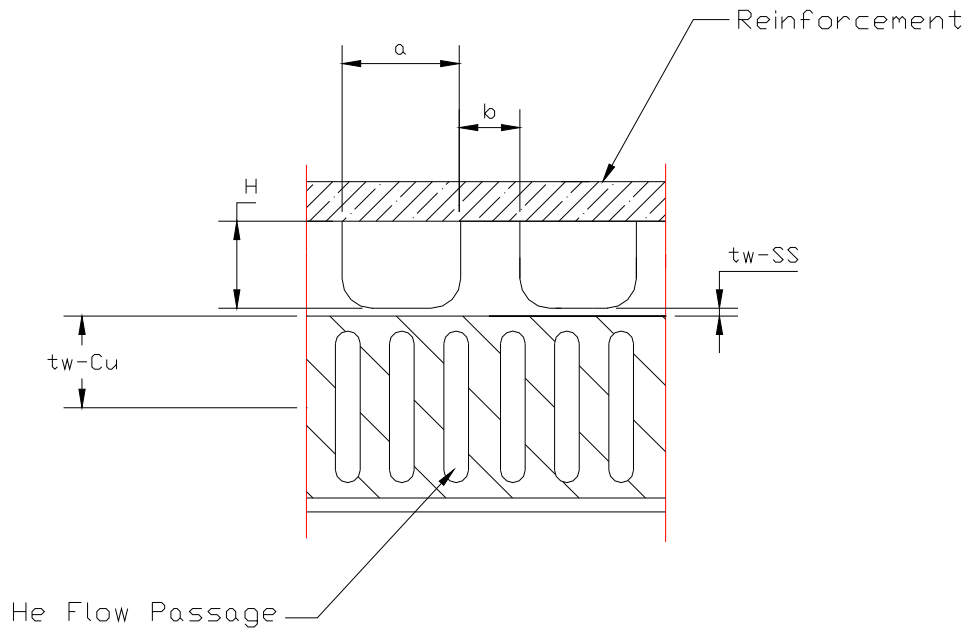


Figure 70.—Reference HSP acceptor HX configuration parameters.

The technical evaluation process involved applying a Sage simulation derived heat flux distribution along the length of the LM HX model which is broken down into a number (between 10 and 20) sections where an energy balance based calculation is carried out on each section. This distribution is defined for a specific wall temperature distribution. As the HX modeling progresses, the wall temperature and in turn the heat flux distribution can change leading to a new simulation case. While not absolutely required, it was initially assumed that the passage geometry did not change along the length of the HX so as to simplify the fabrication and meet the requirements that the rib structure transfer the mechanical loads to the surrounding reinforcement structure. The evaluation process clearly indicated that this assumption had very little impact on the overall HX performance.

The passage width “a” is constrained by the allowable operating stresses in the SS-316 material and convertor operating pressure. Figure 71 indicates the variation in the stress over the span between the ribs for two modeling cases along with the allowable operating stress based on (Refs. 3 and 4) for 10,000 and 100,000 hr operation with the constraint of 1 percent deformation. Based on this evaluation the passage width falls between 5.7 and 6.3 mm if the 100,000 hr constraint is imposed. Based on this evaluation the passage width was set at 6 mm. The remaining parameters, height “H” and rib thickness “b” were then optimized to provide a combination of a low temperature difference ( $T_{lm}-T_w$ ) so as to minimize DT losses and pressure drop through the core of the HX. The latter was evaluated as a fraction of the allowable pressure drop across the entire acceptor HX that was set at 7000 Pa in the FSP SOW.

Table 19 summarizes the operating characteristics of the LM HX along with defining key geometric parameters. The information provided in the table was supplied as the initial input conditions for the CFD design of the integrated LM manifold/HX. Note these values are for a single LM HX, two identical HX are employed.

Figure 72 depicts the changes in the average operating conditions for the LM HX when the LM mass flow rate and inlet temperature are changed over the total range defined by the SOW. As can be seen, the change in inlet temperature is directly related to the effective HX wall temperature ( $T_w$ ) assuming the heat flow to the wall is essentially constant over the range noted. The mass flow change has a smaller effect on the effective wall temperature and has a nearly linear impact on the pressure drop across the core of the HX.

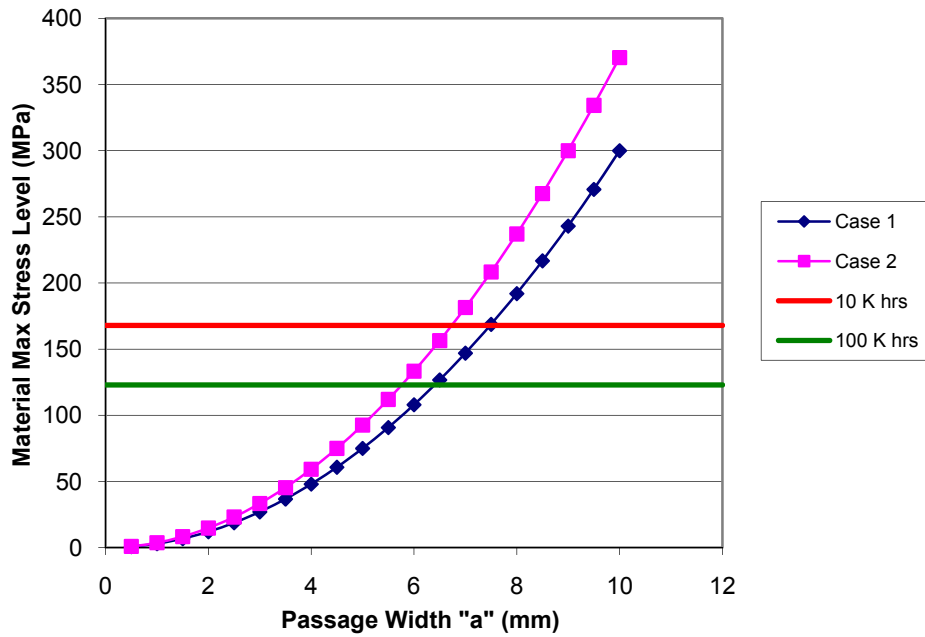


Figure 71.—Maximum stress level versus passage width.

TABLE 19.—REFERENCE LM HX CHARACTERISTICS

Parameter	Nominal Value	Comments
LM flow rate (kg/sec)	0.875	FSP SOW
LM inlet temperature (°C)	577	FSP SOW
Required heat input KW	24	Based on 25% efficiency
HX length (mm)	90	Sage simulation
HX outer diameter (mm)	212	Sage simulation
Passage number	66	HX optimization
Passage width "a" (mm)	6	
Passage height "H" (mm)	4.5	
Rib width "b" (mm)	3.9	
LM velocity (m/sec)	.67	
Hydraulic diameter (mm)	4.73	
L/D	19	
Re	14300	
Nu mean	6.74	Refs. 8, 9, and 10
Nu multiplier	1.22	Refs. 9 and 10
Heat trans. coeff. (W/m <sup>2</sup> °C)	45200	
Fin effectiveness	.2	SS-316
(T <sub>lm</sub> - T <sub>w</sub> ) mean (°C)	11.3	
(T <sub>w</sub> - T <sub>wg'</sub> ) (°C)	18.6	SS-316 wall
Core HX DP (Pa)	1200	Estimate—no manifold

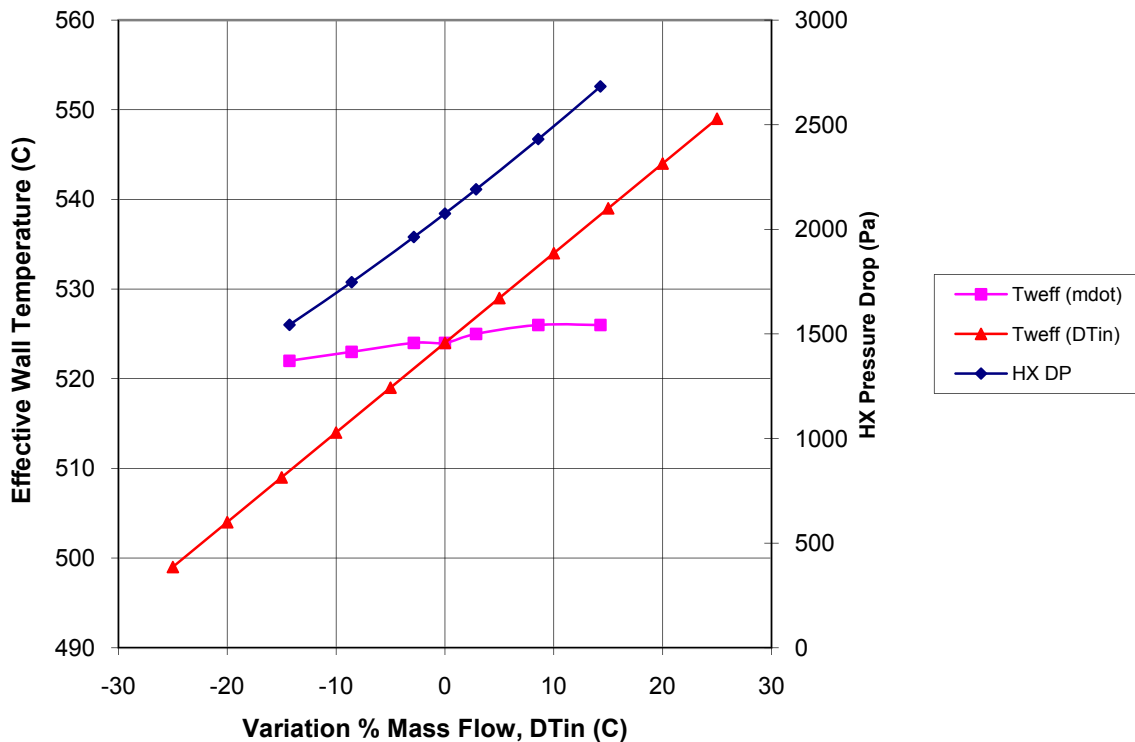


Figure 72.—Off design operating characteristics of reference FSP LM HX.

### Integrated LM Manifold/HX Design Evaluation Process

During the latter stages of the detailed design of the “core” of the LM HX, an effort was started to employ CFD modeling techniques to define the various flow manifolds required to distribute the LM to the HX. The goal was to provide as uniform a flow in the LM passages as possible while also minimizing overall LM pressure drops. These characteristics were desired over the entire LM flow rate variation range defined in the FSP SOW.

### Summary/Conclusions

The evaluation and selection of the final LM HX configuration investigated a range of potential configurations and applied a number of design tools developed specifically to support the unique operating environment of the proposed FSP PCU. The down select process placed a premium on reliability and lower risk configurations and, as such, thermal performance was not the dominant driver.

The selected externally reinforced configuration represents a significant advancement in the use of the highly reliable monolithic HX configuration concept in a manner that does not overly penalize this basic configuration at the higher power levels of interest in the FSP PCU.

Based on the results of the evaluation process, the following items are recommended for consideration in the hardware development effort:

1. Further refinement of the techniques to install the external reinforcement material in a manner which minimizes the potential for structurally degrading interactions with the LM working fluid
2. Early flow testing of the LM manifold system so as to insure that the interface with the “core” HX, flow distribution, and overall pressure drops are in line with CFD expectation (Ref. 15)—

this testing can be carried out with water as a simulant and plastic manifold components produced via rapid prototyping concepts

3. Refined thermal/structural analysis of the internal Copper HX structure from the viewpoint of its ability to provide a load carrying capability supporting the SS-316 HX structure

## Operating Parameter Trades

The basic operating parameter trades were performed by consultant David Gedeon, author of the respected Stirling simulation code Sage. For these studies, we assumed that the piston would be resonated entirely by the working and bounce space pressure swings, implicating no separate piston gas or mechanical springs would be included. For the study, the piston mass was defined by equations representing how the main piston mass would change with piston bore. The magnet mass of the alternator was defined in terms of piston bore, amplitude, and operating frequency.

From experience, we knew that unconstrained optimizations go to very large sizes and low frequencies to minimize through-wall temperature drops and internal losses. Therefore, we imposed a 'sensitivity factor' upon the diameter of the heater head. Here we set a size penalty on heater head diameter of 1 efficiency point for 40 mm of head diameter.

We also imposed a restriction that the pressure drop in either the compression space or the expansion space manifold could not exceed 5 percent of the total heat exchanger loop. This insured that the manifold height and volume were adequately sized to reduce flow non-uniformities, one of the difficulties of larger machines.

Figures 73 and 74 give the primary results of this study. As seen in Figures 73 and 74, increased pressure results in reduced gains in efficiency above a value of around 70 bar, and reduced frequency tends toward better efficiency.

Since these were very early studies, it is the trend of the plots which is important. As the design progressed, we found it necessary to force the regenerator length to be longer than the optimum in order to reduce stresses in the regenerator wall. In these studies, the regenerator length at the final selected pressure and frequency was close to 35 mm; however, we found it necessary to later force this up to 55 mm. We realized also that the longer regenerator would help reduce the detrimental effect of jetting at the ends of the gas entering from the heat exchangers (discussed in section a later section).

The most influential factor in leading to the final efficiency from that shown in Figures 73 and 74 is that the rejector design was changed. These early studies included a modular insert rejector heat exchanger such as was used in the SPDE. There was no attempt to model the outside heat transfer, and constant wall temperatures were assumed. We later switched to the finned internal water design, which inherently has higher temperature drops. The selected rejector design is less costly and has fewer joints which enhance reliability.

Based on these studies and additional simulations using feedback from the hardware layout, we initially selected 50 bar and 50 Hz for our design point. After the layout was sufficiently defined to allow a mass estimate, we found the convertor to be much heavier than expected. Because of this, we later switched to 60 bar and 60 Hz. for our design point to reduce mass. In retrospect we should maybe have pushed this even further (70 bar) and 70 Hz. to further reduce mass. The advantage of 60 Hz. is that it greatly eases early hardware development as the convertor can be connected to the local grid. Thus, hardware development can precede independent of the controller development.

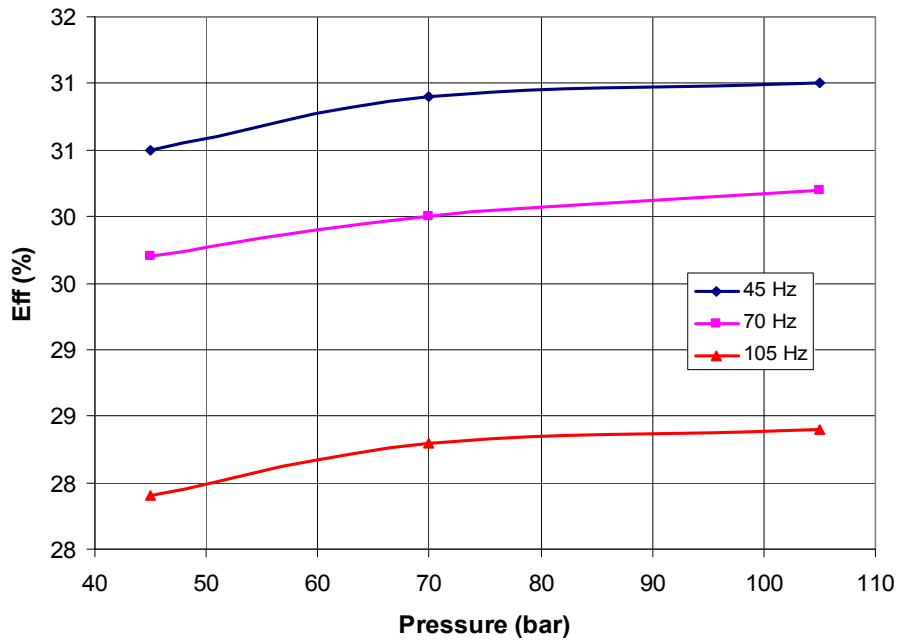


Figure 73.—Influence of pressure on efficiency at different frequencies.

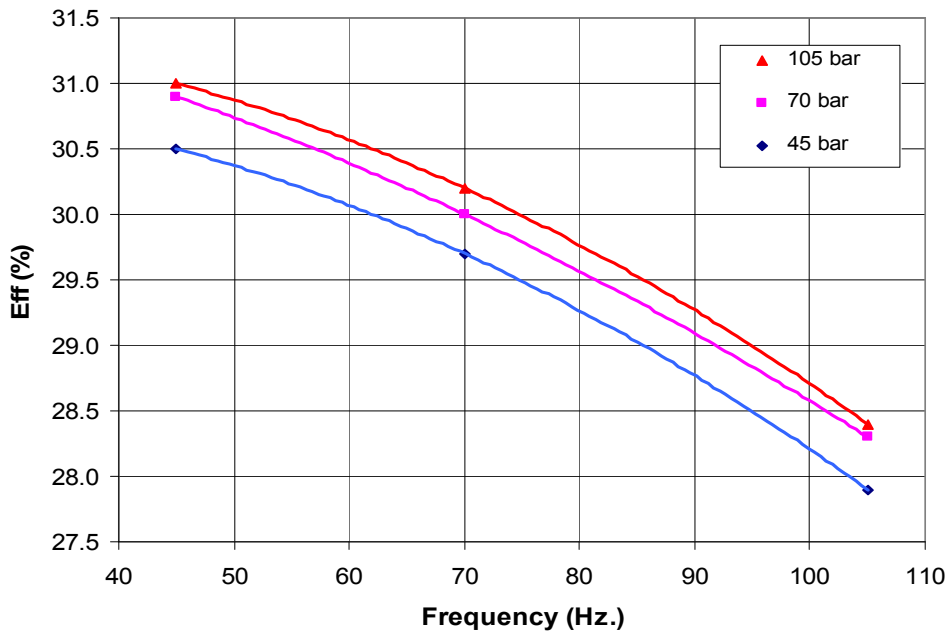


Figure 74.—Influence of frequencies on efficiency at different pressures.

### Projected Efficiency for a 12 kW Converter

A study was performed regarding the expected efficiency of a 12 kW (per side) converter. The primary results are shown in Figure 75. Note here that the efficiencies are approximately 20 percent lower than for the 6 kW design.

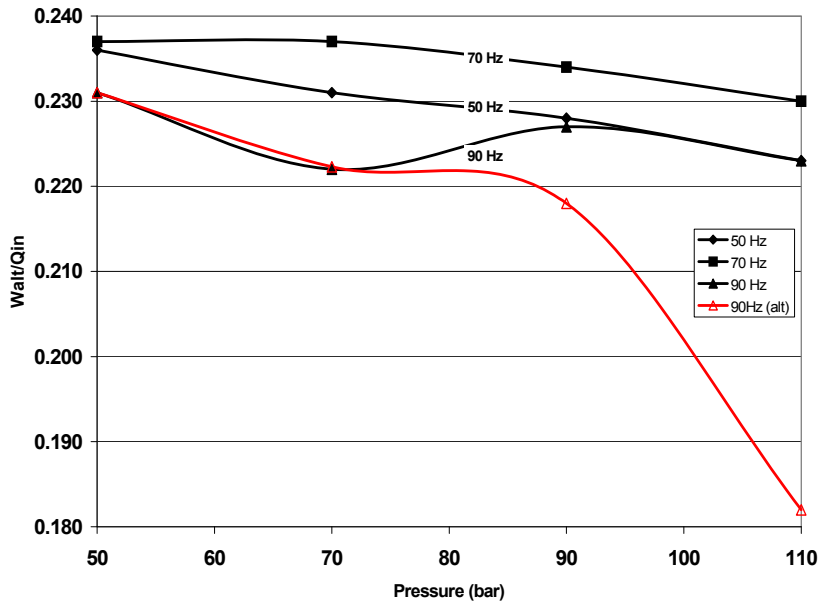


Figure 75.—Effectiveness versus pressure and frequency for a single 12 kW convertor.

The “90 Hz.alt” plot came from our initial studies. However as this plot diverged significantly from the others we decided to investigate the reason. The Sage optimization here had gone to different local optimum with a very large piston diameter (520 versus 210 mm at 110 bar), and a shorter piston amplitude of large mass. This was believed likely the result of the non-linear piston mass function used in the routine shown below. The solution would converge to a more normal and higher efficiency if began from a different starting point. The later and higher value 90 Hz. solution in the above plot has more reasonable values of piston diameter. We could have omitted the earlier plot for this report, but then we would need to explain why the 90 Hz curve was unsmooth. It appears that the reason is the “branch” in solutions at higher pressure.

$$M_{pis} = 1.38 + 2.15 * (0.7 / (\text{Freq} * X_{amp})) + 2.08 * \sqrt{ID_{cyl} / 0.127} \quad (1)$$

Fixed  
structure

Magnets

Shell

## CFD Modeling of Water Circuit

All CFD modeling was performed by Roberto Pellizzari of Environ International. It required six iterations of the water circuit design to arrive at a final configuration. We selected two different widths of passages, all of the same height, for the final design as shown in Figure 76. This starts with seven passages 1.9 mm wide near the inlet/outlet, followed by seven passages of 2.2 mm width, and finally a 1.9 mm passage again. The last passage was made smaller because otherwise the impingement at the end of the manifold resulted in an increased flow rate in this last passage.

The resulting flow rate in each passage is shown in Figure 77, where numbering starts closest to the inlet and outlet. The increase in the center of the plot is the result of changing to the wider passages.

One, of course, might ask why not try to get even more uniform flow. From our study we found no advantage in uniform flow, in fact it appears that non uniform water flow gives better Stirling cycle performance. We found that Sage predicted a higher efficiency with a positive temperature gradient along the rejector (increasing toward the regenerator). This reduced flow near the regenerator thus promoted such a gradient and resulted in higher Stirling efficiency.

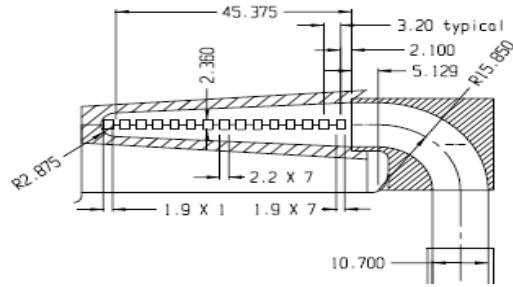


Figure 76.—Rejector water passage geometry.

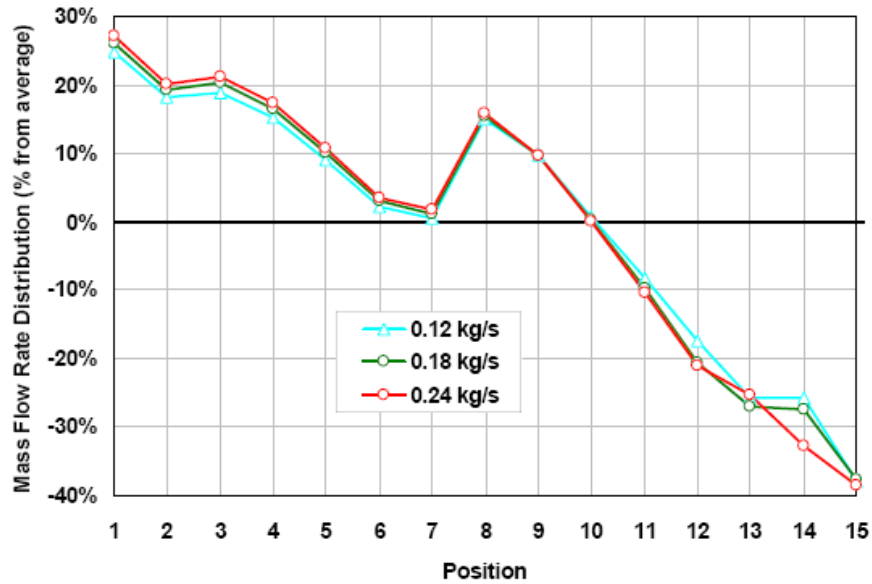


Figure 77.—Water flow distribution in the different passages.

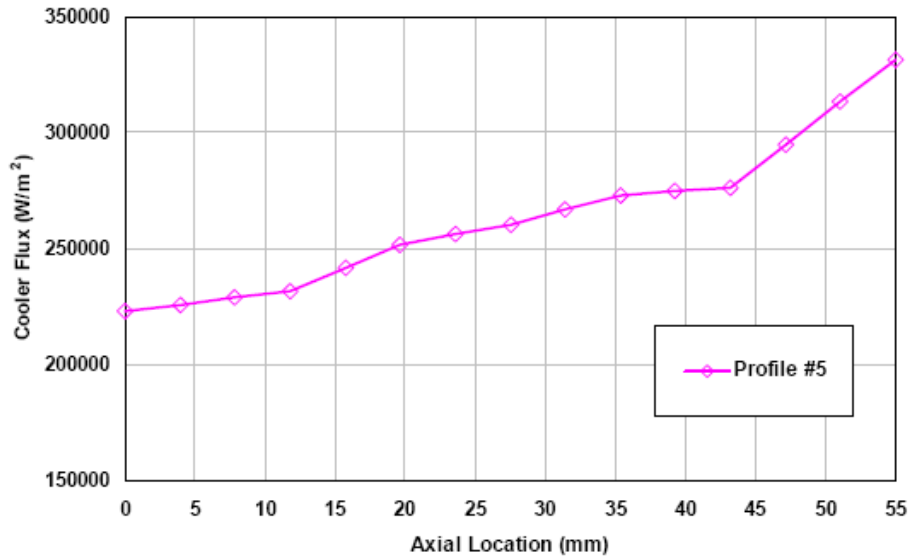


Figure 78.—Cooler heat flux along the length (starting at the compression space manifold).

Figure 78 shows the heat flux profile input into the CFD model. This profile was taken from a Sage simulation. For simplicity, we ended up using the same flux profile for all water flow rates.

Figure 79 illustrates the temperature variation on the copper surface (fin base) around the rejector. Note that Sage is a one-dimensional model and does not model circumferential temperature gradients. For Sage modeling we, therefore, used the CFD predicted temperature at  $\frac{3}{4}$  of the temperature between the coldest and hottest at any given axial location. We feel such an estimate is fairly realistic, if not conservative in the prediction of Stirling performance.

The above temperature profile, as well as those at the maximum and minimum flow rates is presented in Figure 80.

Flow rate (kg/s)	Pressure drop (kPa)	Coolant temperature rise (°C)
0.12	4.0	31.8
0.18	8.7	21.6
0.24	15.0	16.3

Pressure drop and temperature rise for three different flow rates

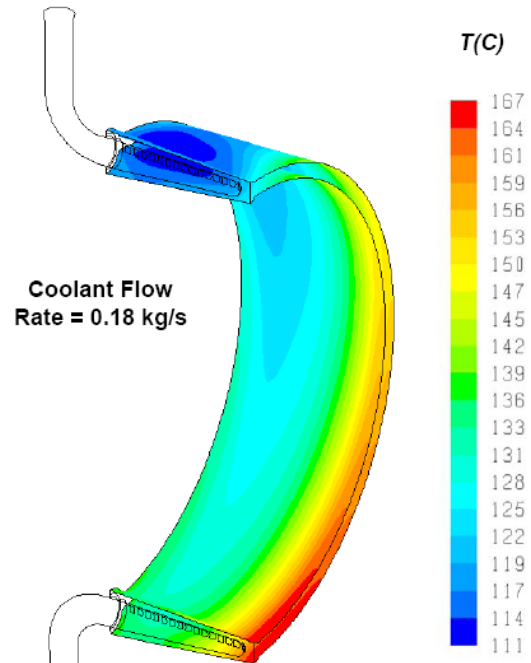


Figure 79.—Rejector temperature at He fin.

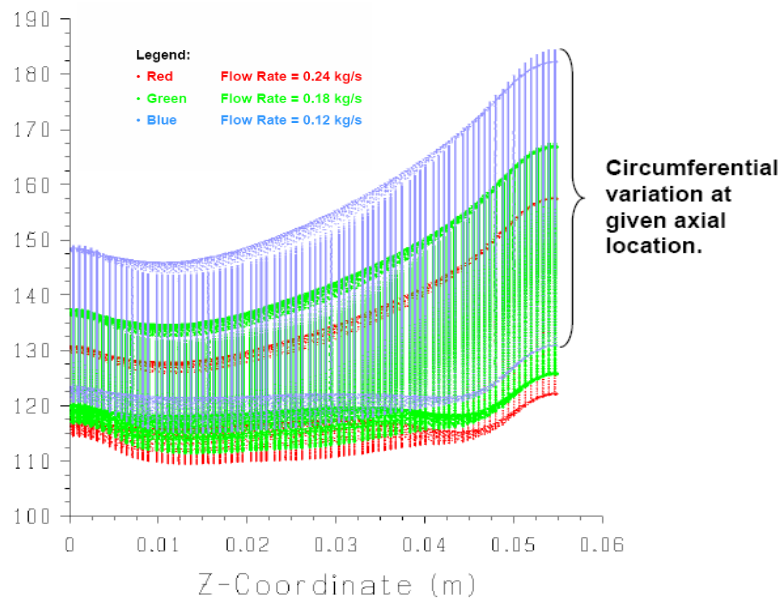


Figure 80.—Rejector wall temperature at different flow rates.

Figure 81 presents the static pressures (Pa) in the inlet and outlet manifolds.

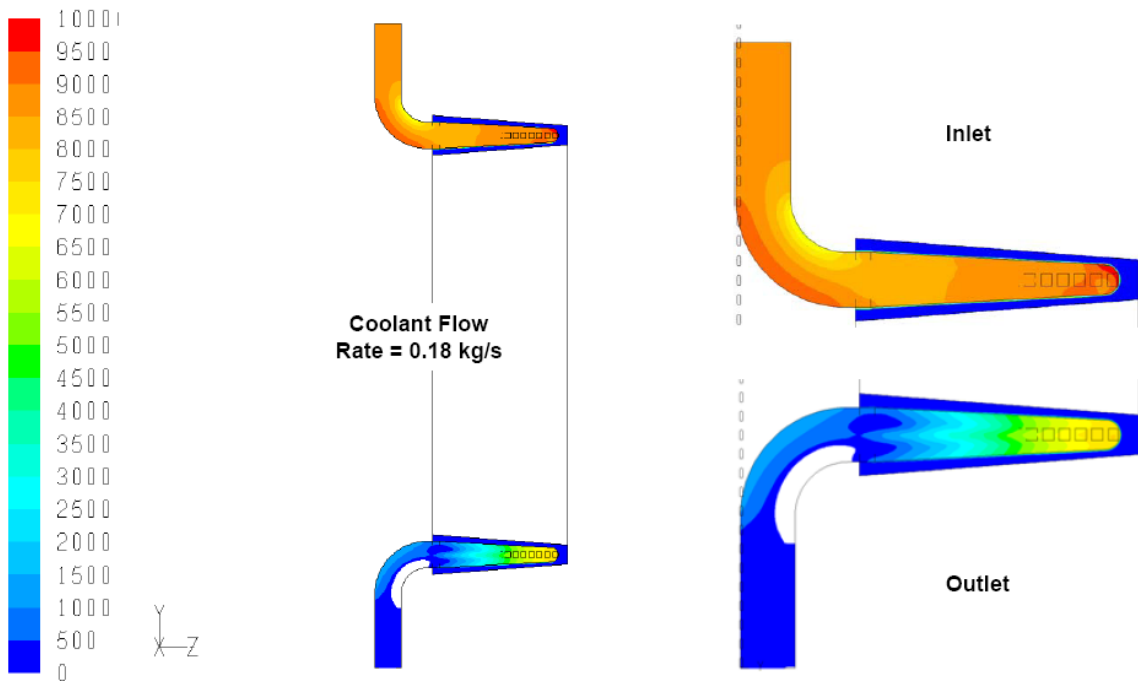


Figure 81.—Static pressures in water inlet and outlet manifolds.

## CFD Modeling of NaK Circuit

As with the rejector, CFD modeling of the LM circuit was performed by Roberto Pellizzari of Environ International.

### Original Radial Inlet Manifold

The layout of the NaK circuit was presented earlier in this report. The following presents the result of the CFD modeling effort that guided the design details of this circuit.

Early attempts were made with a radial inlet design, but with this it proved difficult to achieve uniform flow in all the passages. Basically passages under the inlet had high flow. We then tried a baffle but this essentially blocked flow in the top passages. Next we tried two different widths of slots in the baffle but this indicated that it was going to be difficult to get uniform flow without going to a complicated arrangement of baffles. Figure 82 shows the velocity distribution in the inlet manifold with three of the arrangements which we tried.

Figure 83 presents the temperature distribution on the inside of the heater head with three of the configurations studied.

Figure 84 shows the flow variation among slots with the four configurations tried.

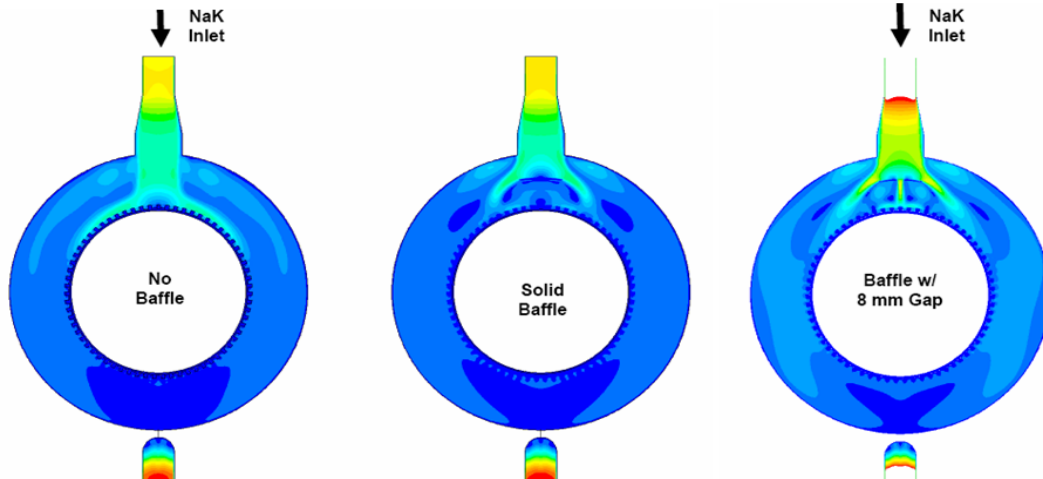


Figure 82.—Velocity fields in the inlet manifold with a radial inlet.

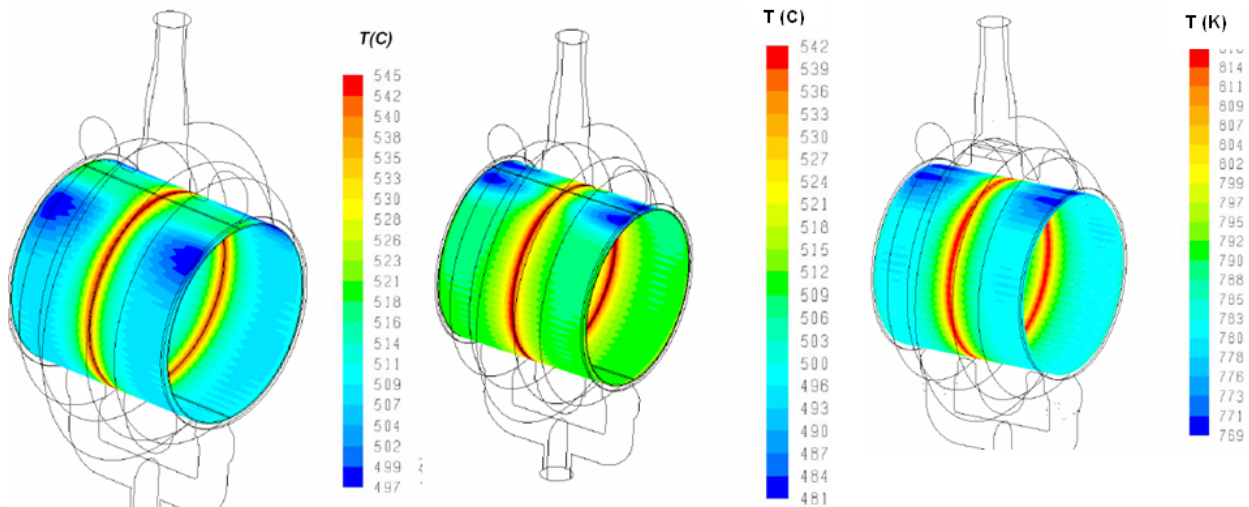


Figure 83.—Inside SS wall temperature with 1) no baffle, 2) baffle, and 3) baffle with an 8 mm slot.

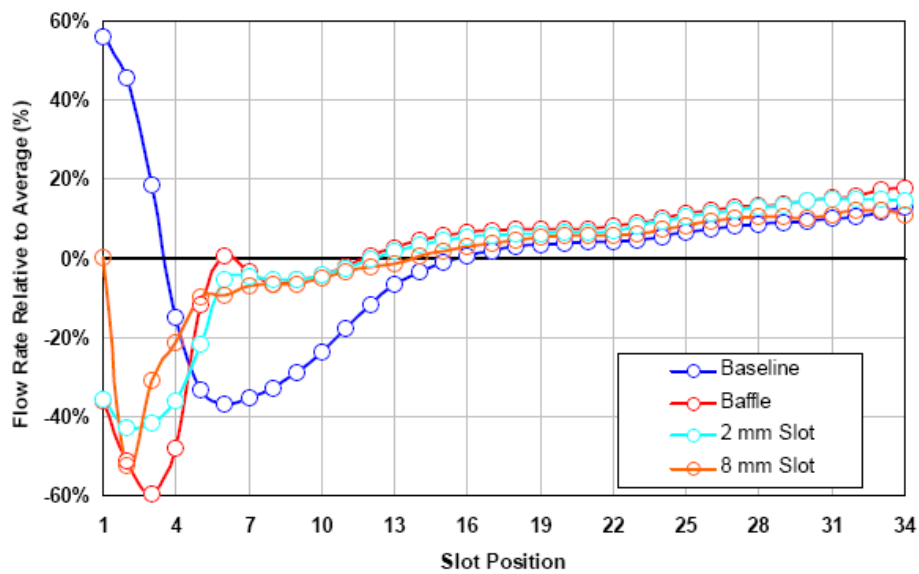


Figure 84.—Flow variations between passages with different baffle configurations.

## Final Tangential Inlet Manifold

Because of the difficulty in achieving uniform flow with the radial inlet, we decided to investigate a tangential inlet feeding into a scroll shaped manifold. This turned out to be an easier design task. After reviewing our first attempt, we made a modification to the recirculation area (minimum area of the scroll) and achieved very good flow uniformity in the HX passages in the next iteration. Figure 85 shows this uniformity; note that this scale is greatly magnified compared to the earlier similar plot for the radial inlet.

Figure 86 gives the heat flux profile at the inside of the outer solid copper of the internal acceptor, taken from Sage and used in the CFD modeling. Figures 87 and 88 show the CFD predicted temperature on the inside of stainless wall.

	Flow Rate (kg/s)		
	1.50	1.75	2.00
$\Delta T$ (C)	34.7	29.7	26.0
$\Delta p$ (Pa)	247	338	445
$Q$ (W)	22481	22481	22481

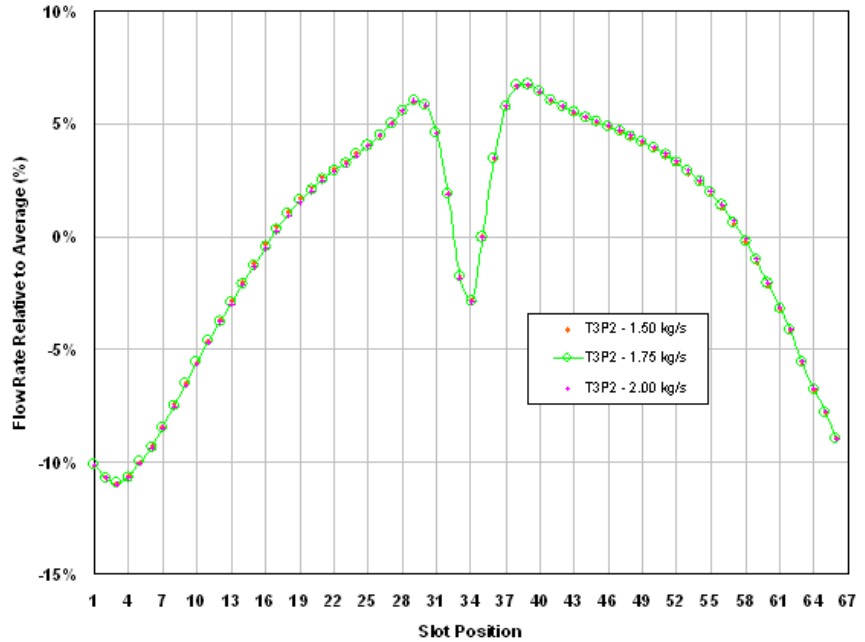


Figure 85.—Flow distribution in individual LM passages.

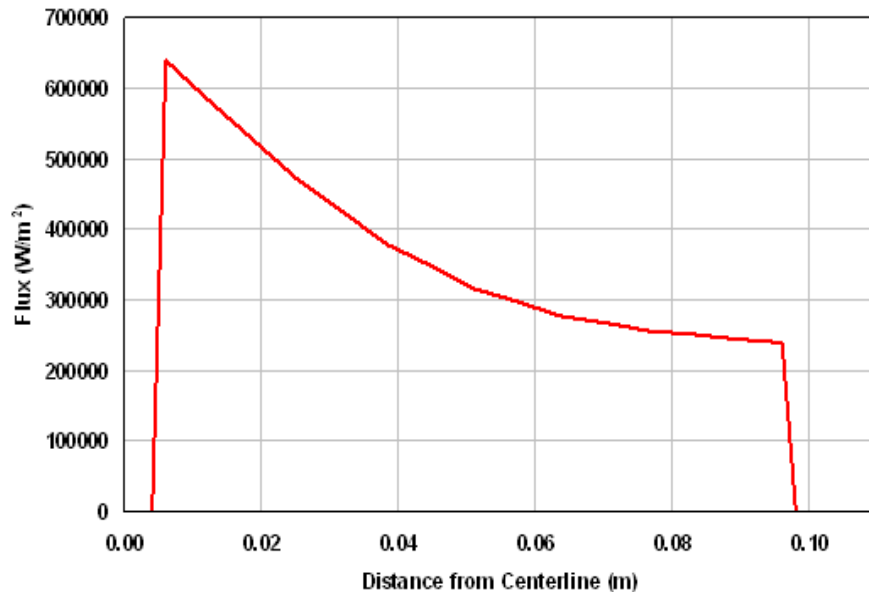


Figure 86.—Heat flux profile for the acceptor.

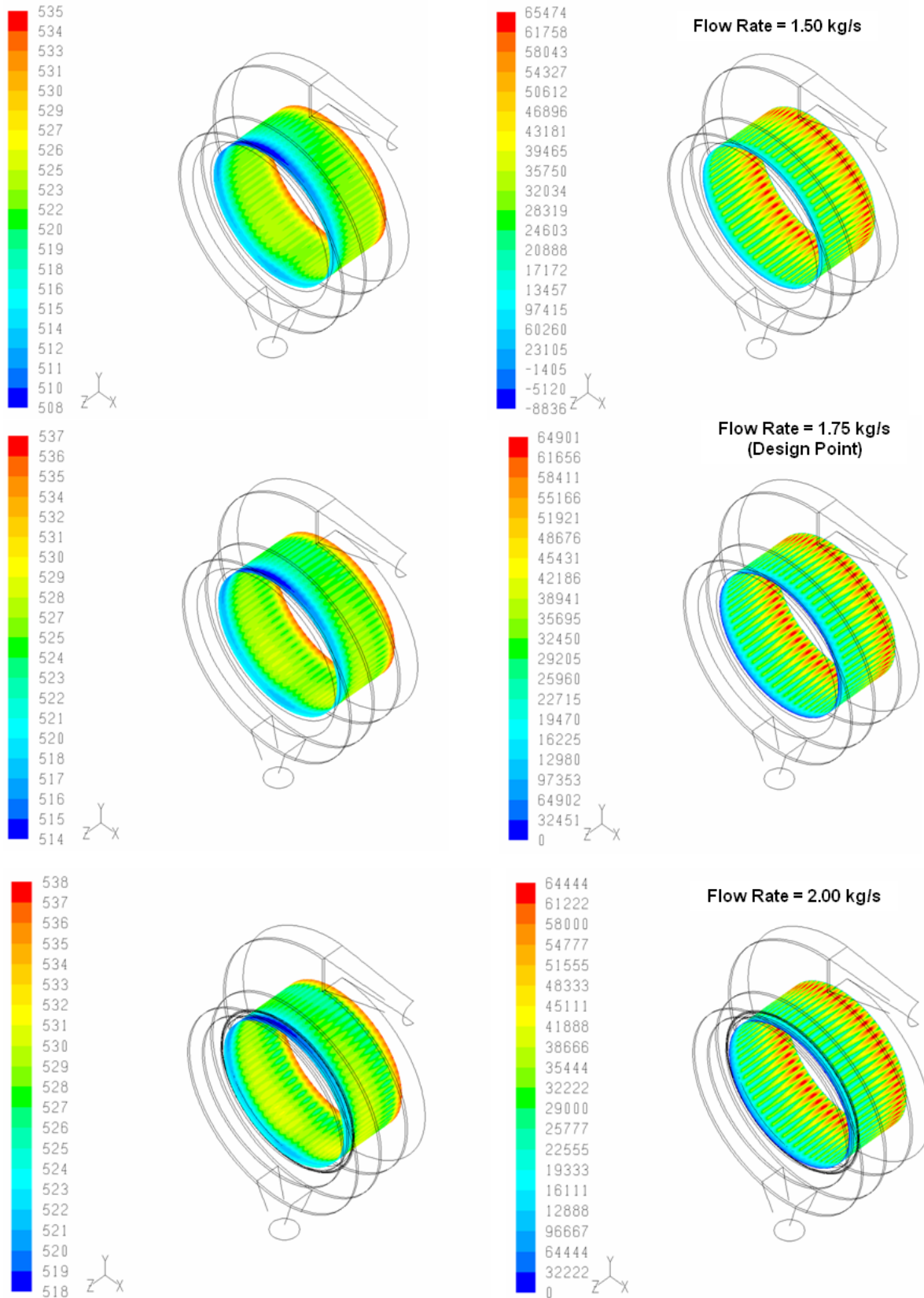


Figure 87.—Inside SS wall temperature (°C) and heat flux (W/m<sup>2</sup>) with selected tangential inlet at three flow rates.

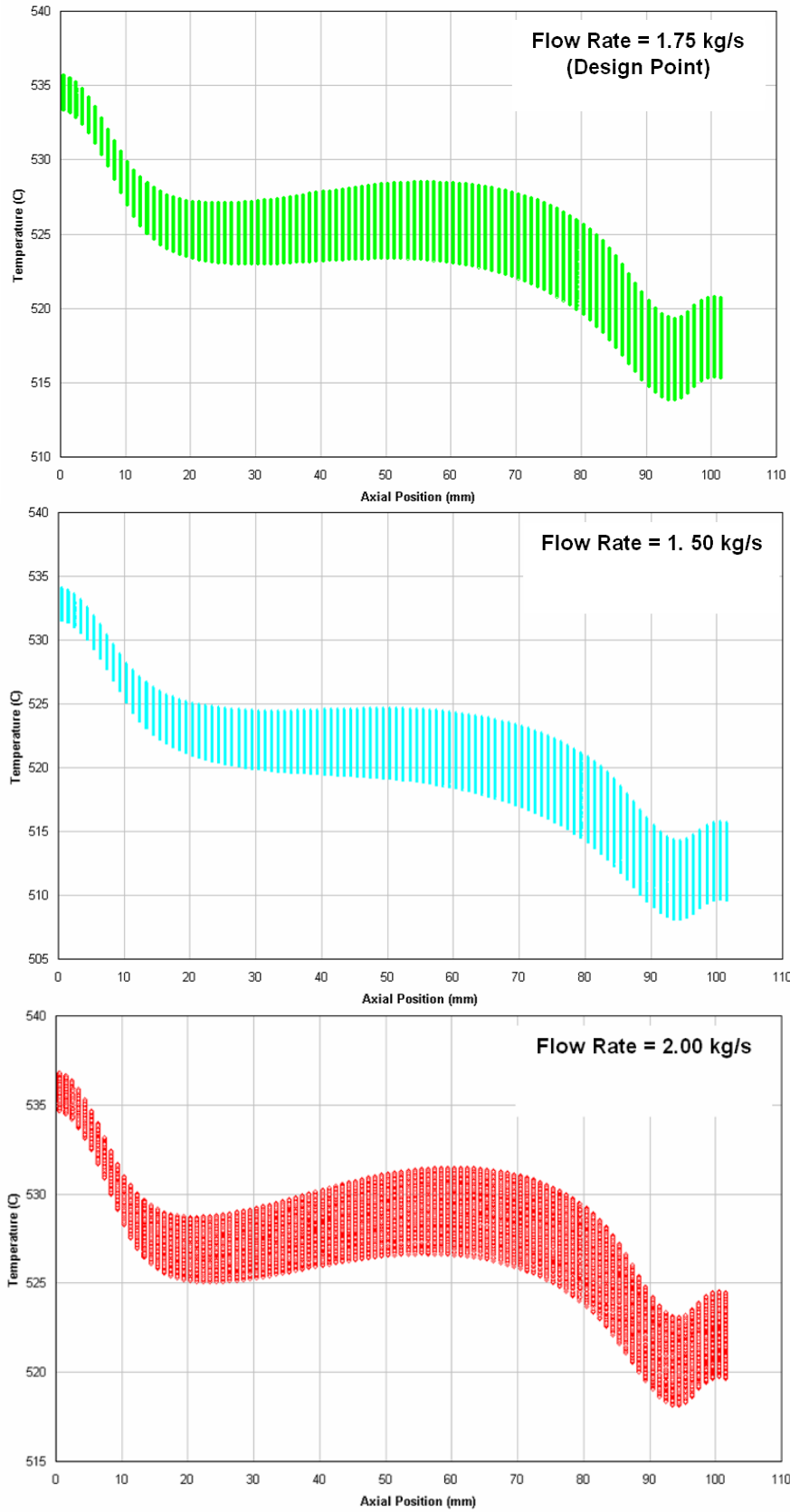


Figure 88.—Inside SS wall temperature with selected tangential inlet at three flow rates.

## Regenerator Flow Entry Effects

The external flow circuit CFD modeling turned out to be more involved than expected and we ran out of time and money before performing CFD modeling of the jet flow entries at the ends of the regenerator. Even if we had performed these the results would be somewhat in doubt because jet diffusion in the regenerator matrix would *not* be based on first principles, but rather some sort of ad hoc porous media model.

On the other hand we have actual experimental data available for round jets impinging on a random-fiber regenerator matrix with a porosity of 0.90 (close to FSP regenerator porosity of 0.91). These tests were run at the University of Minnesota and summarized in a 2003 engineering conference paper.

The Minnesota testing was based on round jets instead of the 2-D planar jets that would have been more appropriate for the FSP finned heat exchangers. We assumed that the same jet spreading angle applies to both cases. The only basis for this assumption is the observation that jet diffusion is based mainly on the localized physics at the scale of the matrix hydraulic diameter. So at the scale of the relatively large jets we are talking about the jet boundary curvature is relatively small in either case. (Jet boundary radius of curvature large compared to hydraulic diameter.)

Figure 89 depicts two jets emerging from adjacent fin channels into the regenerator matrix. The shaded regions represent the solid fin material between the channels. The jet diameters increase linearly with distance into the matrix (more or less consistent with observation) and merge into uniform flow after distance  $C$  into the matrix.

Evidently the distribution length  $C$  scales in proportion to fin thickness  $W$ . In the Minnesota experiments the fin thickness corresponds to  $S - D$ , where  $S$  is the hole spacing (between centers) and  $D$  is hole diameter.

The conclusion from the Minnesota experiments was that the jets were fully distributed after a distance  $C = 3.33 d_h$ , where  $d_h$  is the matrix hydraulic diameter. But hydraulic diameter is not the important thing. The jet spreading angle and separation distance seem more fundamental. So converting Minnesota's  $3.33 d_h$  into a fraction of the separation distance  $S - D$  for their experiment gives the simple formula for distribution depth:

$$C = 0.63(S - D)$$

In our case one can replace  $S - D$  with  $W$

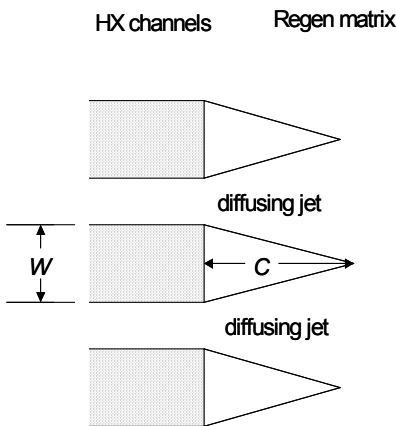


Figure 89.—Flow diffusion of gas entering the regenerator.

## Applied to FSP

According to Sage model aafinal\_base.stl, Table 20 values apply to the FSP engine:

TABLE 20.—FLOW DIFFUSION SUMMARY  
FOR FSP ENGINE

Rejector	
Mean fin thickness $W$	1.66 mm
Distribution Depth	1.04 mm
Acceptor	
Mean fin thickness $W$	3.21 mm
Distribution Depth	2.02 mm
Regenerator	
Total length	55 mm

So the combined distribution depth amounts to 5.6 percent of the total regenerator length.

## Applied to ASC

It is uncertain what it means that 5.6 percent of the regenerator length is required to achieve uniform flow. So it is useful to see how the FSP distribution depth compares to that for the ASC (Advanced Stirling Convertor) engine—an engine that is known to perform very well. Actually we chose here to use the earlier FTB which has a shorter regenerator, but still has very good thermodynamic performance.

It appears then that the effects of the regenerator distribution length for the FSP convertor will be three times as much as that of the FTB engine. The true influence of the regenerator distribution length calculation is unknown.

## Influence of Heater Head Wall Thickness

The ASME allowable stress for 316 SS is given in Figure 90. At lower temperatures, this is 5/8 of the yield stress. Above 566 °C (1050 °F), creep becomes the basis for the allowable stress and is established as 1 percent creep in 100,000 hr (11.4 yr).

Assuming an inlet LM temperature of 577 °C and a 10 °C drop from the LM to the wall, the hottest part of the acceptor wall would be at 567 °C which has an ASME allowable stress of 15.1 ksi. The required wall thickness at this temperature is 6.84 mm.

If the heat input were required to be transferred through the thickness, it would result in a severe penalty on efficiency as shown below. The current FSP design transfers heat through a 1 mm wall, with this wall externally supported by an outer support structure which supports the majority of the pressure load.

Figure 91 shows the temperature gradient along and through the stainless acceptor wall for the existing 1 mm wall thickness. The mean through-wall temperature drop is 15.9 °C, varying from 22 °C at the hottest end to 11 °C at regenerator end of the acceptor.

To illustrate the influence of thicker walls on efficiency, the Sage model was run with several values of wall thickness. For these runs we allowed re-optimization of the charge pressure, piston amplitude, the displacer dynamics, and the number and width of the internal acceptor helium passages (within the copper). Figure 92 and Table 21 present the results.

The severe performance penalty of thicker acceptor walls is noticeable. Also the pressure and displacement of the engine both increase. This occurs because the Stirling cycle is now operating across a lower temperature difference. Also, the through-wall temperature drop per mm of thickness increases (last column). This is the result of having to transfer more heat through the wall because of the falling cycle efficiency because of the effective lower cycle hot-end temperature.

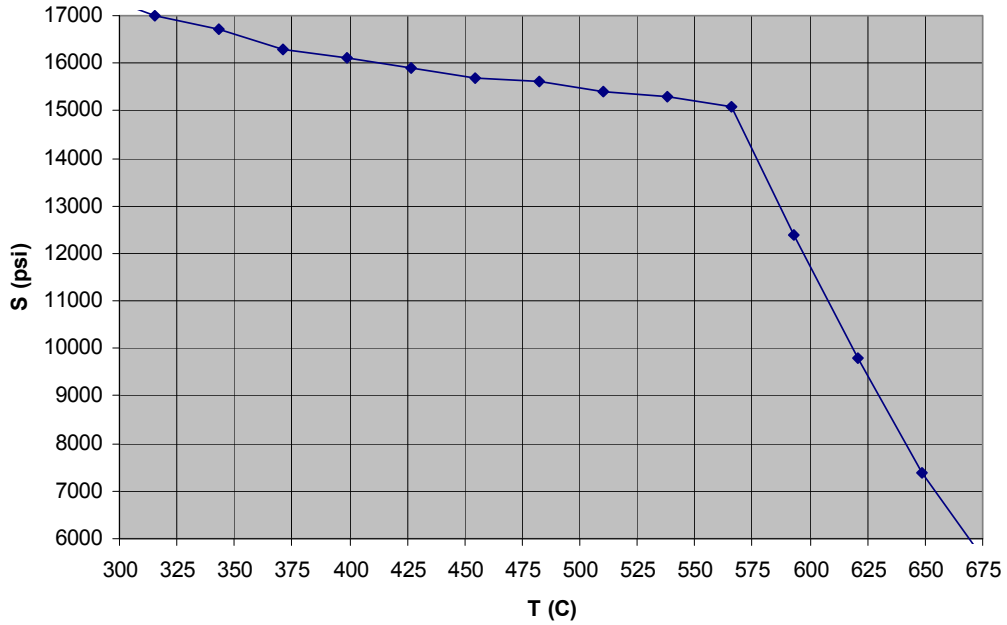


Figure 90.—ASME Pressure Vessel Code (Section VIII, Div. 1) allowable stress 316SS.

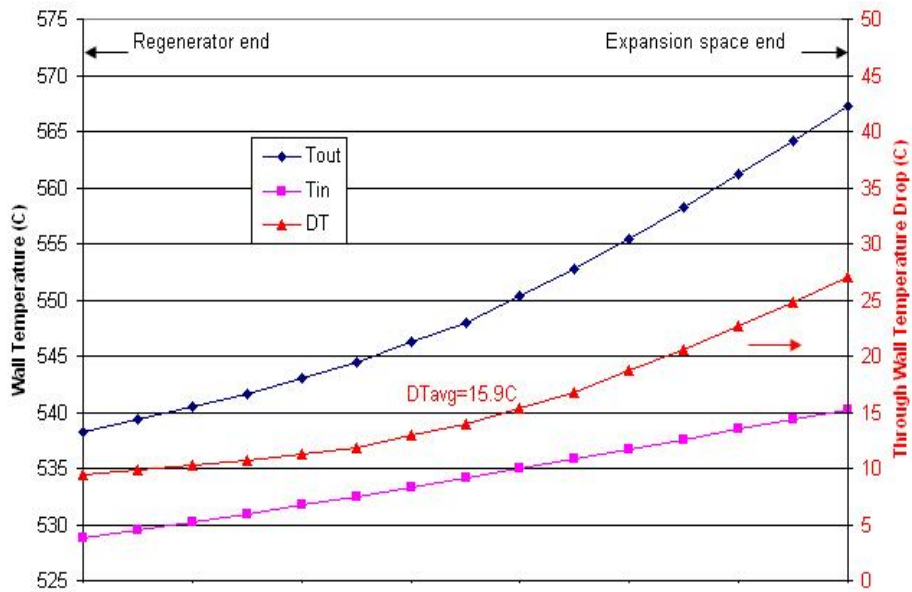


Figure 91.—Acceptor inner and outer wall temperature and through wall temperature drop.

One way to reduce the through wall temperature drop would be to increase the length of the acceptor. The major concern here is the added mass. The current estimated mass of convertor is 94 kg per side. Of this, the internal acceptor copper makes up 17 percent of the total mass (second only to the alternator).

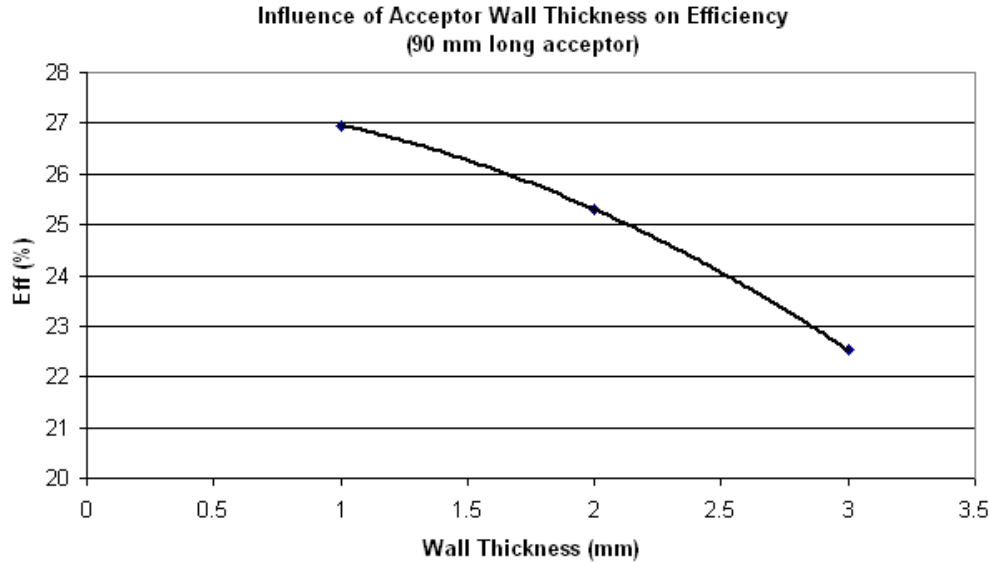


Figure 92.—Influence of acceptor wall thickness on efficiency (90 mm long acceptor).

TABLE 21.—OPTIMIZED OPERATING PARAMETERS FOR DIFFERENT HEATER HEAD WALL THICKNESSES

t <sub>wall</sub> (mm)	Eff (%)	P <sub>chg</sub> (bar)	P <sub>amp</sub> (bar)	X <sub>p</sub> (mm)	DT wall (°C)	DT/mm (°C/mm)
1	26.96	60.92	7.89	16	15.9	15.9
2	25.30	61.38	8.25	16.62	33.9	17.0
3	22.53	62.68	8.85	18.31	57	19.0

Although some gain can be made with a longer acceptor, it should be realized that the added length is not as effective as one might first believe. This is illustrated by the falling through-wall DT along the length of the acceptor. As shown earlier, the through-wall DT currently drops from 22 °C on the hot end to 11 °C at the cold end. Any added length actually adds to the least effective part of the acceptor. Basically, the major heat load on the acceptor is by the cooler gas entering from the expansion space.

On a final and rather minor note, the earlier stated 6.84 mm required wall thickness is slightly conservative. Actually the wall can be slightly thinner because the large through-wall DT results in the inner material having a slightly higher allowable stress. However this influence is pretty small because the design condition is below the creep range of the material where the allowable stress is not a strong function of temperature. Accounting for this, the wall thickness could be reduced to 6.6 mm.

### Concept to Reduce Internal Acceptor Mass

In reviewing the mass breakdown as shown in Table 6, it is seen that the internal acceptor is rather massive and accounts for 17 percent of the convertor mass. We did devise, but later abandoned for reasons of complexity, a means of reducing the acceptor mass.

Realizing that the non-linear heat flux along the acceptor places the highest load on the fins nearest the expansion space, the proposed concept was that by reducing the fin height here it would improve heat transfer while at the same time we could reduce the mass of copper. This concept is shown in Figure 93.

To evaluate this concept, David Gedeon modified the Sage file to model the acceptor with a series of steps along its length to approximate the tapered fins. Using this model, we found that performance was basically flat (actually increasing very slightly) from full height out to where the fins were half height at the leading edge (as shown in Fig. 93).

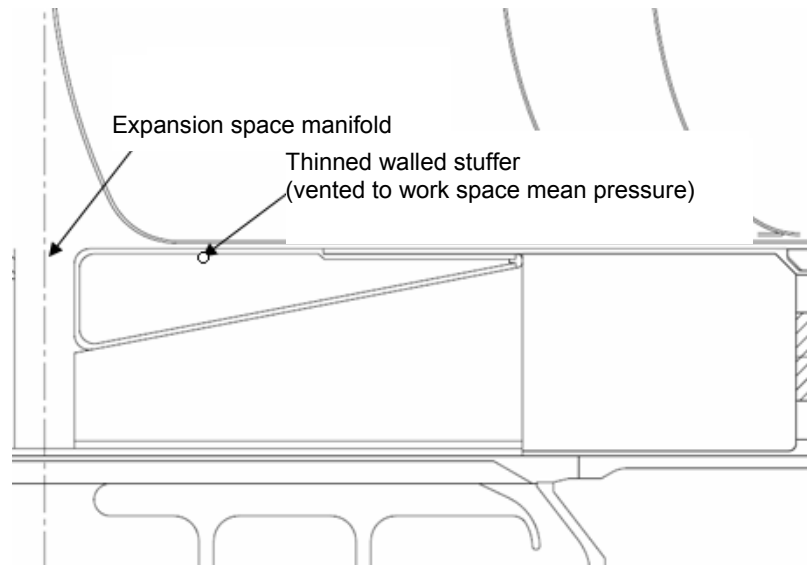


Figure 93.—Concept for reducing acceptor mass (not incorporated in the final design).

In the end, we decided not to incorporate this concept in the final design. It added complexity and appears it would have reduced overall convertor mass by only 2 to 3 percent. Additionally the tapered flow passages have not been tested before in actual convertors, so there was some risk to including it in this new hardware.

## Control Electronics

The control electronics for the pair of 6 kW Stirling convertors has been designed to have some key characteristics to meet the needs of the Fission Surface Power program. The characteristics are: 1) synchronization of the two 6 kW convertors, 2) constant command frequency operation, 3) ability to modulate the convertors amplitude thus allowing power modulation from zero to full power, 4) dissipation of any unused power that has been produced by the convertors, and 5) output voltage of 120 V dc.

The above features have been achieved through a modular design as shown by the block diagram in Figure 94. The major components of the control system are the Sunpower virtual tuning capacitor controller power stage, the 640 V to 120 V DC/DC power stage, the control DSP, the output shunt regulator, and the data acquisition system. Secondary components have also been added to the system to help support testing. These include an over stroke protection circuit and various power meters.

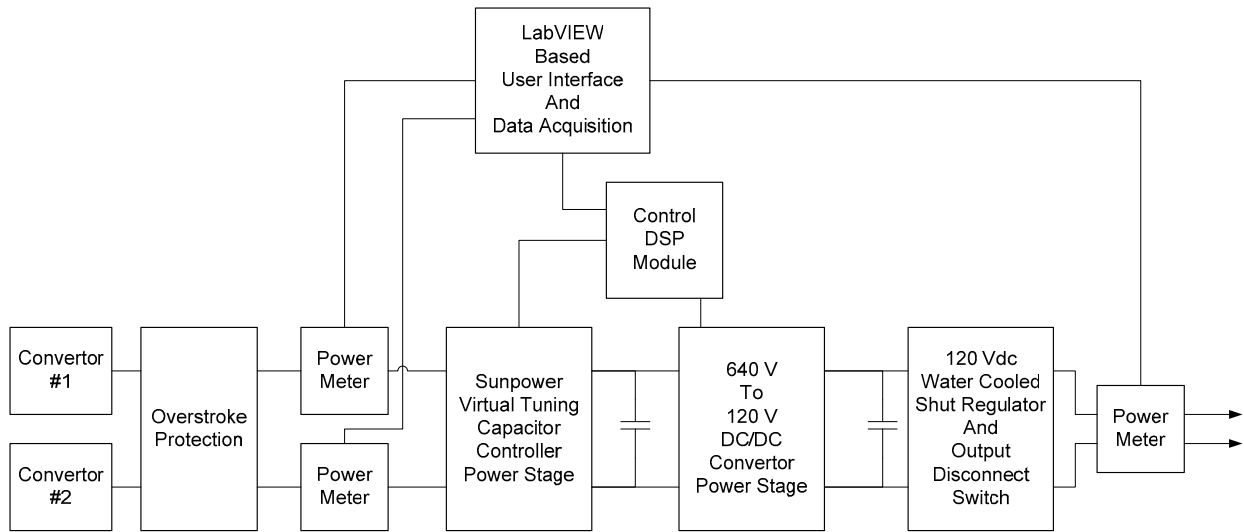


Figure 94.—Control system block diagram.

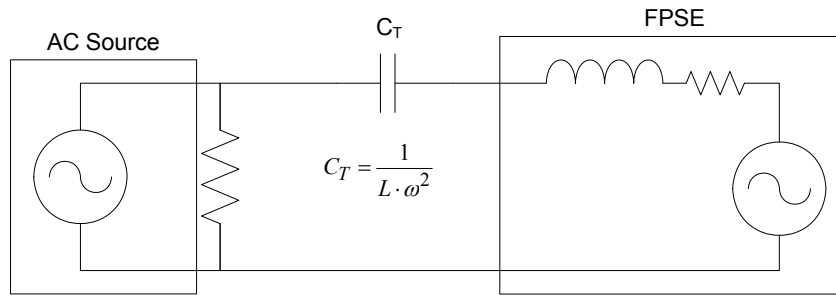


Figure 95.—AC source used to control a Stirling converter.

### Virtual Tuning Capacitor Controller Power Stage

The first major component of the control system is the virtual tuning capacitor power stage. This power stage is controlled by the control DSP to emulate a tuning capacitor and an ideal voltage source. The use of an ideal voltage source and a tuning capacitor as shown in Figure 72 is a well known and understood method of controlling a Stirling converter. This method of control is capable of controlling piston amplitude (0 to >100 percent) and frequency. Also, by synchronizing multiple voltage sources, multiple converters can be synchronized. The major problems with the typical implementation of this type of control are the need for a tuning capacitor inline with the converter current, the fact that an ideal voltage source is typically implemented by placing a AC power supply in parallel with a resistor causing the power supply to always supply power, and the variable voltage produced by the converter when the piston amplitude is modulated.

The previously mentioned problems are overcome by Sunpower's patented virtual tuning capacitor algorithm (US Patent no. 7,511,459). This algorithm switches a full bridge power stage at high frequency controlling the terminal voltage of the Stirling converter. The applied terminal voltage is a calculated sum of the desired virtual AC source, which can be modulated to control piston amplitude, and a calculated virtual tuning capacitor voltage based upon actual converter current. For clarification, neither the virtual AC source nor the virtual tuning capacitor exists in hardware. These only exist as calculation within the control loop.

As a result of the high frequency switching and the inductance of the converter alternator, the alternator is always in a boost state. This causes the output of the full bridge power stage to appear as a constant power source whose output power is a function of the piston amplitude and operating

temperatures of the convertor. This, in turn, causes the bus voltage to be the result of the energy balance of the power being produced and the power being consumed. With the proper design of the DC/DC converter and shunt regulator, as shown in Figure 95, the bus voltage will remain near constant regardless of the power being produced or the piston amplitude.

At the hardware level, the virtual tuning capacitor power stage is implemented as two identical water cooled, full bridge, IGBT power modules sharing a common DC bus, as show in Figure 96. Each power stage is dedicated to a single convertor and controlled as discussed above to synchronize the two 6 kW convertors.

The IGBT's are switched at 20 kHz resulting in 75 W of switching loss and 38 W of reverse recovery loss. Also, the conduction losses are approximately 89 W. These losses result in an approximate efficiency of each 6 kW module of 96 percent.

Each power module has an estimated mass of 230.9g and measure approximately 125- by 125-mm. Renderings of the power module can be seen in Figure 97.

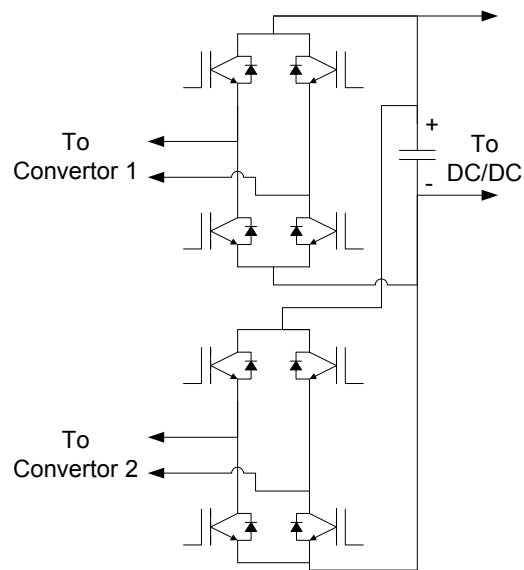


Figure 96.—Connection of two power modules.

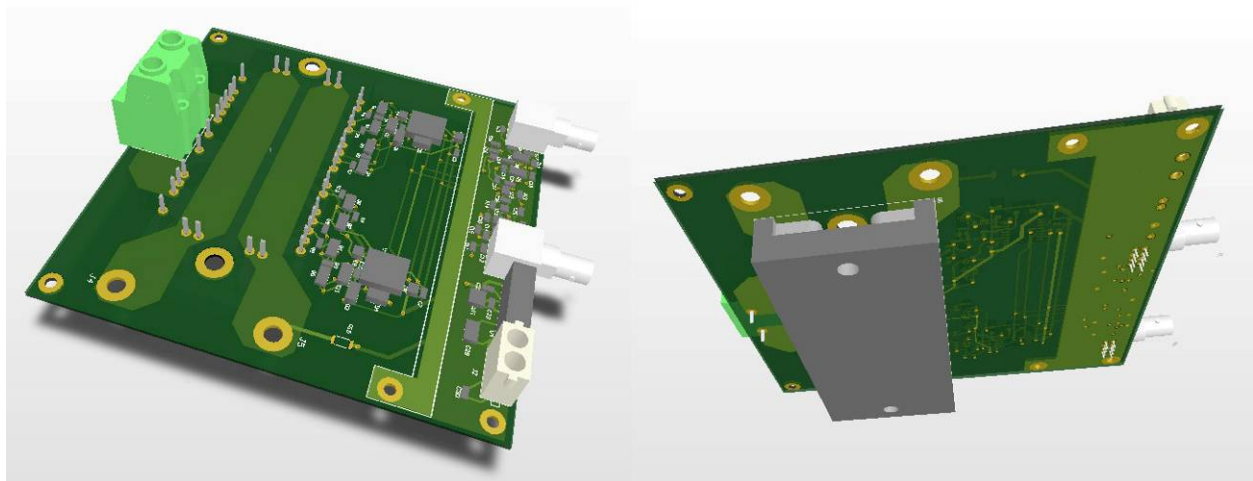


Figure 97.—Top and bottom view of 6 kW power module.

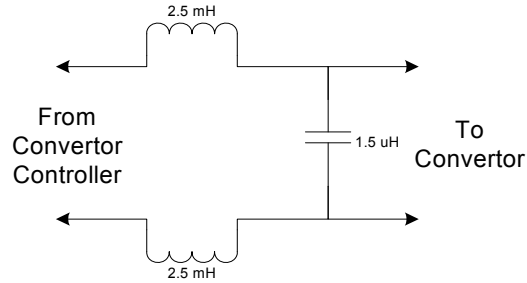


Figure 98.—Converter voltage LC filter.

### Converter Voltage LC Filter

Due to the expected long lead length between each full bridge power module and the converter, an LC filter has been added to filter the high frequency components from the voltage waveform. Without this filter, a few problems could occur. The first possible problem would be excessive EMI. The second would be extra core losses in the alternators due to the high frequency ripple current. Finally, it is possible that voltage multiplication could occur due to the inductance and capacitance of the converter power leads.

Each of the LC filters is implemented as show in Figure 98. As implemented, the cutoff frequency of this filter is 1.8 kHz. This should have the effect of removing most of the 20 kHz switching frequency from the voltages seen by the converter.

The mass of each filter is substantial at 18 kg. This mass however may be reduced if it is found that it is acceptable to attenuate less of the switching harmonics. It may also be possible to reduce the mass by investigate multi-order LC filters.

### DC/DC Converter

The DC/DC converter is present to convert the approximately 640 V bus from the engine control power modules down to the desired 120 V output. An LLC topology, as shown in Figure 99, was chosen due to the ability to switch at high frequencies while maintaining extremely low switching losses.

The LLC topology consists of a full bridge power stage running at approximately 50 percent duty cycle. This generates a square wave voltage that is filtered by a filter network consisting of a series capacitor, series inductor, and a parallel inductor. The voltage across the parallel inductor is then scaled by a transformer and finally rectified to achieve a DC output.

The low switching losses mentioned above are achieved because the converter is run at a frequency such that the current always lags the voltage. This causes the turn-on losses to be zero. Turn-off losses are still present. But, they are very small due to the output capacitance of the MOSFET's making up the full bridge power stage.

The gain of the voltage filter network versus frequency is shown in Figure 100. As can be seen, the gain of the network is 1 at the series resonant frequency of 100 kHz. By placing a 120 V shunt regulator on the output of the LLC converter as shown in Figure 94 and operating the DC/DC converter at the series resonant frequency, the power transferred from the 640 V bus to 120 V bus will be such that the 640 V bus will stay at a constant voltage as long as the power pulled from the 120 V bus is not so great as to pull the voltage bellow 120 V.

The full bridge power stage, as rendered in Figure 101, is implemented as a 125- by 125-mm module using discrete MOSFET's that are controlled through fiber optic links by the central control DSP. At 12 kW of input power and 100 kHz switch the power stage has extremely low losses. The losses of the full bridge power stage are estimated as 240 W conduction, 3 W of turn-off, and 2 W of loss in the body diodes.

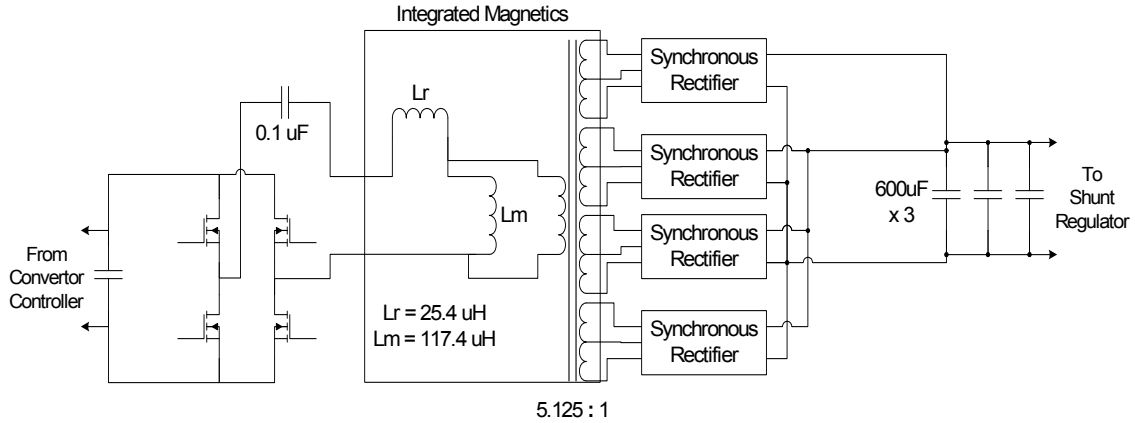


Figure 99.—LLC DC/DC converter.

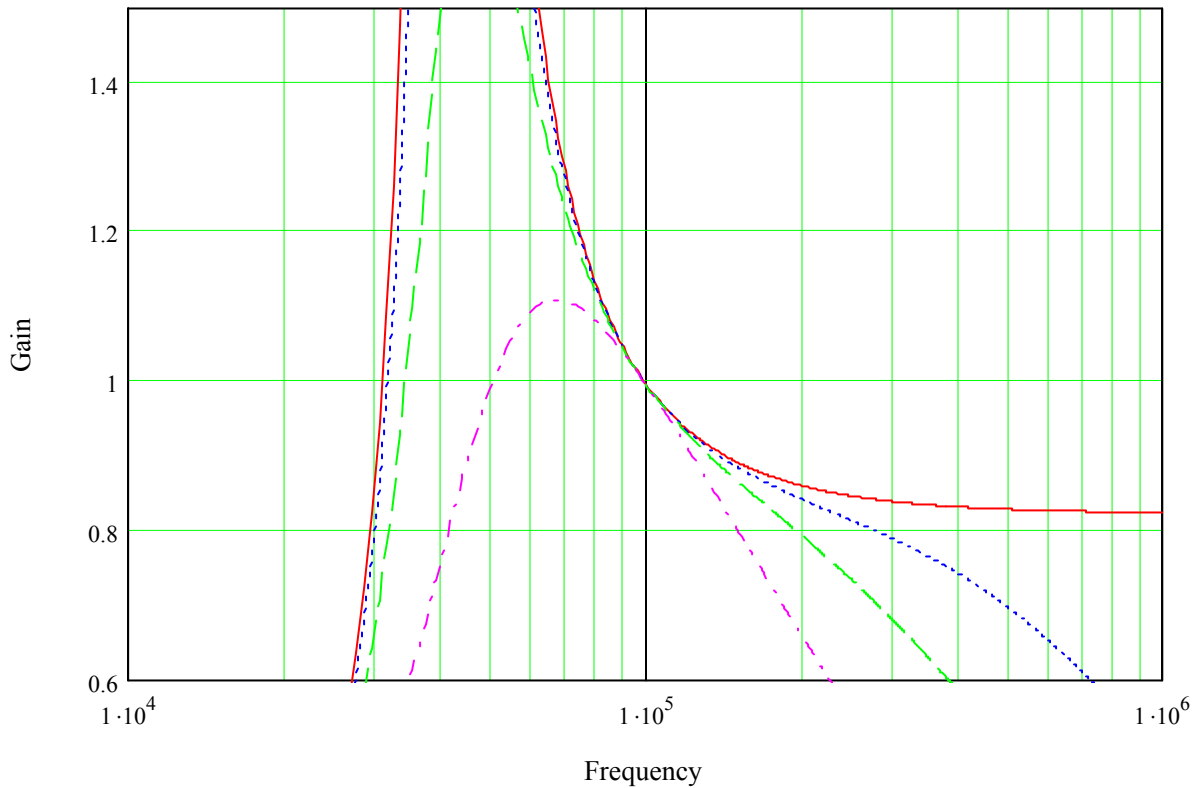


Figure 100.—Voltage filter network gain.

The transformer, series inductor, and parallel inductor have been designed as a single integrated magnet structure. The basic structure can be seen in Figure 102. This allows for low mass (2.5 kg), low loss (35 W core, 40 W gap, and 28 W copper), and small size (128- by 120- by 40-mm).

To further achieve high efficiency, the output of the transformer is rectified using a synchronous rectification. This form of rectification limits the rectification losses to approximately 54 W.

To allow for startup of the Stirling convertor, diodes are placed around the transformer to the 120 V user bus. This allows power to flow from the user bus to the high voltage bus but not the other direction. This does have the consequence of limiting the voltage available on the 640 V bus to 120 V. If a higher

voltage is necessary during startup, the synchronous rectifier stage can be modified to be controlled by the control DSP to allow boosting of the 120 V user bus voltage.

The sum of the power stage losses, magnetic losses, and rectification losses within the DC/DC converter come in at an estimated 402 W. This gives an estimated high efficiency of 96 percent.

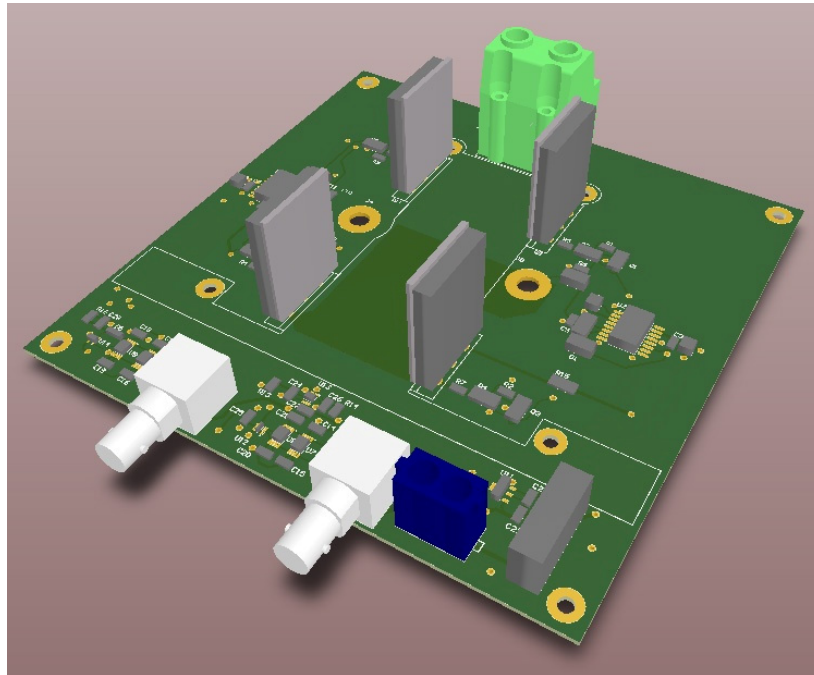


Figure 101.—DC/DC full bridge power module.

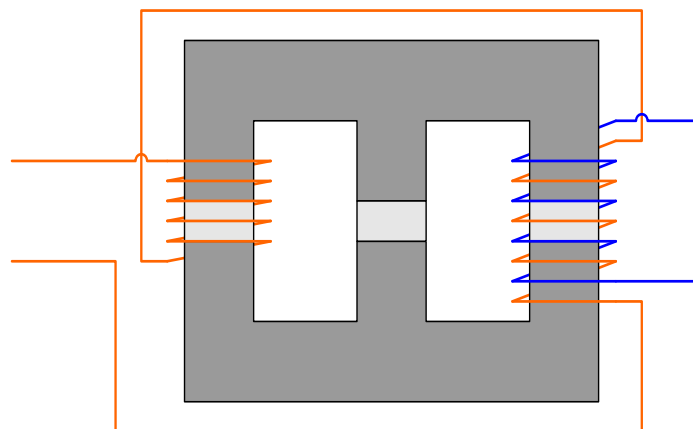


Figure 102.—Integrated magnets.

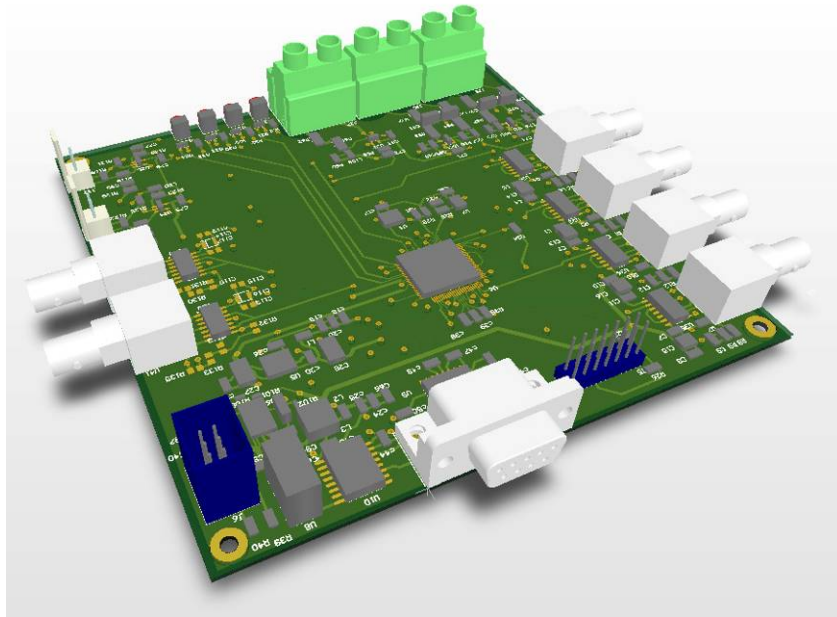


Figure 103.—Control DSP module.

### **Control DSP Module**

The control DSP module, as rendered in Figure 103, is a 125- by 125-mm, 85.4g module based around a Texas Instruments TMS320F2808 DSP (digital signal processor). The control loops for the virtual tuning capacitor control and the LLC DC/DC converter are implemented within the DSP module.

The DSP has various connections for feedback and control. The feedback signals present on the module are alternator current, alternator voltage, and high voltage bus feedback. Also present on the DSP module is an isolated RS-232 interface for connection to the data acquisition system allowing the commanded amplitude and frequency of the Stirling convertor to be changed during testing. And finally, fiber optic connections are on the board to provide gate drive signals to the DC/DC converter and the virtual tuning capacitor power stages.

### **Shunt Regulator and Output Disconnect Switch**

The shunt regulator/output disconnect module, measuring 283- by 118-mm for the control board and 202- by 261- by 470-mm for the resistor bank, performs two separate tasks. First this module is a 12 kW shunt regulator that regulates the output voltage of the control system to 120 V. The second task is to connect and disconnect the system from the main 120 V user bus. The connection to the user bus is controlled by the output voltage of the DC/DC converter. If the output voltage drops below 110 V, the Stirling convertor system is disconnected from the 120 V user bus. Once the DC/DC output voltage returns to 120 V it is reconnected to the 120 V user bus. The output disconnect switch can also be controlled by the control DSP.

### **Summary**

The proposed control system meets the desired functional characteristics of convertor synchronization, commanded frequency operation, ability to modulate convertor amplitude (0 to max available), dissipation of any unused power, and a final output voltage of 120 V. These characteristics are also achieved at an efficiency of 91 percent as can be seen from the review of overall efficiency in Table 22.

TABLE 22.—CONTROLLER CALCULATED EFFICIENCY

Qty	Description	Unit Loss (W)	Extended Loss (W)
2	LC Filter	58	116
2	Convertor Power Stage	202	404
1	DSP Board	4	4
1	DC/DC Full Bridge	245	245
1	DC/DC Magnetics	103	103
1	Synchronous Rectifier	54	54
1	Shunt Controller	2	2
1	Output Switch	20	20
1	Interconnect	60	60
1	Bus Capacitors	30	30
		<b>Total Loss (W)</b>	1038
		<b>Efficiency</b>	91.35%

## References

1. Burdi, G.F., "SNAP Technology Handbook, Vol. 1, Liquid Metals", NASA SR-8617
2. Hoffman, H.W., Yoder, G.L., "Liquid Metal Heat Transfer Issues," DOE CONF-840113-4.
3. ASME Pressure Vessel Code, Section 8, Divisions 1 and 2.
4. ASME Pressure Vessel Code, Section III, Division 1 – NH.
5. Dochat, G., "SPDE/SPRE Final Summary Report," NASA CR-187086
6. Penswick, L.B., "A 1050 K Stirling Space Engine Study," NASA CR-182149
7. Dudenhoefer, J., "Programmatic Status of NASA's CSTI High Capacity Power Space Power Convertor Program," NASA TM-103142.
8. Deissler, R.G., "Analysis of Fully Developed Turbulent Flow Heat Transfer at Low Peclet Number in Smooth Tubes with Application to Liquid Metals," NACA RM E52F05
9. Shah, R.K., Kakac, K., Aung, W., "Handbook of Single Phase Convective Heat Transfer," 1987.
10. Ozisik, M.N., "Heat Transfer—A Basic Approach," 1987.
11. von Glahn, U.H. "Empirical Equations for Turbulent Forced convection heat Transfer for Prandtl Numbers from .001 to 1000," NASA TMD-483
12. Inman, R.M., "Heat Transfer for Liquid Metal Flow in Rectangular Channels With Prescribed Wall heat Fluxes and Heat Sources in the Fluid Flow," NASA TM-X-52170
13. Black, W.Z., Wulff, W. "Space Radiator Simulation System Analysis," NAS9-10415
14. Geng, S.M., et.al., "Overview of Multi-KW Free Piston Stirling Power Conversion Research at Glenn Research Center," NASA TM 2008-215061
15. Bomelburg, H.J., "Evaluation of the Applicability of Water Model Testing of Liquid Metal Engineering Problems," LMEC-68-4
16. Mason, L., et al., "Fission Surface Power technology Development Status," NASA/TM—2009-215602

REPORT DOCUMENTATION PAGE			Form Approved OMB No. 0704-0188		
<p>The public reporting burden for this collection of information is estimated to average 1 hour per response, including the time for reviewing instructions, searching existing data sources, gathering and maintaining the data needed, and completing and reviewing the collection of information. Send comments regarding this burden estimate or any other aspect of this collection of information, including suggestions for reducing this burden, to Department of Defense, Washington Headquarters Services, Directorate for Information Operations and Reports (0704-0188), 1215 Jefferson Davis Highway, Suite 1204, Arlington, VA 22202-4302. Respondents should be aware that notwithstanding any other provision of law, no person shall be subject to any penalty for failing to comply with a collection of information if it does not display a currently valid OMB control number.</p> <p>PLEASE DO NOT RETURN YOUR FORM TO THE ABOVE ADDRESS.</p>					
<b>1. REPORT DATE (DD-MM-YYYY)</b> 01-07-2010		<b>2. REPORT TYPE</b> Final Contractor Report		<b>3. DATES COVERED (From - To)</b>	
<b>4. TITLE AND SUBTITLE</b> Free-Piston Stirling Power Conversion Unit for Fission Surface Power, Phase I Final Report			<b>5a. CONTRACT NUMBER</b> NNC08CA65C		
			<b>5b. GRANT NUMBER</b>		
			<b>5c. PROGRAM ELEMENT NUMBER</b>		
<b>6. AUTHOR(S)</b> Wood, J., Gary; Buffalino, Andrew; Holliday, Ezekiel; Penswick, Barry; Gedeon, David			<b>5d. PROJECT NUMBER</b>		
			<b>5e. TASK NUMBER</b>		
			<b>5f. WORK UNIT NUMBER</b> WBS 463169.04.03.01.02		
<b>7. PERFORMING ORGANIZATION NAME(S) AND ADDRESS(ES)</b> Sunpower, Inc. 182 Mill Street Athens, Ohio 45701			<b>8. PERFORMING ORGANIZATION REPORT NUMBER</b> E-17327		
<b>9. SPONSORING/MONITORING AGENCY NAME(S) AND ADDRESS(ES)</b> National Aeronautics and Space Administration Washington, DC 20546-0001			<b>10. SPONSORING/MONITOR'S ACRONYM(S)</b> NASA		
			<b>11. SPONSORING/MONITORING REPORT NUMBER</b> NASA/CR-2010-216750		
<b>12. DISTRIBUTION/AVAILABILITY STATEMENT</b> Unclassified-Unlimited Subject Category: 20 Available electronically at <a href="http://gltrs.grc.nasa.gov">http://gltrs.grc.nasa.gov</a> This publication is available from the NASA Center for AeroSpace Information, 443-757-5802					
<b>13. SUPPLEMENTARY NOTES</b>					
<b>14. ABSTRACT</b> This report summarizes the design of a 12 kW dual opposed free-piston Stirling convertor and controller for potential future use in space missions. The convertor is heated via a pumped NaK loop and cooling is provided by a pumped water circuit. Convertor efficiency is projected at 27 percent (AC electrical out/heat in). The controller converts the AC electrical output to 120 Vdc and is projected at 91 percent efficiency. A mechanically simple arrangement, based on proven technology, was selected in which the piston is resonated almost entirely by the working space pressure swing, while the displacer is resonated by planar mechanical springs in the bounce space.					
<b>15. SUBJECT TERMS</b> Free-piston Stirling power conversion unit; Fission surface power; NaK heating circuit					
<b>16. SECURITY CLASSIFICATION OF:</b>			<b>17. LIMITATION OF ABSTRACT</b>  UU	<b>18. NUMBER OF PAGES</b> 95	<b>19a. NAME OF RESPONSIBLE PERSON</b> STI Help Desk (email:help@sti.nasa.gov)
<b>a. REPORT</b> U	<b>b. ABSTRACT</b> U	<b>c. THIS PAGE</b> U			<b>19b. TELEPHONE NUMBER (include area code)</b> 443-757-5802



